MicroCT imaging of bone architecture and vasculature

Maarten DEPYPERE

Jury:
Prof. dr. ir. H. Hens, chair
Prof. dr. ir. F. Maes, promotor
Prof. dr. G. Carmeliet, co-promotor
Prof. dr. ir. J. Nuyts, co-promotor
Prof. dr. ir. P. Suetens
Prof. dr. ir. D. Vandermeulen
Prof. dr. ir. H. van Lenthe
Prof. dr. J. Sijbers
(Universiteit Antwerpen)
Dr. P. Salmon
(Bruker microCT)

Dissertation presented in partial fulfilment of the requirements for the degree of Doctor in Engineering

June 2013

D/2013/7515/63
ISBN 978-94-6018-677-6

"Ach, was ich weiß, kann jeder wissen —
mein Herz hab' ich allein."

Johann Wolfgang von Goethe,
Die Leiden des jungen Werthers

Acknowledgements

As for any valuable life experience, this text is the result of many interactions with interesting people. I would like to take this opportunity to acknowledge the most prominent contributors to this thesis.

This work would not exist without the scientific ideas, inspirational passion, broad support and motivational speeches of my promotors prof. Frederik Maes, prof. Geert Carmeliet and prof. Johan Nuyts. I would like to thank them for giving me the opportunity to perform this research, instructing me in their respective domains of expertise, encouraging me to pursue my own suggestions and mentoring me in science and life in general. Frederik, thank you for providing the freedom when desired but guidance when needed. Geert, thank you for your patience and understanding when your research questions had to wait for other investigations. Johan, thank you for letting me tap into your reconstruction expertise and code, and for programming the elaborate user interfaces yourself for me.

I would like to thank my assessors prof. Paul Suetens, prof. Dirk Vandermeulen, and prof. Harry van Lenthe for their interest in this work and their critical comments throughout the years. Additionally, I want to thank Paul for creating and maintaining a stimulating and productive working environment, and for listening to and helping to resolve any grievances. I would like to thank all the members of the jury for their time and effort in evaluating this thesis and for their constructive comments and suggestions.

The technical support provided by Dominique Delaere and Bart De Dobbelaer has been indispensable to this work. I would like to thank Dominique and Bart for the infrastructural setup that enabled working efficiently, and for their genuine dedication in helping me out with programming challenges, compilation errors, all MeVisLab applications, extending the lifetime of the old cluster and anything computer related in general. I am grateful to Annitta De Messemaeker and Patricia Waege for all the administrative assistance.

The good atmosphere in the Medical Image Computing group throughout the years has been created by too many colleagues to name, but I would like to address some people I am particularly grateful to. Janaki Raman Rangarajan has been a constant source of generosity and support, and an excellent sparring partner in discussions about application-driven research. Jeroen Hermans readily shared his profound mathematical and emotional insights, always flavoured with a few profane jokes, to resolve any problems. Dirk Smeets inspired me with his enthusiasm, his energy, and his countless scientific and recreational initiatives to involve everyone. Stijn De Buck and Annemie Ribbens were always available for advice or a casual chat and proved to be great travel companions. Dirk Loeckx stimulated an environment where knowledge and experience could be gained and shared easily, and I have benefitted immensely from his knowledge and experience. Pieter Bruyninckx and Sarah Shrimpton provided cultural tips and valuable insights as well as amusing reflections on the more universal questions of life.

I had the luxury of being part of the Legendo laboratory, where I was always welcomed with enthusiastic smiles and helping hands. Over the years, their kind and relentless explanations transformed the incomprehensible labmeetings into understanding and appreciation of the biomedical pathways they try to decrypt. The unrivalled organisational enthusiasm of Ingrid Stockmans led to countless activities, lunches, parties and weekends in which Ingrid, Kjell Laperre, Steve Stegen, Nick van Gastel, Liesbet Lieben, Sophie Baret, An Vanden Bosch, Christa Maes, Werner Verbakel, Nico Smets and their families became friends.

I would like to thank Katrien Van Slambrouck, Koen Michielsen, Lin Zhou and Kathleen Vunckx of the nuclear medicine group for helping me out with all aspects regarding image reconstruction and programming in IDL. In particular, I am thankful to Katrien for her valuable insights, the scientific discussions and the corrections of my equations whenever required.

The disciplines of cardiology and radiology are represented in the Medical Imaging Research Center by many kind people. I am indebted to Ruta Jasaityte for her emotional support and the various cultural discoveries she exposed me to. I am grateful to Xóchitl Lopez Rendon for offering refreshing walks and attempting to teach me some Spanish, and to Valérie Robesyn for providing sporting relief by encouraging me to go swimming, cycling and running and even to participate in a trio triathlon. For their ever warming smiles, I would like to thank Andre La Gerche, Matilda Larsson and Emmy Shaheen.

I had the pleasure of collaborating with several other research groups. In particular I would like to thank Olivia Nackaerts, Greet Kerckhofs, Gregory Pyka, Greetje Vande Velde, Jeroen Van Dessel and Yan Huang for the most agreeable collaborations and good company at scientific events.

Finally, I would like to thank my family for their incessant support, even when that meant seeing me less frequently. My most heartfelt gratitude goes to Elise, Albina and Jessica, whose coming and going have somehow helped me to find some meaning in this absurd world.

Maarten

Abstract

A better understanding of the complex mechanisms regulating bone development, homeostasis and repair will certainly result in improved therapies for numerous bone disorders. Such mechanisms are under investigation in small animal models, whose internal 3D bone structure and vasculature can be imaged with X-ray micro-computed tomography (μCT). While μCT imaging offers various opportunities, challenges such as the effect of X-ray radiation, segmentation of low dose images and the joint visualisation of bone and vasculature require investigation.

In this study, we developed methodologies that address several of the remaining challenges. To enable longitudinal follow-up of bone architecture, in vivo μCT acquisition protocols were developed that do not induce any major radiation side effects. The new protocols administer limited radiation doses to the animals, which results in μCT images of reduced image quality, manifested by blurring and intensity inhomogeneity. To accurately segment these degraded images, a simultaneous reconstruction and segmentation (SRS) approach was pursued. In our approach, an iterative MAP reconstruction technique that can model the μCT system blurring is applied, while a segmentation is obtained by enforcing the novel minimal entropy prior that limits the amount of intensities in the reconstruction. The presented SRS algorithm yields more accurate morphometric trabecular bone parameters than threshold-based segmentation methods.

The vascular network can be imaged by μCT through perfusion of the animal with a contrast agent typically containing a K-edge element. The contrast increases the density of the vasculature, making it visible but harder to distinguish from bone. A novel iterative dual energy reconstruction method was developed that models the material attenuation as a sum of Compton scatter, photoelectric effect and K-edge material basis functions. By enforcing a relationship between Compton scatter and photoelectric effect basis functions as observed in common substances, basis function coefficients can be computed

and a discrimination between bone and contrast is achieved. This approach performs better than a typical post-reconstruction dual energy approach with respect to noise and beam-hardening. Visualisation and quantification software was developed that enables joint 3D visualisation of vasculature and bone as well as the drawing of quantitative conclusions.

In conclusion, μCT imaging is a valuable tool in bone and other preclinical research. In this study, we examined and enhanced the μCT bone imaging and image analysis processes, we developed novel algorithms and analysis software, and we applied the imaging methodologies to answer relevant bone research questions.

Beknopte samenvatting

Een beter begrip van de ingewikkelde mechanismen in botontwikkeling, bothomeostase en botherstel leiden ongetwijfeld tot verbeterde therapieën voor verscheidene botafwijkingen. Deze mechanismen worden onderzocht in kleine proefdieren, wiens interne 3D botstructuur en bloedvaten onderzocht kunnen worden met behulp van X-ray micro-computed tomography (μCT) beeldvorming. Hoewel μCT beeldvorming een duidelijke meerwaarde biedt, vereisen uitdagingen zoals het effect van bestraling, segmentatie van lage dosis beelden en de gezamenlijke visualisatie van bot en vasculatuur verder onderzoek.

In deze studie ontwikkelden we methodes die zich richten op verscheidene van de uitdagingen. Om longitudinale opvolging van botarchitectuur mogelijk te maken, werden in vivo μCT opnameprotocollen ontwikkeld waarbij de bestraling geen noemenswaardige neveneffecten opwekt. De nieuwe protocollen dienen minder bestralingsdosis toe aan het proefdier en leiden tot μCT beelden van beperktere beeldkwaliteit, zichtbaar aan vage randen en intensiteits-inhomogeniteiten in het beeld. Om deze beelden nauwkeurig te segmenteren werd een simultane reconstructie en segmentatie (SRS) aanpak gevolgd. Onze methode past een iteratieve MAP reconstructie techniek toe die rekening houdt met de beperkte ruimtelijke resolutie van het μCT systeem, en resulteert in een segmentatie onder invloed van de nieuwe minimale entropie prior die het aantal intensiteiten in het reconstructiebeeld beperkt. Het voorgestelde SRS algoritme leidt tot nauwkeurigere morfometrische botparameters dan segmentatiemethodes gebaseerd op drempelwaarden.

Het vasculair netwerk kan onderzocht worden met μCT mits perfusie van het proefdier met een contraststof die meestal een K-edge element bevat. De constraststof verhoogt de dichtheid van de vasculatuur, waardoor het zichtbaar maar moeilijker te onderscheiden van bot wordt. Een nieuw iteratief dual energy reconstructie algoritme werd ontwikkeld dat de attenuatie modelleert als een som van Comptonverstrooiing, foto-elektrisch effect en K-edge element

basis functies. Door het toepassen van een verband geobserveerd in gangbare weefsels tussen de basis functies van Comptonverstrooiing en het foto-elektrisch effect, kunnen basis functie coëfficiënten bepaald worden en wordt een onderscheid tussen bot en contraststof verkregen. Deze aanpak presteert beter dan een gebruikelijke post-reconstructie dual energy techniek betreffende ruis en verharding van de X-stralenbundel. Visualisatie- en kwantificatiesoftware werd ontwikkeld die toelaat om zowel bot en bloedvaten samen te visualiseren als om kwantitatieve besluiten te trekken.

We besluiten dat μCT een waardevolle beeldvormingstechniek in bot- en ander preklinisch onderzoek. In deze studie onderzochten en verbeterden we de μCT botbeeldvormings- en beeldverwerkingsprocessen, ontwikkelden we nieuwe algoritmes en analysesoftware, en pasten we de beeldvormingsmethodologieën toe op relevante vraagstukken in het botonderzoek.

List of acronyms

μCT	X-ray micro-computed tomography
2D	two-dimensional
3D	three-dimensional
BS	bone surface
BV	bone volume
BV/TV	bone volume fraction
Ct.Ar	cortical bone area
Ct.Th	cortical thickness
FOV	field of view
FWHM	full-width-at-half-maximum
KO	knockout
M-CSF	macrophage colony-stimulating factor
MAP	maximum a posteriori
MAPTR	maximum a posteriori for transmission
ML	maximum likelihood
MLTR	maximum likelihood for transmission
Obj.N	number of unconnected objects
ORX	orchidectomised
OVX	ovariectomised
PSF	point spread function
RANKL	receptor activator of nuclear factor kappa-B ligand

ROI	region of interest
Sham	sham-operated
SRS	simultaneous reconstruction and segmentation
Tb.N	trabecular number
Tb.Sp	trabecular separation
Tb.Th	trabecular thickness
TRAP	tartrate-resistant acid phosphatase
Tt.Ar	total cross-sectional are
WT	wild type

List of Symbols

α_x	Energy dependent basis function x
$\bar{y_i}$	Estimated value at projection ray i
β	Prior strength
γ	Relative difference prior parameter
μ	Linear attenuation coefficient
σ_{tot}	Total atomic cross section
A	Histogram bins of the minimal entropy prior
a_x	Coefficient of basis function α_x
b_i	Photon counts in the blank projection ray i
K	Energy bins of the polychromatic spectrum
$L(\mu)$	Loglikelihood
l_{ij}	Intersection length of projection line i with voxel j
$P(\mu)$	Prior information
y_i	Measured value at projection ray i
E	Photon energy

Contents

Chapter 1

Introduction

1.1 Problem statement

Bone is continuously remodelled to maintain the optimal shape and structure of the bone throughout life. Understanding the mechanism of bone formation can provide key insights in the development of therapeutic strategies. Bone development, homeostasis (equilibrium) and repair require a normal vascular system that provides the bone with oxygen, nutrients and growth factors.

Blood vessels are in close physical contact with bone cells and molecular interactions between the two have been suggested. When blood circulation is inadequate during bone development or after bone injury, different types of bone cells are able to produce growth factors that stimulate the formation of new blood vessels (angiogenesis) to restore the oxygen supply [85]. Bone remodelling sites in both cortical and trabecular bone have been associated with the presence of capillaries [72]. The absence of vascularisation during the healing process of bone fractures results in unhealed bone, while treatment with growth factors stimulating angiogenesis enhances bone formation [128].

To obtain more insight in these matters, in vivo mouse models and detailed molecular analysis are required as well as accurate information on the three dimensional (3D) structure of blood vessels in relation to the trabecular bone structure. Such information can be obtained by 3D imaging.

X-ray micro-computed tomography (μCT) is a valuable tool to visualise the internal 3D structure of small objects. It is a non destructive technique, leaving the imaged sample available for analysis with complementary techniques. μCT

image intensities represent X-ray attenuation, providing a contrast especially suited to discriminate bone from soft tissue in small animals. With a resolution of up to a few μm, ex vivo μCT is able to resolve the thin trabecular bone structures of mice. The bone structures can be inspected visually in 2D or as a 3D model, and quantitative measures can be obtained by computing morphometric parameters from the images. New in vivo μCT systems enable imaging of living small animals at various time points, allowing monitoring of the consecutive changes in bone micro-architecture within the same animal. Such longitudinal studies can measure dynamic processes, lead to a more effective use of animal models and a reduced number of required animals.

1.2 Aims and objectives

Besides these advantages and opportunities offered by μCT imaging, the use of μCT imaging of small animals in vivo poses several challenges. μCT generates a 3D image of a sample by irradiating the sample with X-rays. Possible negative side effects from exposure to ionising radiation need to be analysed. A single μCT scan of a live animal does not cause any clear effects, but data on frequent in vivo exposure is lacking. As a first challenge, the effect of X-ray radiation on different ages of bone homeostasis should be examined.

To quantify changes in local bone architecture over time with image segmentation techniques, it is of importance that the segmentation is sufficiently accurate to detect subtle alterations. As limiting the radiation dose administered to the small animals reduces the image quality, it should be investigated how the accuracy of bone segmentation is affected by approaches to dose reduction. Therefore, a second challenge consists of developing a segmentation algorithm for low dose μCT images that enables accurate quantification of changes in bone structure.

To study the relationship between the vasculature and mineralised bone, joint 3D visualisation of the vascular tree and the bone architecture is of great interest. The vascular network can be imaged by μCT through perfusion of the animal with a suitable contrast agent. The contrast increases the density of the vasculature, making it visible but harder to distinguish from bone. As third challenge, a method to discriminate between bone and contrast agent should be developed, and quantitative measures describing the interaction between bone and blood vessels should be derived.

1.3 Main contributions

The main contributions of this thesis are the examination and enhancement of the μCT murine (i.e. of the mice) bone imaging and image analysis process, the development of novel algorithms and analysis software, and the application of these imaging methodologies to answer relevant bone research questions:

- The **acquisition** of projection data is optimised for in vivo follow-up of mouse bones with minimal radiation side effects.
- The **reconstruction** of in vivo projection data is modified to better model the physical reality, resulting in improved **segmentation** images of murine bone and more accurate **quantification** of in vivo bone morphology.
- The optimal **acquisition** settings for ex vivo dual energy imaging of bone and contrast agent are investigated, and a novel dual energy **reconstruction** and **segmentation** algorithm is developed to accommodate joint **visualisation** of bone and vasculature.
- The **biological relevance** of the proposed μCT imaging methods is illustrated by applying them to bone research questions. Dedicated analysis software for **visualisation** and **quantification** of various datasets is developed.

1.4 Outline

Chapter 2 of this thesis provides background information on bone and μCT. The properties of bone are revised, the benefit of animal models is explained, and the mouse disease models encountered in this work are introduced. Then the gold standard to image bone, histology, is discussed, followed by a detailed description of μCT imaging. Quantitative measures that describe bone structure are described.

Chapter 3 investigates the relationship between radiation dose and image quality, and proposes and validates in vivo μCT protocols that do not induce radiation side effects.

Chapter 4 investigates the limitations of threshold-based segmentation algorithms and presents a simultaneous reconstruction and segmentation method to segment low quality in vivo μCT images.

Chapter 5 develops a dual energy reconstruction algorithm that allows imaging vasculature and bone in 3D simultaneously. The method is compared to conventional post-reconstruction tissue decomposition and shown to exhibit improved noise properties.

The biological relevance of the developed algorithms is shown by applying them to specific bone research questions in Chapter 6. Congruences between μCT and histology images are investigated, vasculature properties are derived that distinguish between different disease conditions, and parameters that relevantly quantify bone healing in bone grafts are developed.

Chapter 7 draws some general conclusions and provides suggestions for future work.

Chapter 2

Imaging of murine bone architecture

2.1 Bone

The adult human skeleton consists of more than 200 bones in different shapes and forms: long bones such as the limbs, flat bones such as the skull, and irregular bones such as the hip or vertebrae. The main functions of bone are mechanical (protection of organs, providing structure and allowing motion by serving as levers for the muscles) and metabolic (as a reserve of ions, especially calcium and phosphate) [26].

Macroscopically, two types of bone organisation can be distinguished. Cortical bone is dense and solid, while trabecular or cancellous bone is highly porous. Trabecular bone is a honeycomb-like network of interconnected bony plates and bars, called trabeculae [26]. Long bones consist of a hollow tube, the diaphysis, of which the extremities end up in the metaphyses (Fig. 2.1). The metaphyses contain trabecular bone that is surrounded by a shell of cortical bone and include the cartilage growth plates. The rounded ends of the long bone also contain trabecular bone and are called epiphyses. To enhance locomotion, the bone surfaces at the joint sites are lined with articular cartilage. All remaining bone surface is covered with periosteum that contains blood vessels, nerve endings and bone-forming cells [26]. The normal functioning of bone tissue depends on an adequate supply of oxygen and nutrients through a network of blood vessels that is continuously adapted.

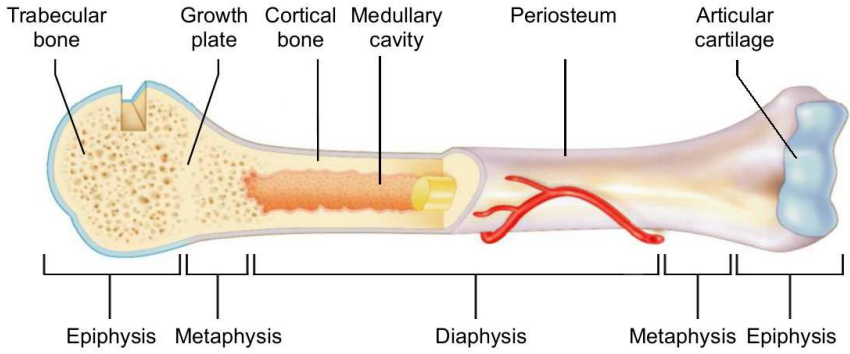

Figure 2.1: Schematic illustration of a long bone (adapted from [87]).

Microscopically, both cortical and trabecular bone are composed of the same basic structural units. They consist of a bone matrix upon which minerals such as calcium and phosphate can be deposited. The bone matrix is primarily a collagen fiber network that provides elasticity and flexibility to the bone and determines its structural organisation. The bone mineral that is deposited on the matrix and forms mineral crystals provides the mechanical strength of the bone [115].

Although macroscopically the skeleton appears to be static, it is an extremely dynamic tissue at the microscopic level. Bone is constantly broken down (bone resorption) and rebuilt (bone formation) in a continuous process called bone remodelling. Bone remodelling maintains the optimal shape and structure of the bone throughout life by responding to changes in loading conditions on the bone (bone structure is enhanced by exercise and compromised by disuse [117]). Small microcracks in the bone originated during cyclic loading regimes such as walking can be repaired and prevented from growing into a bone fracture. Additionally, bone remodelling can regulate the mineral content in the body by storing more or less calcium and phosphorus in the bone [26]. Bone remodelling occurs simultaneously at different sites in the skeleton.

Three different types of bone cells participate in the remodelling process. Osteoclasts resorb the bone by generating a very acidic environment that enables the dissolution of the mineralised bone matrix and by secreting enzymes that digest the bone matrix. Osteoblasts build the bone by synthesising the bone matrix and mineralising the generated bone matrix. This process results in the entrapment of the osteoblast within the generated bone matrix, and encapsulated osteoblasts differentiate into osteocytes. Osteocytes are

distributed throughout the bone matrix and are connected to each other by long extensions that occupy tiny canals in the bone matrix. Osteocytes are thought to be responsible for sensing mechanical strain and orchestrating signals to recruit osteoblasts and osteoclasts for maintenance, remodelling or healing of the bone. The sequence of events in a remodelling cycle is as follows: sensing of microcracks by osteocytes, recruitment of osteoblasts and osteoclasts to the site, bone resorption to remove damaged and old bone by osteoclasts, and finally new bone formation by osteoblasts to repair the defect [26].

2.2 Mouse models

Bone remodelling requires a careful balance between constant cycles of bone resorption and bone formation. When this balance is disturbed, pathologies such as osteoporosis or the imperfect healing of bone fractures may occur. To study the pathophysiology and mechanisms of human bone pathologies, they are replicated in mouse models.

Mice have become the preferred small animal model to study bone because of three reasons. First, mice and other rodents are genetically and pathophysiologically very similar to humans, facilitating translational research. Second, mice have a relatively short reproductive period, speeding up breeding of transgenic mice and reducing maintenance costs, compared to for example rats [33]. Third, the entire mouse genome was sequenced in 2002, making it the second mammalian species after the human to have its DNA sequenced [96]. The availability of their genetic information facilitates the creation of transgenic mice.

The genome is the entirety of an organism's hereditary information, which is encoded in DNA (or RNA for some viruses). The genome consists of both genes, i.e. specific sequences of DNA that encode a protein, and non-coding DNA sequences. Proteins are essential parts of organisms and participate in virtually every process within cells. Proteins catalyse biochemical reactions and regulate amongst others cell signaling, immune responses, cell adhesion, and the cell cycle.

In general, inbred mouse strains are used in laboratory experiments. Mice within an inbred strain have almost identical genotypes (manifestations of the genome) due to many generations of mating by genetically related parents. As a result, inbred mice express the same phenotypes and experiments with inbred mice have a higher reproducibility, and allow to distinguish genetic from environmental effects. The most widely used mouse strain is C57Bl/6, the strain whose genome was sequenced first [96].

By altering the genome of inbred mice and comparing these mice to mice with the unaltered genome, the role of a specific gene can be examined. Mice with an altered genetic sequence are called transgenic mice. The mice with the original, unaltered genome, are called wild type (WT) mice. Several different types of transgenic mice can be created. By inserting a gene sequence into a mouse, a transgenic mouse is created that overexpresses a certain gene, and the effect of this overexpression can be studied. Knockout (KO) mice, on the other hand, have an entirely inactivated gene. While this technique is very useful, essential genes that result in lethality of KO mice can not be analysed. Conditional knockout mice allow gene deletion in a tissue specific manner, inactivating the gene in only one type of cells. Inducible gene targeting can turn gene expression on or off by administering an inducer substance to the mice. With this approach, a gene can be turned on for a short period and then turned off again, in order to track gene function at specific developmental stages or cell differentiation stages [33].

By creating transgenic mice, genes can be overexpressed or inactivated, resulting in increased levels or lack of expression of the encoded protein. As proteins interact with many other molecules, a whole pathway of signals and effects will be influenced. Comparing the characteristics of transgenic mice with WT mice can provide a deeper understanding of pathways and interaction between different molecules, the physiological in vivo role of the gene of interest and lead to more targeted treatments.

Not all pathologies can be linked to a specific gene, however. By emulating the physical environment in which the pathology occurs in humans, such as a specific diet or stress, the pathology can be induced in animals. Generally, long bone pathologies are evaluated in the hindlimb bones: the tibia, or the shinbone, and femur, or thigh bone, although the vertebrae have been used as well. In this thesis we will come across bone pathologies like osteoporosis, fractures and certain therapies like bone grafts. These pathologies and how they are induced in animal models are discussed in the following sections.

2.2.1 Osteoporosis

Osteoporosis is the most common skeletal disease in the world and is characterised by a low bone mass and a deterioration in bone micro-architecture [59]. The reduction in bone strength associated with this disease markedly increases the risk of fractures, and the resulting pain and function loss strongly affect the quality of life. Osteoporosis is caused by a disturbance in bone cell regulation, leading to an increase in bone resorption rate without an equally strong increase in the rate of bone formation [109]. This type of

bone loss is observed in post-menopausal women, due to decreased estrogen levels. Osteoporosis may also occur in men due to a drop in testosterone [34].

Similar effects can be induced in the proximal tibia of female rats and mice by removing the ovaries [66]. Ovariectomised (OVX) mice are a well studied disease model and they display lower trabecular bone volume, decreased trabecular thickness and a lower trabecular number [1, 155].

In male rats and mice, the drop in testosterone can be prompted by orchidectomy, the removal of the testes. Orchidectomy (ORX) is known to decrease trabecular bone volume, while trabecular thickness remains unchanged [34]. ORX effects are more subtle than OVX effects, and therefore harder to detect.

Differences observed between OVX or ORX and unchallenged mice could be due to stress provoked by the operation or side effects of the anaesthesia. To exclude such environmental effects, OVX or ORX mice are compared to sham-operated (Sham) mice, which undergo the same surgical procedure but without the actual removal of the ovaries or testes.

2.2.2 Fracture repair

Bone is a unique tissue in its ability to regenerate its original structure and biomechanical integrity after simple fractures, if the fracture is stabilised. Fractures can arise by extreme mechanical loading, by stress through prolonged unusual loading requiring a too high remodelling rate, by bone pathologies that reduce the bone strength, or by trauma.

The process of fracture repair is comprised of four phases. First, an inflammatory response, associated with pain, heat and swelling, occurs. Bleeding of ruptured blood vessels is stopped by blood clotting. Inflammatory and stem cells are recruited to the fracture site. Second, stem cells and osteoprogenitors differentiate into osteoblasts which form immature bone. This process is especially present distant from the fracture site, where vessels from the periosteum can penetrate, and bone matrix is synthesised to form a hard callus. Closer to the fracture, no blood vessels are available and stem cells differentiate to chondrocytes that form the cartilaginous or soft callus. Third, the callus grows in size until both sides of the fracture unite and bridge the bone defect, resulting in an enhanced stabilisation. The cartilage is then transformed into trabecular bone, resulting in an entirely mineralised callus. Fourth, remodelling restores the large fracture callus to its original anatomical structure to support mechanical loads and the vascular supply returns to normal [95, 17]. This phase may take several years.

A bone fracture can be induced in mice by cutting the tibia into two parts with a diamond saw. A pin is entered into the bone to reproducibly stabilise the fracture. To study bone repair stimulation strategies, stem cells or growth factors may be injected in the fracture region. The condition with vehicle injections is called the control group.

2.2.3 Bone grafting

Large and complex bone defects may not heal naturally after stabilisation and result in non-unions. In such cases one may resort to bone grafting. In this surgical procedure a replacement material or graft is implanted at the bone defect to stimulate healing. The graft may be bone or synthetic material.

For successful bone healing, three key elements are considered to be required: a scaffold or graft that provides structure upon which bone can be deposited, relevant growth factors that can attract blood vessels or stimulate bone formation, and cells that can develop into bone cells [14]. Autografts, bone grafts harvested from the patient himself, provide the best healing properties and are the gold standard, as these grafts contain the optimal growth factors and cells, but they require a second operation site. Allografts, grafts obtained from another individual, are the most frequently chosen bone substitutes, but are rarely used fresh as they might ignite an immune response or transmit diseases. Freezing the allograft eliminates the cellular phase and hence lowers these risks, but the absence of appropriate cells impairs integration into the host bone. Allografts yield less satisfying and more variable results than autografts [40].

Bone grafts can be induced in mice by removing the mid-part of the femur and replacing it with a bone graft. To stabilise the graft, a pin may be inserted into the bone or an external fixator may be applied. Usually the allograft is seeded with different conditions of stem cells and growth factors before implantation.

2.3 Imaging of murine bone

In order to investigate the effect of certain proteins, pathologies or treatments on bone, characteristics of the bone have to be evaluated. While derived characteristics such as stress resistance or bone length can be measured relatively easily from the excised bone, they do not provide as much information as an image of the bone and its internal structure.

2.3.1 Histology

The traditional gold standard method of imaging the internal structure of bone, is by histological means. Histology allows for very specific cell and tissue staining, that can be imaged in high 2D resolution by microscopy. The histological procedure typically consists of embedding, sectioning and staining.

In order to section the bone, it is isolated from the animal and fixed to prevent cell degradation. Depending on the desired staining, the bone sample may be embedded in methylmethacrylate (MMA) or may be decalcified and embedded into paraffin. Subsequently the entire bone is sectioned into slices of 4 μm thick. In order to view certain tissues or cells, a staining method is applied to the bone sections to colour the tissues of interest. A tartrate-resistant acid phosphatase (TRAP) staining for example visualises osteoclasts [93], while Goldner staining colours mineralised bone green and unmineralised bone (osteoid) pink [43].

To visualise the calcium deposited in the bone matrix, the von Kossa staining protocol is applied [145]. The slices are hydrated to ameliorate dye penetration into the tissue. The slice is flooded with silver nitrate and left to rest in direct sunlight for one hour. During this process the silver attaches to the calcium salts and sunlight reduces the silver into a dark brown or black colour [91]. The result is a staining of the calcium, and consequently of the mineralised bone.

To enable quantification of tissue characteristics, the stained slices are photographed under a light microscope, typically with a pixel size in the order of magnitude of a few μm. An image of a von Kossa stained section that depicts the mineralised bone is shown in Figure 2.2(a). The ability of histology to capture functional information is illustrated in Figure 2.2(b): TRAP staining colours osteoclasts red. The histological process is very delicate and can generate artifacts in the form of small cracks.

As the histologic and histomorphometric analysis is very time consuming, typically the tissue characteristics are quantified in 3 to 5 sections of a long bone. Global morphometric indices have usually converged towards a nominal value after analysing those sections [110]. Histological imaging provides high resolution 2D images of a variety of tissues and bone cells. It is a destructive imaging method, and excising the bone from the animal and sectioning it, renders the bone sample unavailable for other analysis methods. Furthermore it provides only 2D information on the internal 3D structure of the bone sample.

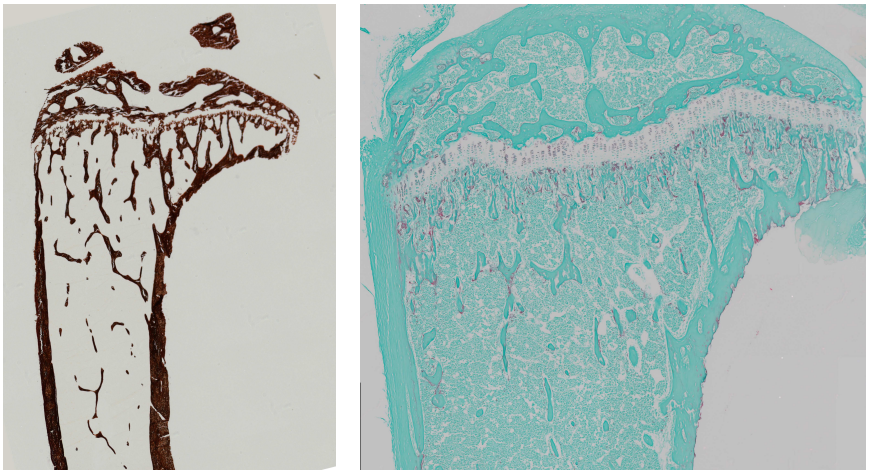

(a) (b)

Figure 2.2: Examples of stained histological images. (a) Von Kossa staining depicts mineralised bone. (b) TRAP staining colours osteoblasts red.

2.3.2 X-ray Micro-Computed Tomography

The 3D internal structure of objects can be visualised non-destructively with computed tomography (CT). CT is an imaging modality that produces cross-sectional images representing the X-ray attenuation properties of the object. An X-ray beam that travels through an object is attenuated by the X-ray attenuation properties of the object in its path, and the resulting modified X-ray beam is measured and converted to an electrical signal. From repeated measurements along a series of paths, the attenuation at each point in the object can be reconstructed, resulting in a 3D attenuation image of the object. CT is especially suited to image mineralised bone, as the calcium in bone has a very different X-ray attenuation from soft tissue. It has to be emphasised that when discussing bone with regards to μCT imaging, we mean the mineralised bone.

Clinical CT scanners provide reconstructed images with voxel sizes of approximately 1 mm [114]. In recent years, CT scanners have been scaled down to image much smaller structures. The term microCT, or μCT, has been used to describe CT systems that provide images with resolution in the micrometer range. Dedicated μCT systems to image live small animals are commercially available. Similarly, nanoCT systems have been developed with image voxel sizes in the nanometer range. These systems provide increased resolution at

the cost of a much smaller field of view and corresponding sample size.

Working with μCT systems provides several research advantages over working with clinical CT systems. As the system is used to scan animals rather than patients, more freedom in the adaptation of imaging protocols is allowed. In contrast to clinical or dental CT systems, the raw, unprocessed measurements are readily available.

In the following sections, the basic principles of CT are described.

X-rays

X-rays are electromagnetic waves. Electromagnetic radiation consists of elementary particles called photons. The energy E of a photon depends on its wavelength λ, or inversely its frequency ν:

$$E = \frac{hc}{\lambda} = h\nu \tag{2.1}$$

with $h = 6.626 \times 10^{-34}$Js Plank's constant and $c = 3 \times 10^{8}$m/s the speed of light. The energy of a photon is expressed in electronVolt (eV), which is the energy gained by an electron across an electric potential difference of 1V and equals 1.602×10^{-19}J. For μCT imaging of organic tissue, X-rays with photon energies between 8 keV and 100 keV are used, while for denser materials, such as rocks, photon energies may reach up to 225 keV. X-rays are ionising radiation, they have enough energy to knock electrons out of atoms, and can cause damage to living tissue.

X-rays can be generated in an X-ray tube, as shown in Figure 2.3. In this vacuum tube, electrons are released from a cathode and accelerated towards an anode by a potential difference called the tube voltage U. Upon hitting the anode, an electron can collide with:

an outer shell electron Part of the electron energy is transferred to the outer shell electron and is finally dissipated into heat. Due to this interaction, the anode must be cooled, making the size of the anode a trade-off between high resolution (small focal spot and limited cooling) and high power (larger focal spot but better cooling) [113].

a nucleus The electron is slowed down by particles in the nucleus, and releases a photon with energy equal to the lost kinetic energy. This causes a continuous energy spectrum called Bremsstrahlung. The photon energy is bounded by the maximum energy of the electron, which is U keV.

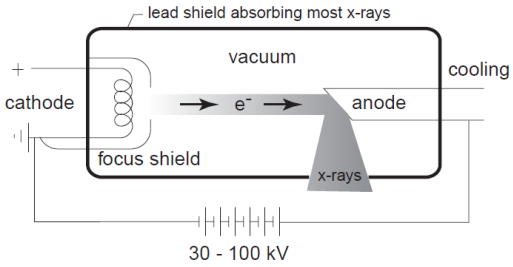

Figure 2.3: Schematic illustration of an X-ray tube [129]. Electrons are released from a cathode and accelerated towards an anode by a potential difference. As the electrons collide with the anode, X-rays are produced.

an inner shell electron The electron knocks the inner shell electron out of its shell, leaving a hole. An electron of a higher shell drops into the hole, releasing a photon with an energy of the difference in energy of the two shells. This results in peaks of specific energies in the X-ray spectrum, depending on the energies of the different shells and therefore on the anode material. This radiation is called characteristic radiation.

The important parameters of the X-ray tube are the tube voltage, which determines the maximum photon energy, and the tube current, which controls the amount of emitted photons. The intensity I of an X-ray beam is defined as the energy transmitted per unit time per unit area, and is proportional to the amount of X-ray photons. X-rays can also be generated in particle accelerators such as synchrotrons, by sending high-energy electrons through strong magnetic fields perpendicular to the beam.

Interaction of X-rays with matter

X-ray photons can interact with matter in several ways. At the X-ray energy ranges used in medical imaging, different types of interactions between photon and atom can occur.

Photoelectric effect The photon can be absorbed by the atom by using all of the photon's energy to knock an electron out of a shell. The electron is transmitted in the same direction the incoming photon was travelling.

Compton scatter The photon can transfer part of its energy to an electron. A photon with the remaining lower energy is emitted in a direction

different from the incoming photon. Additionally, the electron escapes in another direction.

Rayleigh scatter The photon can interact with an atom as a whole without exchange of energy. The photon is merely bounced away in an altered direction, but mainly maintains the forward direction.

Pair production At higher energies, the photon can interact with the nucleus and create an electron-positron pair. The photon energy should exceed the energy associated with the mass of the electron-positron pair, 1.022 MeV.

The probability of any of these effects occurring can be expressed by the cross section σ of that effect. The cross section is a hypothetical area measure that represents a surface, which prompts interaction if crossed by a photon. The cross section depends on the photon energy and on the chemical element of the atom. The total cross section of an atom σ_{tot} is simply the sum of the contributions of the different cross sections:

$$\sigma_{tot} = \sigma_{pe} + \sigma_{cs} + \sigma_{rs} + \sigma_{pp} \tag{2.2}$$

where σ_{pe} is the atomic photoelectric effect cross section, σ_{cs} is the Compton scatter cross section, σ_{rs} is the Rayleigh scatter cross section, and σ_{pp} is the pair production cross section [54].

The atomic photoelectric effect cross section of an element can be related to the element's atomic number Z by

$$\sigma_{pe} \propto \frac{Z^n}{E^3} \tag{2.3}$$

with E the photon energy and $n \approx 4$ [2]. Figure 2.4 plots the relative importance of the different photon-atom interactions for elements with varying atomic number at different photon energies. The lines mark equal strengths of the two neighbouring interactions. The energy range used in μCT imaging is shaded grey. As photoelectric and Compton cross sections account for the majority of the total cross sectional area, Rayleigh scatter and pair production are usually disregarded in medical imaging applications.

The total atomic cross section is related to the linear attenuation coefficient μ of an element, expressed in cm^{-1}, by

$$\mu = \mu_m \rho = \frac{\sigma_{tot}}{uA}\rho \tag{2.4}$$

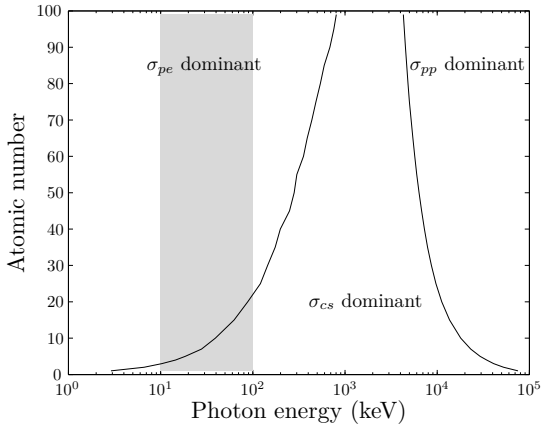

Figure 2.4: The relative importance of the photon-atom interactions for elements with varying atomic number Z at different photon energies. The lines indicate equal strengths of the two neighbouring interactions. The shaded region shows the energies used in μCT imaging of soft tissues.

with μ_m the mass attenuation coefficient, ρ the density of the element, u the atomic mass unit, and A the relative atomic mass of the element [55]. The linear attenuation coefficient can be interpreted as the fraction of an X-ray beam that is attenuated per unit distance of a material. Besides being a function of the material properties density and atomic mass, μ depends on the energy of the X-rays (Figure 2.5).

Most biological tissues are not pure elements. The mass attenuation coefficient of any mixture or compound can be computed according to

$$\mu_m = \sum_i w_i \left(\mu_m\right)_i \tag{2.5}$$

where w_i is the fraction by weight of the i^{th} atomic constituent [54]. The composition of various human tissues is described in [8]. Cross section and attenuation coefficient values for any element, compound or mixture can be obtained from the XCOM web database [7].

Figure 2.5 shows the attenuation of carbon and barium in the X-ray energy range of medical imaging. The linear attenuation coefficient of Barium exhibits a jump at 37.5 keV, due to the photoelectric effect. To knock an electron out of a shell, a photon with energy above the binding energy of that shell is required. As a result, X-rays with energy above this binding energy are more likely to be absorbed than X-rays below this binding energy. Such a discontinuity in the attenuation coefficient is called an absorption edge. The absorption edges

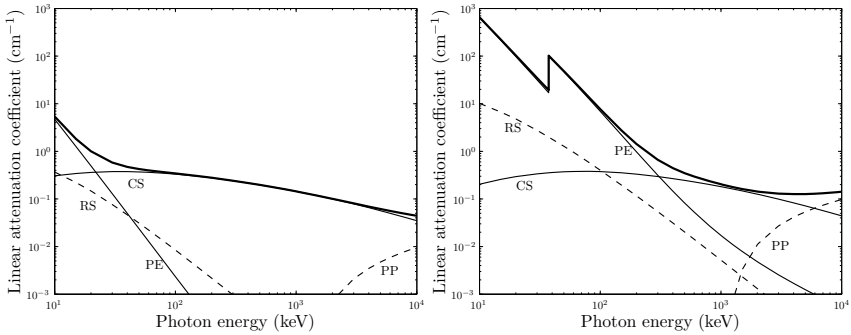

(a) Carbon (b) Barium

Figure 2.5: The linear attenuation coefficient μ of (a) carbon and (b) barium. The contributions of photoelectric effect (PE), Compton scatter (CS), Rayleigh scatter (RS) and pair production (PP) are labelled.

can be labeled according to the shell the electron belongs to. For example, the absorption edge associated with knocking an electron out of the innermost shell of the atom, the K-shell, is called the K-edge. All elements have K-edges, but elements with atomic numbers higher than 40 have their K-edge in the imaging range.

Consider an X-ray beam with intensity $I(0)$ travelling through an object with attenuation $\mu(s)$, s being the position along the X-ray beam line. The law of Beer-Lambert states that the intensity of the beam at any position x is given by

$$I(x) = I(0)e^{-\int_0^x \mu(s)\,\mathrm{d}s} \tag{2.6}$$

Although the interaction of a single photon with a single atom is of a statistical nature, the macroscopic intensity of the X-ray beam follows a deterministic exponential law. For polychromatic X-ray beams, the attenuation and intensity are function of the photon energy, and equation 2.6 becomes

$$I(x) = \int_0^{E_{max}} I(0,E)e^{-\int_0^x \mu(s,E)\,\mathrm{d}s}\,\mathrm{d}E \tag{2.7}$$

X-ray detectors

The X-ray beam that has been attenuated by an object has to be captured and converted to an electric signal to provide a digital image. This is done

in a device called the detector and while many types exist, modern scanners contain solid state detectors. Each sensor element of the detector consists of a scintillator coupled to a photodiode. The scintillator material absorbs X-rays and converts them into photons with a larger wavelength, in the range of visible light. The visible light then travels through the remainder of the scintillator material and hits the photodiode. The photodiode absorbs the light photons and produces an electric charge proportional to the photons' energy. During exposure, the electric charge is accumulated in the detector element. After exposure, the total charge is read out of each detector element. Flat panel detectors are created by stacking the photodiodes together into a charge-coupled device (CCD), and applying the scintillator, cut from a large crystal or ceramic, onto the pixel matrix [12].

The SkyScan μCT systems use solid state detectors. The scintillator is made out of a 25 μm thick slab of terbium doped (P43) gadolinium oxysulphide (Gd2O2S). Gadolinium oxysulfide in particular is used because it offers a very fast response time, meaning that almost no fluorescence is emitted after the X-ray exposure has ceased. This enables fast read-out times without corrupting measurements with fluorescence of the previous measurement. Photodiodes with a size of 12.5 x 12.5 μm^2 are stacked together in a matrix of, for the SkyScan 1076 μCT system, 4000 x 2000 pixels [18].

Current detectors give an estimate of the total detected energy over the exposure time, and are called energy integrating detectors. Photon counting detectors convert the X-ray photons directly to electrical charges. By connecting such semiconductors to an electronic circuit, the number of detected photons can be counted. Furthermore, as the charge is proportional to the energy of the photon, the energy of each photon can be stored, and spectral measurements are obtained. Photon counting detectors will become widely available the following years and make spectral imaging feasible.

Scanner geometry

μCT scanners have a cone-beam geometry. A single X-ray source is oriented towards a flat detector. The detector consists of a matrix of square detector elements. As a result, an entire volume can be measured in a single orbit.

We distinguish between ex vivo and in vivo μCT imaging. For ex vivo imaging, the sample is a piece of material or tissue, that can be positioned firmly in the field of view and rotated to obtain different projections at different angles. Typically, this setup allows varying the distances between tube, detector and sample, accommodating various magnification factors (Figure 2.6(a)).

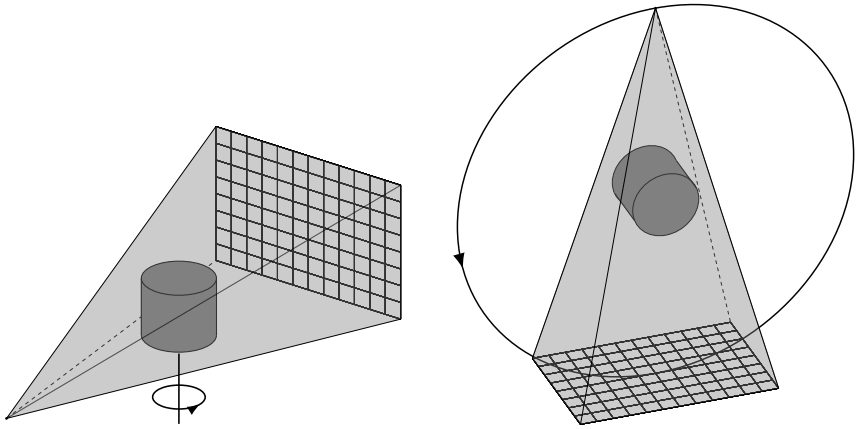

(a) (b)

Figure 2.6: (a) In the geometry of an ex vivo μCT system, the X-ray source and detector are fixed while the sample is rotated. (b) In the in vivo μCT geometry, the X-ray source and detector are rotated while the sample is fixed.

In vivo μCT systems are designed to scan living small animals, and the system geometry is adapted such that the animal does not need to be rotated. The animals are always anesthetised during a scan to prevent movement, and laid on a bed with access to anesthesia ducts, temperature control and cameras to ensure the well-being of the animal throughout the procedure. The source and the detector are mounted on a gantry which follows a circular trajectory around the animal to acquire projections at different angles. As the bed is fixed in the middle of the gantry, the magnification factor is fixed. Due to mechanical considerations the positioning of the gantry is less precise than simply rotating the sample, and ex vivo scanners provide higher resolution at equal magnification.

Data acquisition

At each position of the tube (in vivo μCT) or the sample (ex vivo μCT), a projection image of the sample onto the detector is acquired. Projection images are acquired at a set of projection angles, usually separated at a stepsize of approximately 1 degree and spanning 360 degrees. A lower angular stepsize results in a higher sampling density but requires longer scan times. A projection image of a mouse tibia is shown in Figure 2.7(a).

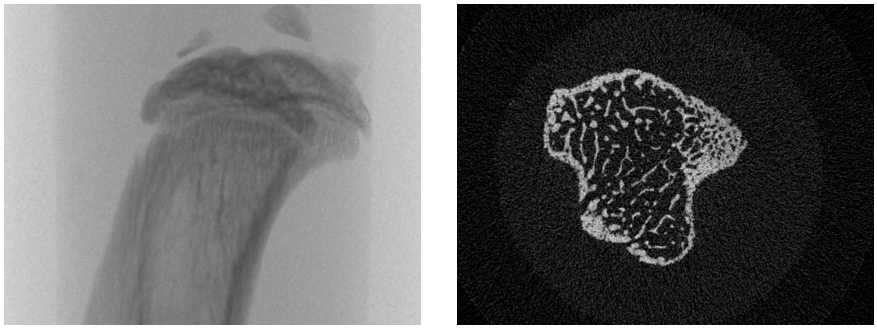

(a) (b)

Figure 2.7: μCT imaging of a mouse tibia. (a) A projection image. (b) A slice of the reconstruction reveals the internal 3D structure of the tibia.

The field of view (FOV) is the area in the centre of the scanner that is projected onto the detector in every projection direction. The FOV is the area that can be reconstructed, and the sample should be positioned in this area. If the sample is longer than a single FOV, the specimen can be moved axially and a second scan can be acquired. If the sample is wider than a single FOV, the magnification factor should be adjusted at the cost of resolution. Alternatively, some scanners can move the detector in the trans-axial plane and obtain a double FOV by stitching together two half projections.

A set of projection images is called consistent if an object exists that generates those projections under a certain projection model. Inconsistencies arise due to projection models that do not correspond to the physical reality during measurement. Inconsistencies in data can lead to artifacts in the resulting reconstructed object representation. Depending on the projection model, inconsistencies can be caused by noise, scatter, beam hardening, misalignment, photon starvation, variable detector element sensitivity and object motion. More details can be found in [3].

Provided that the detector is not saturated, noise in the projection image can be reduced by increasing the tube current, by increasing the exposure time over which the photons are integrated in the detector, or by averaging multiple projection images at the same angle. These all increase the amount of X-rays sent through the sample, and this higher dose might cause undesirable side effects in living tissue. The acquisition settings require a careful trade-off between administered dose and image quality. The relationship between dose and image quality is further investigated in Chapter 3. Noise can also be reduced by binning detector pixels, at the cost of image resolution.

Image reconstruction

Reconstruction is the process of computing the 3-dimensional density function from a set of 2-dimensional projections. An example reconstruction of a mouse tibia is shown in Figure 2.7(b). Reconstruction algorithms can be divided into two categories: analytical reconstruction techniques and iterative reconstruction techniques.

Analytical techniques rely on the analytic inversion of the Radon transform. The most popular cone-beam reconstruction algorithm is the FDK algorithm, named after the initials of its authors Feldkamp, Davis and Kress [35]. It consists of weighting, filtering and backprojecting the projection images. The formula is approximate, as cone-beam scans do not provide sufficient sampling for exact reconstruction, but performs reasonably well for small cone angles, is easy to implement and fast [52, 35].

Analytical methods are widely used because of their computational efficiency, but have a number of limitations. They generally ignore noise and other inconsistencies or treat them by preprocessing the projection images or postprocessing the resulting reconstruction. An analytical algorithm is applicable to a specific geometry, limiting practical use to standard geometries. Analytical formulations usually assume continuous measurements and sampling issues are treated by discretisation after the fact. Iterative reconstruction methods can overcome all these limitations, and due to recent increases in computational power are expected to become commonplace. Analytical methods remain useful for developing insight and intuition, and for studying properties of specific geometries.

Iterative reconstruction techniques start from discrete representations of both the reconstructed image and the projection measurement. A forward model relates the object with the measurement. The model attempts to describe the underlying physics, and can be made as accurate as desirable. Physical realities that can be incorporated are for example the polychromatic nature of the X-ray beam, the finite width of the beam, or the detector cross-talk [22]. A more accurate forward model generally results in increased reconstruction image quality, at the cost of a higher computation time.

Generally, iterative reconstruction techniques define an objective function and a method to optimise the objective function. Many different objective functions and optimisers exist, leading to, in the words of Fessler, “as many different methods for image reconstruction as there are researchers in the field. More in fact, because many researchers have proposed multiple methods” [36].

A typical objective function would encourage projections of the reconstructed

image to match the measured projections, and can incorporate noise models, prior information and regularisation constraints. Combined with the optimiser, this usually leads to an algorithm that starts from a uniform image that serves as estimate of the reconstruction, and iteratively refines this estimation. In each iteration the projections of the current reconstruction estimate are calculated and compared to the measured projections. A difference measure between current estimate projections and the measured projections is backprojected and added to the reconstruction estimate. This procedure is iterated until convergence, i.e. until the current calculated projections are equal to the measured projections. The major drawback of iterative reconstruction techniques is their computational complexity, taking 10 to 1000 times longer than analytical techniques. Iterative reconstruction is discussed in more detail in Chapter 4.

While the values of the reconstructed image represent attenuation expressed per cm, they can be transformed by a linear transformation to Hounsfield units. The Hounsfield unit (HU) of a voxel j is given by

$$HU_j = 1000 \frac{\mu_j - \mu_{water}}{\mu_{water}} \tag{2.8}$$

As a result, air has a HU of -1000 and water of 0 HU. Depending on the acquisition system and settings, the HU of bone will range from 400 to 1000 in clinical practice and can be up to 5000 for μCT images.

The aim of the reconstruction method is to obtain an image that represents the scanned object. Noise or blurry edges can be considered as artifacts introduced by the imaging process and do not belong in the true representation of the object. Consequently, higher image quality, characterised by amongst others the ability to detect small structures and the absence of noise, provides a better object representation. Given a set of projection images, the reconstruction algorithm attempts to obtain a reconstruction image with as high image quality as possible. Higher quality images facilitate accurate segmentation, essential to quantifying properties of the object.

2.4 Quantification of bone morphometry

While images of the internal bone structure provide a visual interpretation of the bone characteristics, quantitative measures allow a more thorough assessment. The standard method of quantitatively describing bone architecture is the calculation of morphometric indices [9]. Morphometric indices are computed from a binary image containing only bone and non-bone voxels. To obtain this binary image, the histology or μCT images have to be segmented.

Table 2.1: A set of important trabecular morphometric indices [9].

Trabecular index	Abbrev.	Description
Bone volume fraction	BV/TV	Ratio of the segmented bone volume to the volume of the ROI.
Trabecular thickness	Tb.Th	The mean thickness of trabeculae. It is the average of all the local thicknesses of the structure. The local thickness in every voxel of the bone is defined as the diameter of the largest sphere that fits within the object and encloses the voxel [50].
Trabecular separation	Tb.Sp	The mean distance between trabeculae. It can be computed by applying the thickness measurement to the background, the space between the bone.
Trabecular number	Tb.N	The average number of trabecular traversals per unit length.
Connectivity density	Conn.D	The degree of connectivity measured as the number of redundant trabecular connections per volume unit.

Table 2.2: A set of important cortical morphometric indices [9].

Cortical index	Abbrev.	Description
Total cross-sectional area	Tt.Ar	Total cross-sectional area inside the periosteal envelope.
Cortical bone area	Ct.Ar	Average cortical bone area.
Cortical thickness	Ct.Th	Average cortical thickness.

When the resolution and the signal-to-noise ratio of the image are high, as is the case for histology and ex vivo μCT images, the segmentation can be performed by global thresholding. More advanced segmentation methods are discussed in Chapter 4.

Due to the difference in structure between cortical and trabecular bone, they are assessed separately. Trabecular bone is usually evaluated in the metaphysis, and cortical bone in the diaphysis. Typically, a region of interest (ROI) is computed or delineated in which only trabecular or cortical bone is present. The bone in this ROI is then characterised with either cortical or trabecular morphometric indices. A set of important trabecular indices is given in Table 2.1, and cortical indices are described in Table 2.2.

As bone structure cannot be fully understood unless described in 3D terms, it is recommended to report morphometric indices in 3D [105]. Certain measurements on 2D histologic images can be straightforwardly extrapolated to

3D indices. For example, multiplying the 2D bone perimeter and 2D bone area with the slice thickness provides measurements for the 3D bone surface (BS) and bone volume (BV). Some morphometric indices, such as the 3D trabecular thickness, can only be computed indirectly from histological images by making assumptions about the 3D structure of the bone. Typical assumptions are that all the trabeculae are either plates (the plate model) or cylindrical rods (the rod model) [106]. As these assumptions introduce bias if the object deviates from the model, morphometric indices computed in 3D are more accurate [9].

2.5 Imaging of murine bone vasculature

Besides imaging bone and quantifying its characteristics, the relationship between bone and vasculature is of interest. To study this interaction, images of the vascular structure have to be obtained.

2.5.1 Histology

CD31 is a protein that is highly expressed on the surface of endothelial cells, which line the inner surface of blood vessels. Endothelial cells can be detected by staining tissue sections with an antibody that specifically binds to CD31, and visualised by adding a substrate that reacts with the antibody [142]. The resulting brown staining of the inner blood vessel layer can be seen around a tumour and within bone in Figure 2.8. This approach is called immunohistochemistry in reference to the usage of antibodies. This histological technique yields high resolution images, but is time consuming, destructive, and provides only 2D information.

2.5.2 X-ray Micro-Computed Tomography

The contrast in μCT images is provided by the linear attenuation coefficient of the scanned objects. As blood and blood vessels have attenuation coefficients similar to soft tissue, a regular CT scan does not provide any contrast to visualise the blood vessels. To discriminate blood, the attenuation of blood can be altered by perfusing the vasculature system with a contrast agent based on an element with a high atomic number Z, such as iodine (Z=53), barium (Z=56), gold (Z=79) or lead (Z=82).

For in vivo imaging of vasculature, contrast agents that are non-toxic and that clear out of the body are used. Typically iodine based contrast agents

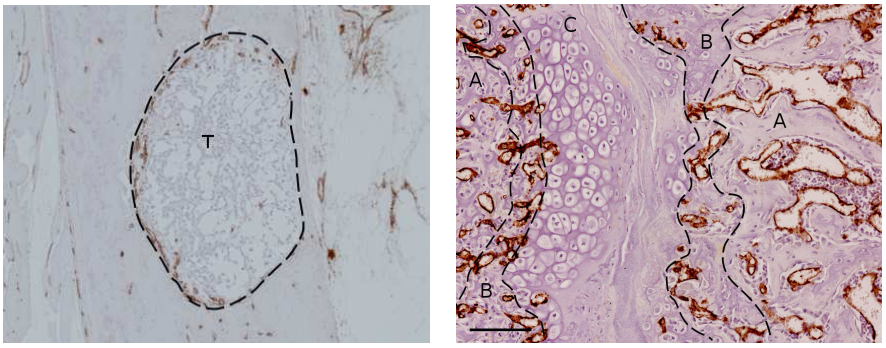

(a) (b)

Figure 2.8: CD31 stained histological images indicate the circumference of blood vessels in brown (a) around a tumour (denoted by T) and (b) within bone. Region C is cartilage, free from any blood vessels. In the cartilage remodeling zones (B), small blood vessels intrude into the cartilage, while in the newly formed bone (A), large blood vessels are present.

clear out of the body through liver and spleen in a few hours, resulting in the majority of commercially available μCT scanners not being fast enough to capture the images without some contrast medium clearance out of the blood vessels. Contrast agents based on gold nanoparticles that stay in the body for up to 24 hours have been developed to improve this [13].

For higher resolution imaging of the vasculature, the tissue of interest is excised and scanned in an ex vivo scanner. In this case measures are taken to keep the contrast agent in the blood vessels, as clearance is now undesirable. Less stringent constraints are placed on contrast agents compared to in vivo imaging, as toxicity of the contrast is irrelevant. The scientific community is divided as to whether barium sulfate or commercial lead based contrast Microfil (Flow Tech Inc., MA, USA) yields best results. After extensive testing, our experience has led us to opt for barium sulfate contrast agents. Figure 2.9 shows a projection image and a reconstructed slice of a mouse hindlimb perfused with barium sulfate.

Small animals perfused with contrast agents based on lead or barium display high variability in attenuation of the contrast agent, even within the same vessel [88]. The high variability makes it hard to discriminate contrast agent from bone, which has a similar attenuation coefficient (see Fig. 2.9(b)). Techniques to discriminate bone from vasculature are discussed in Chapter 5.

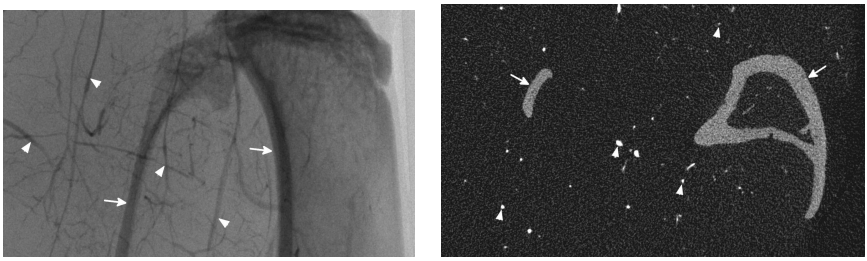

(a) Projection image (b) Reconstructed slice

Figure 2.9: Illustration of perfusion of a mouse hindlimb with barium sulfate. (a) A projection image with a clearly visible vascular tree. (b) A slice of the reconstruction contains both bone and barium sulfate, although they are not easily distinguishable on an intensity basis. Arrows indicate bone structures, triangles indicate blood vessels.

2.6 Conclusion

In this chapter the function, composition and structure of bone are revised. To study bone, pathologies are replicated in transgenic mice and induced in mouse disease models. Conventionally the structure of murine bone and accompanying vasculature was studied using histology, but now μCT systems provide a non-destructive method to visualise the internal 3D structure. The basic concepts and underlying physical processes of μCT imaging are explained, noting in particular that there is a trade-off between dose and image quality, and that the reconstruction algorithm influences the image quality.

Chapter 3

In vivo μCT protocols without major radiation side effects

3.1 Introduction

In vivo μCT has been suggested as a valuable tool to monitor local changes in bone structure in living mice [61]. This technology can offer unique high resolution information on the temporal responses of specific bone regions to pathological or therapeutic stimuli, stipulated that the μCT imaging process itself has no influence on the skeletal system. Indeed, frequent or excessive exposure of the skeletal system to X-rays leads to side effects which are closely related to the radiation dose and include growth retardation, skeletal deformities, bone loss and hematological abnormalities [153, 94].

Radiation can cause cell death, most likely as a consequence of irreparable DNA damage [57, 103]. But also low radiation doses can result in non-lethal DNA damage, which will initiate DNA repair processes and ultimately lead to a decrease in cell proliferation [58]. It is therefore generally accepted that proliferating cells are more radiosensitive than non-proliferating cells and that less differentiated cells are more prone to radiation damage than highly

This chapter is based on the publication: K. Laperre*, M. Depypere*, N. van Gastel, S. Torrekens, K. Moermans, R. Bogaerts, F. Maes, G. Carmeliet, Development of μCT protocols for in vivo follow-up of mouse bone architecture without major radiation side effects, Bone, vol. 49, no. 4, pp. 613-622, 2011, * equal contribution. Reused with permission from Elsevier.

differentiated cells [127]. This radiation-induced cytotoxicity has resulted in the use of radiation as a local therapy for numerous malignancies in humans.

Radiation will also harm non-malignant cells and several studies have investigated the effects of high-dose radiation on bone cells in vitro and in vivo. X-ray radiation in the range of 2.5 to 8 Gy inhibits the proliferation and activity of osteoblasts [31, 90, 21, 39] and osteoclasts [120], while radiation doses lower than 2 Gy have a stimulatory effect on osteoclast proliferation and activity [152]. Growth plate chondrocytes and bone marrow cells are the most radiation sensitive cells because of their high proliferation rate, and radiation damage to these types of cells inhibits their proliferation and thus results in growth retardation and myeloid depletion, respectively [153, 53]. On the other hand, the exposure of the total mouse body to a low dose radiation of 75 mGy was found to stimulate the proliferation of bone marrow hematopoietic progenitor cells as well as their mobilisation into the peripheral blood [78].

In contrast to the radiation doses used in radiation therapy, the doses associated with imaging are substantially lower. To investigate the temporal changes in bone structure during a longitudinal followup study, multiple successive μCT scans are, however, required. Frequent in vivo μCT imaging, even with relatively low radiation doses per scan, can still affect bone architecture. Discrepant results have been reported concerning the effects of μCT-induced radiation on the bone micro-architecture and especially the hematopoietic system in rodents. In rats, 8 weekly in vivo scans of 939 mGy each did not alter the structural bone parameters nor the viability of the bone marrow cells [11]. In mice, however, μCT-induced radiation decreased trabecular bone volume of the tibiae of 8 to 10-week old mice after 4 weekly scans with 846 mGy [69], while 4 weekly scans with 1255 mGy did not exacerbate disuse-related bone loss in the femurs of 17-week old mice [63]. It is still unclear whether this inconsistency should be attributed to differences in the radiation dose, frequency and number of in vivo scans or a combination of these. In addition, young, growing animals may be particularly susceptible to radiation exposure [9]. Certainly in humans, this age-related radiation sensitivity has already been thoroughly described [94].

Taken together, it is critical to delineate the settings for in vivo μCT imaging of the bone architecture of mice in order to avoid side effects on bone and hematopoietic cells that could result in altered bone structure and hematological defects. However, lowering the radiation dose to avoid radiation effects may increase noise in the images and decrease the signal-to-noise ratio, or reduce image sharpness and lower the resolution [38]. Hence, image quality needs to be weighed against the radiation risks [42]. This trade-off between dose and image quality has not been investigated thoroughly in relation to in vivo μCT imaging of mouse bone architecture. In this study, we designed 2 protocols for longitudinal μCT studies of the skeletal system in young pre-

pubertal and adult mice that are devoid of radiation-induced side effects and maintain adequate image quality.

3.2 Materials and methods

3.2.1 Animals and experimental design

Male C57Bl/6 mice (Janvier) were housed under standard conditions in our animal facility (Proefdierencentrum Leuven, Belgium). All procedures were approved by the Ethical Committee of the Katholieke Universiteit Leuven.

Three types of experiments were performed: a pilot experiment, an optimisation experiment and a validation experiment. In each experiment, the left hindlimb of male C57Bl/6 mice, anesthetised with isoflurane, was scanned in vivo with μCT at 3 consecutive time points, separated each time by a 2-week interval. This followup period of 4 weeks was chosen because it corresponds with the evaluation period used in several murine bone pathology models such as ovariectomy, castration, tail suspension and fracture repair. The right hindlimb was positioned out of the field of view of the μCT and served as the non-irradiated control, as the total X-ray exposure of this hindlimb was negligible (data not shown). Following the last in vivo scan, mice were sacrificed by cervical dislocation and, depending on the experiment, blood was collected and the spleen, tibia and femur were isolated.

In the pilot experiment, we investigated the radiation effect of the recommended μCT parameters on 10-week old male C57Bl/6 mice (n=5), an age often used as starting point in bone pathology models. The in vivo μCT parameters were 9 μm pixel size, 50 kV, 120 μA, 0.5 mm Al filter, angular rotation step 0.9°, 220 projections and an exposure time of 4.7 s with a total scan duration of 19 min. After sacrifice, dissected tibiae were imaged by ex vivo μCT after overnight fixation in 2% paraformaldehyde, and then processed for histological analysis.

In the optimisation experiment, 4 and 16-week old male C57Bl/6 mice were analysed, as age is known to change the susceptibility to radiation effects (n=4 per age group). For each age, an additional group of mice was included, referred to as 'reference' group, and these mice were anesthetised at each time point but did not receive any in vivo radiation (n=4 per age group). Two in vivo μCT parameters were used: (i) a pixel size of 9 μm(50 kV, 100 μA, 1 mm Al filter, angular rotation step 1°, 199 projections, exposure time 3.3 s, scan duration 12 min); (ii) a pixel size of 18 μm (50 kV, 100 μA, 1 mm Al filter, angular rotation step 0.8°, 248 projections, exposure time 1 s, scan duration 5 min). After sacrifice, the bone architecture was analysed by ex vivo μCT

and histology. Peripheral blood cell counts were determined and the in vitro colony forming capacity of hematopoietic progenitor cells of the bone marrow and spleen was analysed. The in vitro osteogenic potential of bone marrow stromal cells and the differentiation of bone marrow hematopoietic cells into osteoclasts were assessed.

In the validation experiment, 10-week old male C57Bl/6 mice were either sham-operated or orchidectomised the day before the first in vivo μCT scan was taken (n=5 per group). They were anesthetized with pentobarbitone sodium (Nembutal, 50 mg/kg body weight, CEVA Sante Animale) and received buprenorfine hydrochloride as postoperative analgesic (Temgesic, 0.05 mg/kg body weight, Schering-Plough). The in vivo μCT parameters were the 9 μm pixel size parameters used in the optimisation experiment, and trabecular bone architecture was analysed and compared between orchidectomised and sham-operated mice over time.

3.2.2 Micro-computed tomography

The bone micro-architecture of the tibiae was assessed ex vivo and in vivo using a SkyScan 1172 and a SkyScan 1076 μCT system, respectively, and related software (SkyScan). In vivo μCT images were segmented using an adaptive thresholding algorithm provided by the SkyScan CTan software because the reduced image quality precluded the use of global thresholding [73]. The local threshold was calculated in a circular region of radius 8 pixels around each pixel (see Section 4.2.2). When indicated, registration software based on mutual information was applied to align these images [86].

The scanning parameters for all ex vivo μCT imaging experiments were 5 μm pixel size, 50 kV, 200 μA, 321 projections, 0.5 mm Al filter. After reconstruction, the ex vivo μCT images were segmented using a global threshold. The global threshold was visually determined to optimally separate the bimodal histogram into bone and soft tissue. Trabecular and cortical volumes of interest were selected manually and histomorphometric parameters were calculated according to the 'Guidelines for the assessment of bone microstructure in rodents using μCT' [9].

3.2.3 Image quality

Image quality can be quantified by several factors such as resolution and signal-to-noise ratio. Resolution describes the ability to resolve small details in the image and can be quantified as the full-width- at-half-maximum of the

system point spread function [64]. The signal-to-noise ratio in μCT images of the different protocols is measured as the ratio of the mean intensity over the standard deviation of the intensity in a region of interest in images of a homogeneous water phantom. More details about image quality and its relationship to radiation dose can be found in [42].

3.2.4 Histological analysis

Tibiae were fixed in 2% paraformaldehyde, decalcified in 0.5 MEDTA (pH 7.4)/PBS prior to dehydration, embedded in paraffin, and sectioned at 5 μm. Hematoxylin-eosin (H&E) staining and staining for tartrate-resistant acid phosphatase (TRAP) activity were performed as previously described [84, 82] and were used to quantify osteoblast surface and osteoclast surface per bone surface, respectively. When indicated, bones were fixed in Burckhardt's solution, embedded undecalcified in methyl-metacrylate, sectioned at 4 μm and stained according to Von Kossa to visualise the mineralised bone matrix. Histomorphometric analysis was performed using a Zeiss Axiovert microscope and related Axiovision software (v6.1.0). Histomorphometric data were expressed according to the American Society for Bone and Mineral Research standardised histomorphometry nomenclature [105].

3.2.5 Radiation dose

The radiation dose was estimated by measuring the air kerma with a 0.6 cm^3 thimble ionisation chamber that has a calibration factor traceable to a standard dosimetry lab (PTB, Braunschweig). The ionisation chamber (type FC-65-G, IBA Dosimetry) was placed in air at the centre of rotation of the scanner, resulting in an estimate of the radiation dose by means of the air kerma value. The reported radiation doses are not corrected for tissue surrounding the bone and are not representative values for radiation delivered to the bone.

3.2.6 In vitro assays

The colony forming capacity of hematopoietic progenitor cells was analysed on bone marrow cells, flushed from the femur, and on spleen cells which were isolated by gently pressing the spleen through a 70 μm nylon mesh cell strainer (Becton Dickinson). The Methocult assay (StemCell Technologies) was performed as described before [83]. Bone marrow stromal cells isolated from tibiae and femora were cultured according to the method described previously.

Osteogenic differentiation was analysed after 2 and 3 weeks of culture by alkaline phosphatase or alizarin red staining [89]. Osteoclast formation was performed as described previously, using macrophage colony-stimulating factor (M-CSF) and receptor activator of nuclear factor kappa-B ligand (RANKL) treatment [79] and the number of TRAP-positive cells with more than three nuclei were counted as osteoclasts [20]. Cell counts (white and red blood cells and blood platelets) in peripheral blood were quantified using an Abbott Cell-Dyn 3500 hematology analyser.

3.2.7 Statistics

Results are expressed as mean±SEM (standard error of the mean), unless stated otherwise. Data were analysed by one-way ANOVA and paired t-test using NCSS software (NCSS). Post hoc comparisons were performed using Fisher's least significant difference test. Differences were considered significant at $p<0.05$.

3.3 Results

3.3.1 Doses of 776 mGy induce trabecular bone loss

To investigate whether repetitive exposure to in vivo μCT imaging, using recommended scanning parameters, might have an effect on bone architecture, we compared in a pilot experiment the bone architecture of the in vivo irradiated left tibia to the non-irradiated right tibia that served as control. The used scanning parameters resulted in a total radiation dose of 776 mGy per scan.

Analysis of the bone volume by ex vivo μCT imaging of the dissected tibiae showed that the in vivo μCT-induced radiation decreased trabecular bone volume by 30% in the irradiated tibia compared to the non-irradiated control tibia (Figs. 3.1A,B). This reduction was caused by a decrease in trabecular number (Figs. 3.1A,C), whereas trabecular thickness was not altered by the frequent CT scanning (Figs. 3.1A,D). Cortical bone mass and structure were not affected by the μCT-induced radiation as the total cross-sectional area (Fig. 3.1E), the cortical bone area (Fig. 3.1F) and cortical thickness (Fig. 3.1G) were normal.

An imbalance between osteoblast-mediated bone formation and osteoclast-mediated bone resorption is generally the cause of a decreased bone mass.

Histomorphometric analysis showed that the decrease in trabecular bone volume was associated with increased bone resorption as TRAP staining revealed an increase in the osteoclast surface per bone surface in the irradiated tibiae compared to control tibiae (Fig. 3.1H). Bone formation, on the other hand, seemed unaltered as the osteoblast surface per bone surface, quantified on H&E stained sections, remained unchanged after in vivo irradiation (Fig. 3.1I).

These data indicate that administration of three in vivo μCT radiation doses of 776 mGy, given with a two week time interval, negatively affects bone mass in young adult mice.

3.3.2 Lowering radiation dose reduces image quality

Because the suggested scanning parameters induced radiation-related changes in bone architecture, we performed an optimisation experiment in which the scanning settings were adapted in order to deliver the lowest possible radiation dose while maintaining acceptable image quality. To reduce scan duration, the angular rotation step was increased and the exposure time decreased. The current of the X-ray source was lowered and a thicker filter was used to reduce the radiation dose per unit of time. The adapted parameter set resulted in a radiation dose of 434 mGy per scan for a 9 μm pixel size scan. Further lowering of the radiation dose was achieved by decreasing the exposure time and combining 4 detector camera pixels to obtain an image pixel size of 18 μm, resulting in a radiation dose of 166 mGy per scan.

We first evaluated the effect of lowering the radiation dose on the quality of the obtained images. Ex vivo μCT images were taken as a reference, because the image quality achieved with this method is comparable to the one obtained in stained histological sections. Indeed, comparison between a registered ex vivo μCT image (Fig. 3.2A) and a von Kossa-stained histological section (Fig. 3.2B) revealed that the bone structures, as visualized by each of these techniques, were matching closely.

As anticipated, the quality of the in vivo μCT images was reduced when the radiation dose was decreased. Scanning with a dose of 434 mGy and a pixel size of 9 μm resulted in more blurred images compared to the ex vivo μCT scan, as demonstrated by the registration of the ex vivo and in vivo μCT images of the same tibia (Figs. 3.2C,D). Image quality was degraded even more when the bone was scanned using the protocol with a pixel size of 18 μm and a radiation dose of 166 mGy (Fig. 3.2E). The signal-to-noise ratio of 1.78 for the 9 μm protocol increased to 2.79 for the 18 μm pixel size protocol, while the resolution of 36 μm deteriorated to 57 μm. The slightly improved noise characteristics of the 18 μm pixel size protocol indicate

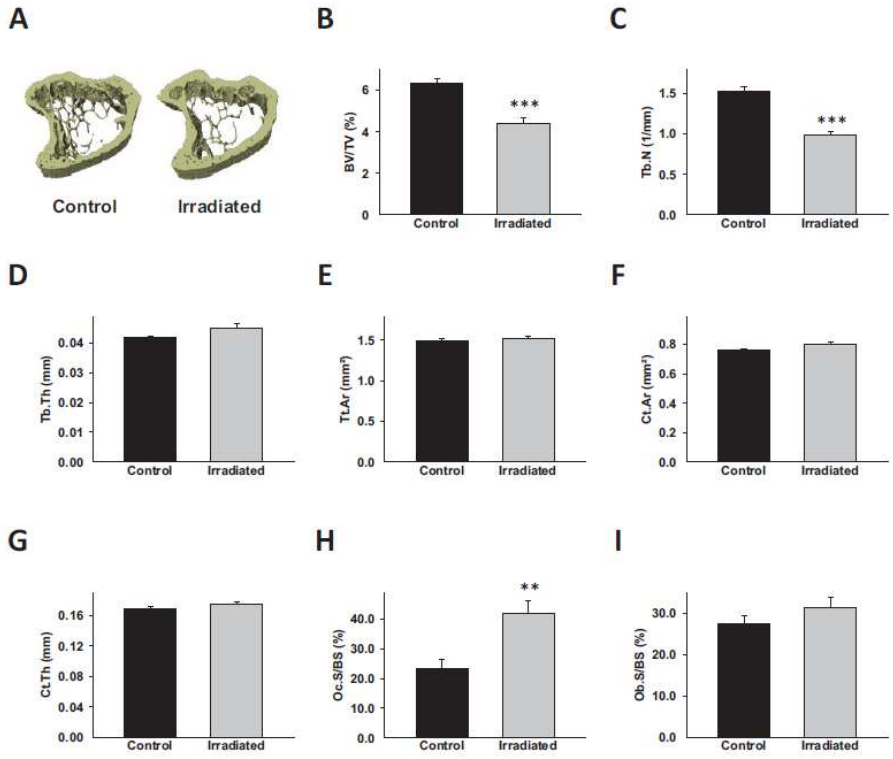

Figure 3.1: Trabecular bone mass is reduced by 3 two-weekly in vivo μCT scans with a radiation dose of 776 mGy. (A) Representative 3D μCT images of metaphyseal bone structure of the non-irradiated right (control) and irradiated left tibia of the same mouse. (B−G) Quantification of trabecular bone volume relative to tissue volume (B; BV/TV), trabecular number (C; Tb.N), trabecular thickness (D; Tb.Th), total cross-sectional area (E; Tt.Ar), cortical bone area (F; Ct.Ar) and cortical thickness (G; Ct.Th) of the non-irradiated (control) and irradiated tibiae. (H−I) Quantification of the osteoclast surface per bone surface (H; Oc.S/BS) and osteoblast surface per bone surface (I; Ob.S/BS) on histological sections of non-irradiated (control) and irradiated tibiae after TRAP or H&E-staining, respectively. ** $p<0.01$; *** $p<0.001$ (t-test, vs control; n=5).

that the observed quality difference can mainly be attributed to the lower resolution due to the increased pixel size. This quality difference was also reflected in the quantification of the trabecular and cortical bone parameters. In vivo μCT imaging with 18 μm, and to a lesser extent 9 μm pixel size, overestimated trabecular bone volume (Fig. 3.2F) and trabecular thickness (Fig. 3.2H) compared to ex vivo μCT imaging, but underestimated the number of trabeculae (Fig. 3.2G). The quantification of the cortical parameters was less influenced by the in vivo scanning protocols: the total cross-sectional area (Fig. 3.2I) and the cortical bone area (Fig. 3.2J) quantified from the 9 and 18 μm pixel size in vivo scans did not differ significantly from those quantified from the ex vivo scans. Similar to the trabecular thickness, cortical thickness (Fig. 3.2K) was overestimated by the in vivo scanning protocols.

In conclusion, the two developed protocols for in vivo μCT imaging resulted in a low radiation dose, but inevitably also reduced the image quality and rendered accurate quantification of the bone parameters more difficult.

3.3.3 Bone structure is not significantly altered by repeated 434 mGy imaging

Next, we investigated whether these adapted protocols for in vivo μCT imaging had less or even no toxic effects on trabecular and cortical bone volume. Young pre-pubertal mice (4 weeks of age) and adult mice (16 weeks of age) were subjected 3 times to one of the 2 protocols. We included the group of growing mice, since it is known that, at least in humans, young individuals are more sensitive to radiation than older persons [94]. As before, the effect of radiation on bone mass and structure was analysed by quantifying the bone parameters in the left irradiated and right non-irradiated tibia with ex vivo μCT imaging. To avoid that inter-individual variations in bone architecture between the left and right tibia masked the effect of radiation, the difference in bone parameters between the left and right tibia was calculated for each mouse and compared between the radiated group and the non-irradiated group that served as reference.

Repeated in vivo μCT imaging at 9 or 18 μm pixel size had no significant effect on the trabecular (Figs. 3.3A−C) or cortical (Figs. 3.3D−F) bone parameters, irrespective of the age of the mice, as the data were comparable to the results obtained in the non-scanned reference group. Some minor side effects of in vivo μCT radiation doses of 434 mGy (9 μm) were however detected in pre-pubertal as well as adult mice (Fig. 3.3A). The difference in trabecular bone volume between the left irradiated and right non-irradiated tibia was negative in every mouse, indicating that trabecular mass tended to decrease in the in

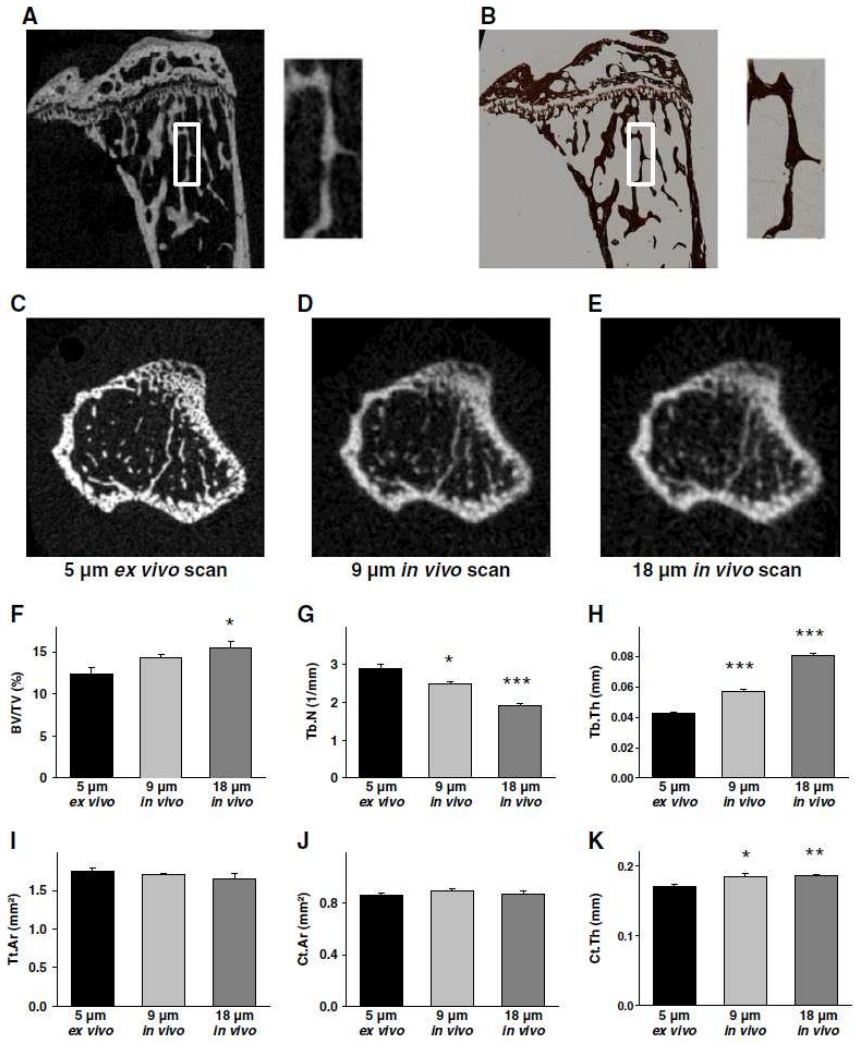

Figure 3.2: Lowering the radiation dose reduces image quality. (A−B) Registered images of a tibia scanned ex vivo at 5 μm pixel size (A) and a Von Kossa-stained section after histological processing (B). (C−E) Registered images of the tibial metaphysis scanned ex vivo at 5 μm pixel size (C), in vivo at 9 μm pixel size (D) or in vivo at 18 μm pixel size (E) showing a decrease in image quality with reduced radiation dose. (F−K) Quantification of BV/TV, Tb.N, Tb.Th, Tt.Ar, Ct.Ar and Ct.Th of tibiae scanned with the above acquisition settings. * $p<0.05$; ** $p<0.01$; *** $p<0.001$.

vivo scanned tibia, although not significantly. This decrease was mainly due to a reduction in trabecular number (Fig. 3.3B) without an effect on trabecular thickness (Fig. 3.3C).

To ascertain that the effects of the 434 mGy μCT radiation dose on bone mass were minimal or even negligible, we analysed osteoblast-mediated bone formation and osteoclast-mediated bone resorption. To this end, we performed histomorphometry of the irradiated and non-irradiated control tibia of pre-pubertal mice that were in vivo scanned at 9 μm pixel size. We reasoned that a possible negative effect of radiation would be most marked in the youngest group receiving the highest radiation dose. No significant changes were, however, observed in the osteoblast surface (Figs. 3.4A,B) or osteoclast surface (Figs. 3.4C,D) which were quantified on HE- or TRAP-stained sections, respectively. These in vivo findings were confirmed by in vitro analyses. No differences were observed in the number and size of the osteogenic colonies formed by bone marrow stromal cells derived from pre-pubertal reference mice or mice that were in vivo scanned at 9 μm pixel size (Fig. 3.5A). Furthermore, bone marrow hematopoietic cells, treated with M-CSF and RANKL, differentiated equally well to osteoclasts in vitro (Fig. 3.5B).

In summary, repeated in vivo exposure to μCT radiation doses of 434 mGy did not significantly affect bone formation or resorption, and trabecular and cortical bone parameters were thus not altered.

3.3.4 In vivo μCT radiation doses of 434 mGy are not deleterious to hematopoietic bone marrow cells

In vivo μCT imaging of the long bones inevitably results in radiation exposure of the bone marrow harbouring the hematopoietic (stem and progenitor) cells. In vivo μCT imaging may thus indirectly influence the number of progenitors in the spleen and the number (and type) of circulating blood cells [71]. Colony forming assay of hematopoietic cells revealed that in vivo μCT imaging with 9 or 18 μm pixel size (434 or 166 mGy respectively) did not alter the number of granulocyte, macrophage or granulocyte-macrophage colony forming units in the bone marrow isolated from irradiated femora (Table 3.1) or in the spleen from irradiated mice (data not shown), irrespective of the age of the mice. These data are in line with a previous report showing that in vivo exposure of neonatal or adult mice with a single dose of 500 mGy did not induce long-term impairment of haematopoiesis [44]. Furthermore, the number of white blood cells, red blood cells and blood platelets in peripheral blood was unaffected by the in vivo μCT radiation (Table 3.2).

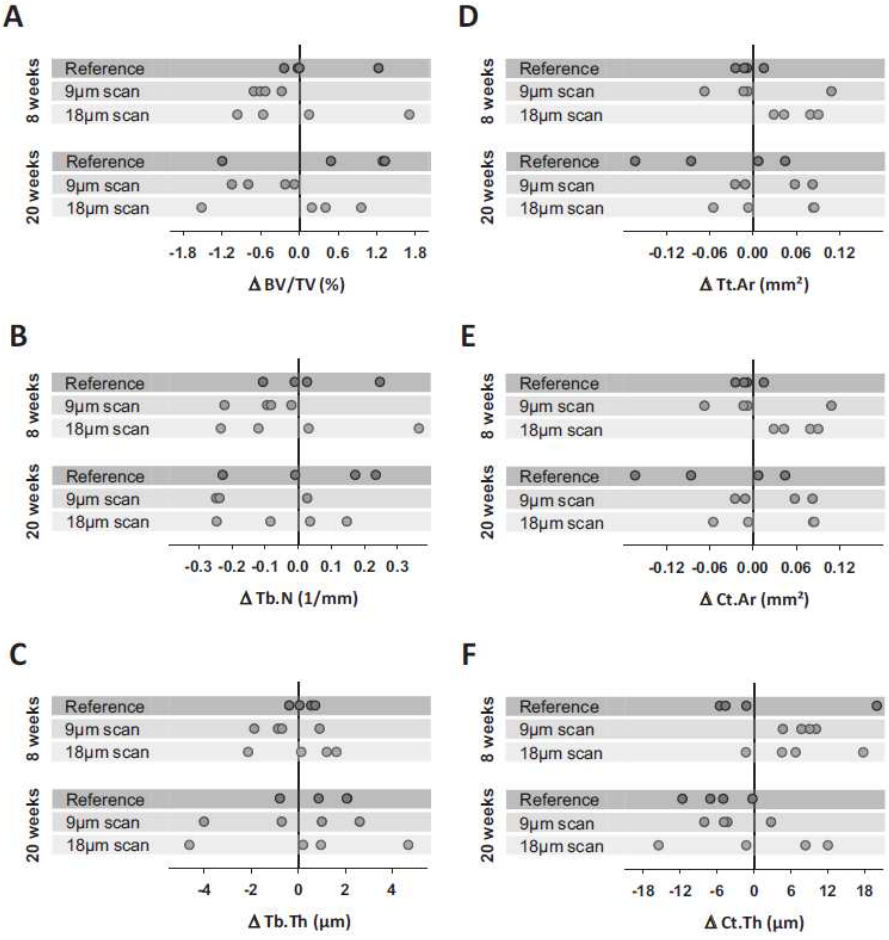

Figure 3.3: Bone structure is not altered by multiple in vivo radiation doses of 434 mGy. The left tibia of young (8 weeks) or adult (20 weeks) mice was repetitively scanned in vivo at 9 or 18 μm pixel size, or not scanned (reference). The difference in trabecular and cortical bone parameters between the left and right tibia was calculated for each mouse and represented in a dot plot: difference in trabecular bone volume relative to tissue volume (A; ΔBV/TV), trabecular number (B; ΔTb.N), trabecular thickness (C;Δ Tb.th), total cross-sectional area (D; ΔTt.Ar), cortical bone area (E; ΔCt.Ar) and cortical thickness (F; ΔCt.Th).

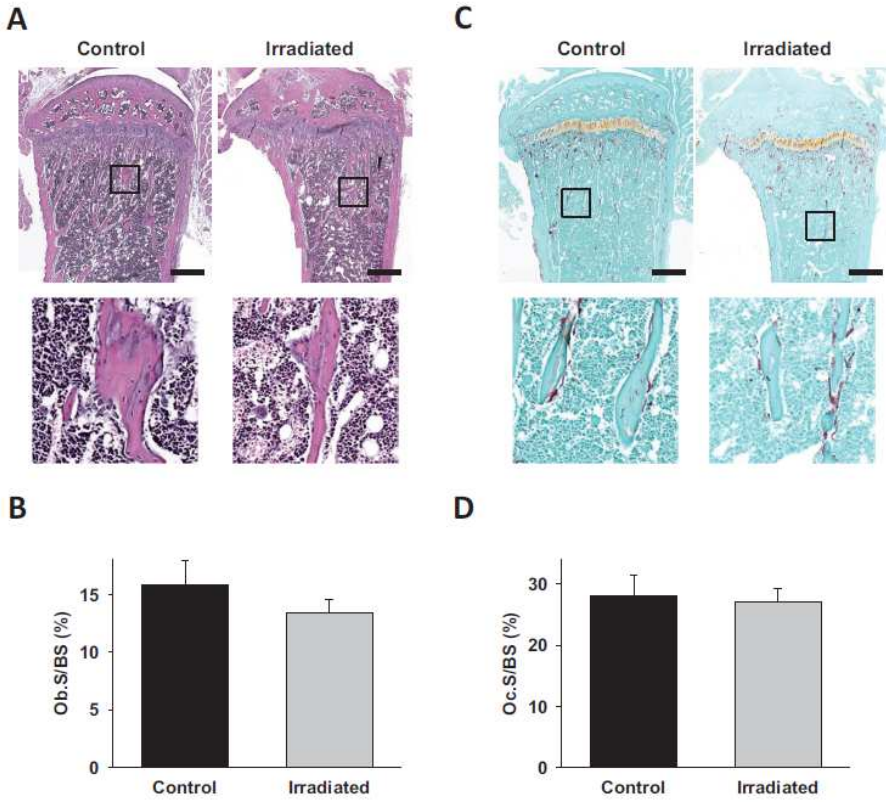

Figure 3.4: Bone formation and resorption are not altered by multiple in vivo radiation doses of 434 mGy. (A−B) H&E staining on histological sections of the non-irradiated (control) or in vivo scanned tibiae (9 μm) of pre-pubertal mice (A, overview in top panel, higher magnification of boxed area in lower panel). Quantification of osteoblast surface per bone surface (B; Ob.S/BS). (C−D) TRAP-staining on histological sections of non-irradiated (control) or in vivo scanned tibiae (9 μm) of pre-pubertal mice (C, overview in top panel, higher magnification of boxed area in lower panel). Quantification of osteoclast surface per bone surface (D; Oc.S/BS). Scale bar = 500 μm.

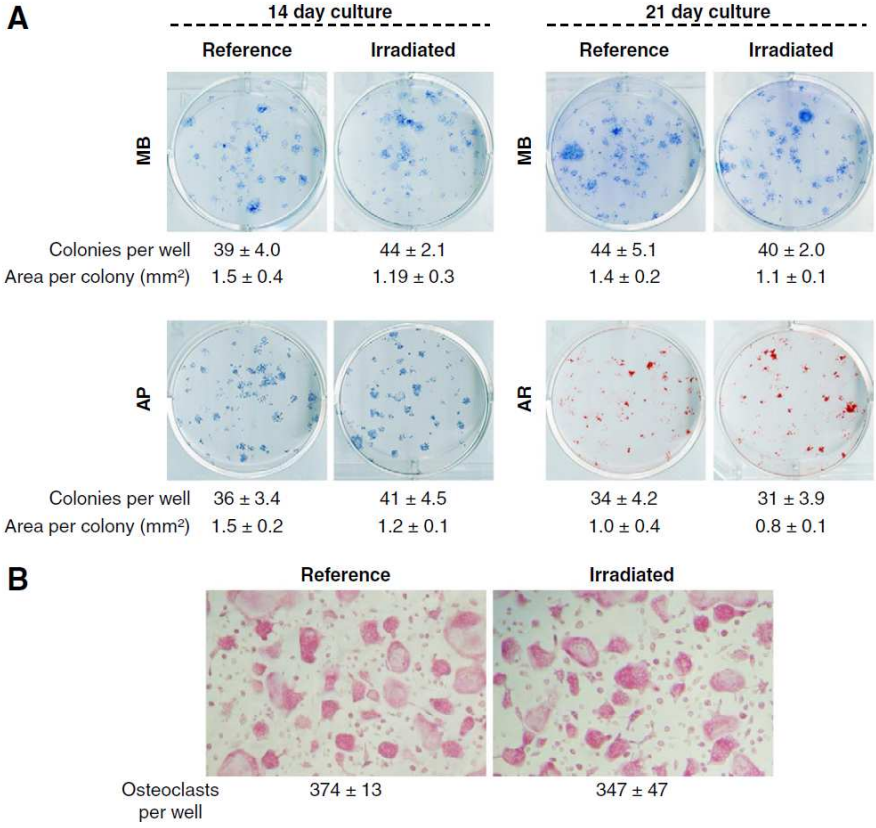

Figure 3.5: Multiple in vivo radiation doses of 434 mGy do not affect colony forming capacity of bone marrow cells or osteoclast differentiation. (A) Representative images of methylene blue, alkaline phosphatase and alizarin red staining of bone marrow stromal cell cultures derived from non-irradiated (reference) or in vivo scanned tibiae (9 μm) of pre-pubertal mice after 14 or 21 days of culture with quantification of the number of osteogenic colonies per well and the average area per colony (t-test, vs reference group; n=3). (B) Representative images of TRAP-stained osteoclasts differentiated from hematopoietic bone marrow cells derived from non-irradiated (reference) or in vivo scanned (9 μm) tibiae of pre-pubertal mice formed after 1 week of culture with quantification of the number of osteoclasts formed per well.

Table 3.1: Number of granulocyte (G), macrophage (M) and granulocyte-macrophage (GM) colony forming units (CFU) per 10^4 bone marrow cells isolated from femora of 8- or 20- week-old mice that were not in vivo scanned (reference) or scanned at 9 or 18 μm pixel size.

Age	Colony type	Reference	9 μm in vivo scan	18 μm in vivo scan
8 weeks	CFU-G	17.5 ± 0.9	14.8 ± 2.7	17.8 ± 1.7
	CFU-M	18.5 ± 2.4	15.3 ± 2.7	15.0 ± 0.7
	CFU-GM	13.5 ± 12.5	12.3 ± 1.7	12.5 ± 1.5
	Total CFU	49.0 ± 4.8	42.3 ± 5.4	45.3 ± 2.4
20 weeks	CFU-G	16.3 ± 3.4	18.0 ± 1.9	21.3 ± 1.9
	CFU-M	17.0 ± 4.7	16.8 ± 3.0	18.8 ± 2.2
	CFU-GM	14.3 ± 3.4	13.5 ± 2.2	15.3 ± 1.9
	Total CFU	47.5 ± 11.2	48.3 ± 5.2	55.3 ± 4.9

Table 3.2: Number of white blood cells (WBC), red blood cells (RBC) and blood platelets (BPL) in peripheral blood isolated from 8- or 10-week-old mice that were not in vivo scanned (reference) or scanned at 9 or 18 μm pixel size.

Age	Colony type	Reference	9 μm in vivo scan	18 μm in vivo scan
8 weeks	WBC (x $10^3/\mu$l)	2.4 ± 0.4	2.5 ± 0.5	3.0 ± 0.3
	RBC (x $10^3/\mu$l)	9.4 ± 0.1	9.2 ± 0.2	9.2 ± 0.3
	BPL (x $10^3/\mu$l)	1580 ± 20.1	1530 ± 27.8	1471 ± 55.2
20 weeks	WBC (x $10^3/\mu$l)	2.6 ± 0.5	2.7 ± 0.5	2.2 ± 0.4
	RBC (x $10^3/\mu$l)	9.1 ± 0.2	8.8 ± 0.1	7.9 ± 0.7
	BPL (x $10^3/\mu$l)	1516 ± 92.2	1428 ± 99.3	961 ± 190.9

Taken together, repetitive in vivo exposure to μCT radiation doses of up to 434 mGy did not affect hematopoietic progenitor activity.

3.3.5 The 434 mGy protocol enables longitudinal follow-up of trabecular bone loss after orchidectomy

Since the developed μCT imaging protocols had no obvious radiation effects, we next investigated whether they were suitable to monitor changes in bone architecture during longitudinal follow-up studies (validation experiment). We therefore analysed bone loss over time after orchidectomy, a male osteoporosis model, via in vivo μCT scanning using the 434 mGy protocol. Orchidectomy (ORX) is known to decrease trabecular bone volume, while trabecular thickness remains unchanged [77, 34].

The 3D μCT images of the tibiae of sham-operated mice, obtained at 3 consecutive time points, showed the normal age-related decrease in trabecular

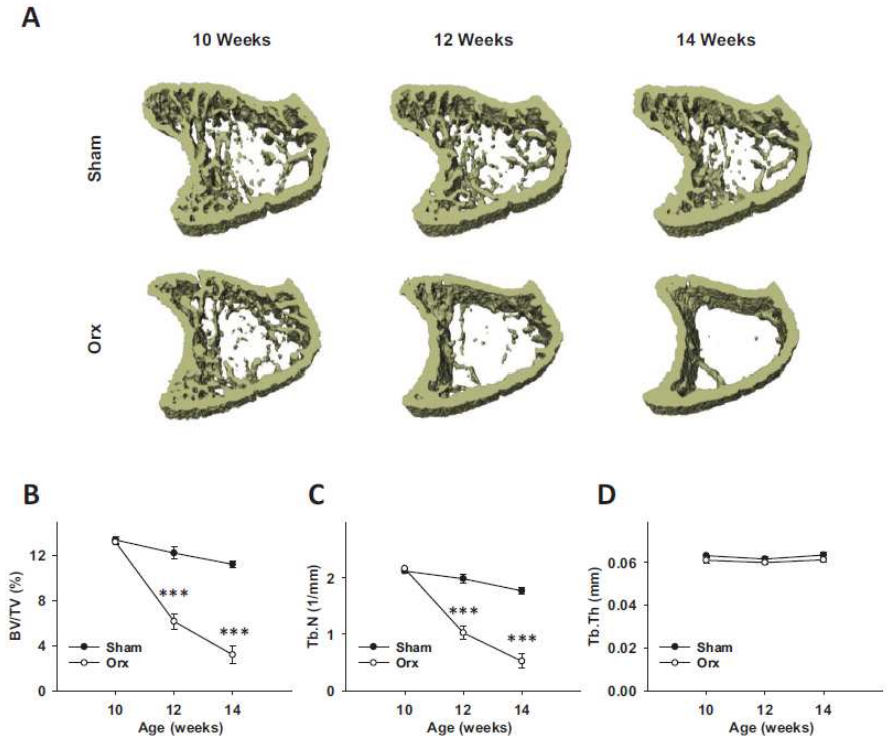

Figure 3.6: The 9 μm in vivo μCT imaging protocol enables longitudinal follow-up of trabecular bone loss after orchidectomy. (A) 3D μCT models of Sham or ORX mice, analysed by in vivo μCT imaging at the time of the operation (10 weeks of age) or 2 and 4 weeks after the procedure. (B−D) Quantification of trabecular bone volume (B; BV/TV), trabecular number (C; Tb.N) and trabecular thickness (D; Tb.Th). *** $p<0.001$.

bone mass (Fig. 3.6A). In contrast, trabecular bone volume manifestly decreased over time in orchidectomised mice (Fig. 3.6A). Quantification showed a 50% decrease of trabecular bone volume (Fig. 3.6B) and trabecular number (Fig. 3.6C) 2 weeks after orchidectomy and a 70% decrease of both parameters after 4 weeks. Trabecular thickness did not vary over time after orchidectomy (Fig. 3.6D).

In conclusion, the proposed 434 mGy μCT imaging protocol yields images that are of sufficient quality to quantitatively monitor changes in trabecular bone architecture over time in vivo.

3.4 Discussion

In vivo imaging of animals has multiple advantages, but the radiation exposure is a cause of major concern in any longitudinal in vivo μCT imaging study of the long bones of mice. Indeed, we could confirm that an ill-considered choice of μCT imaging parameters decreased trabecular bone mass manifestly. We therefore developed and validated two in vivo μCT imaging protocols, which are devoid of clear radiation-induced side effects, and enabled us to quantitatively follow-up trabecular and cortical bone architecture over a 4-week period in mice.

The benefits of in vivo μCT scanning of bone architecture in mice compared to ex vivo imaging are patently obvious [9]. In vivo μCT imaging allows the follow-up of time-dependent changes in three-dimensional bone structure within the same animal. Registration of the sequential 3D images provides unique information on the precise sites of bone formation or bone resorption [10, 98, 146]. In addition, longitudinal studies inherently reduce the number of animals to be used. Moreover, each animal can be used as its own control, which decreases the variability and thus increases the statistical power. Possible applications are numerous and include changes in bone architecture, linked to a gene defect or caused by therapeutic intervention, besides many others. The significance and added value of these in vivo follow-up experiments, however, depend on the μCT scanning protocol that should be devoid of radiation-induced side effects. Ideally, the actual radiation dose delivered to the bone tissue should be known, but this parameter is hard to determine because it requires that the tissues surrounding the bone are simulated by a phantom. In this study, we therefore used the radiation doses measured in air (air kerma values), omitting the need for a phantom. The advantage of this approach is that these measurements are easily reproducible, which facilitates comparisons with other studies, including those referred to in this study [11, 69].

We developed a 9 and 18 μm pixel size in vivo μCT imaging protocol resulting in a radiation dose of 434 mGy and 166 mGy per scan, respectively. We showed that these two protocols had no significant radiation-induced side effects on trabecular and cortical bone architecture or on the analysed hematological parameters. The higher radiation dose tended to decrease the trabecular bone volume, but no clear changes in bone formation or bone resorption were detected by histomorphometry, indicating that the radiation-induced effects were minimal. These in vivo findings were confirmed by in vitro analyses showing that the osteogenic differentiation of bone marrow osteoprogenitors as well as osteoclast formation from bone marrow osteoclast precursors was not reduced by the in vivo μCT scanning protocol. These findings, nevertheless, suggest that a μCT radiation dose of 434 mGy is close to the limit of safely using

in vivo imaging. Indeed, repeated in vivo μCT imaging with a higher radiation dose (776 mGy in this study, 846 mGy in Ref. [69]) decreased trabecular bone volume significantly, most likely due to increased bone resorption as shown by an increase in the osteoclast abundance. It should also be noted that this limit is likely species-specific because radiation-induced toxicity was not observed in rats even with higher radiation doses. Indeed, eight in vivo scans with a radiation dose of 939 mGy per scan and a 1-week interval [11] or five in vivo scans with a radiation dose of 597 mGy and a 2-week interval [69] did not cause any changes in the bone architecture of rats.

The drawback of a reduced radiation dose is that the image quality is correspondingly decreased. As the signal-to-noise ratio obtained with the 9 μm pixel size protocol is slightly lower than that of the 18 μm pixel size protocol, the larger pixel size in the 18 μm protocol compensates for the increased noise, which is expected by the dose reduction. The apparent reduced image quality of the in vivo protocols can mainly be attributed to the lower resolution of the images and is manifested by blurring and associated intensity inhomogeneity. These effects should be taken into account by the bone segmentation process in order to minimise errors in estimates of structural bone parameters. Selecting a global threshold value to segment the bone ignores these image distortions and should be avoided as segmentation method for low-dose images. Local thresholding approaches attempt to account for intensity inhomogeneities by computing a local threshold value for every pixel, and can model blurring by adapting the thresholds in blurred regions [147]. Local thresholding methods are relatively fast and readily available, but can only handle limited image degradation. In the presence of large image degradation, such as in the images obtained with the 18 μm pixel size protocol, the local thresholding method used in this study tended to consider thin trabeculae as bone marrow because of their low intensity and the segmentation of thin trabeculae might thus fail. As a result, the number of trabeculae is likely to be underscored and the mean thickness of the trabeculae is likely to be overrated in these images. However, such segmentation errors can be considered to occur systematically within a study and therefore do not need to preclude correct relative comparisons between groups and over time, as has been shown in the ORX experiment. Nevertheless, care should be taken to assure that bone segmentation errors are as small as possible such that more subtle changes can be correctly detected and quantified with statistical significance. Hence, the remaining challenge for low-dose in vivo μCT imaging of bone lies in developing more sophisticated segmentation techniques to accurately extract the relevant information from the images. One such approach that is currently under investigation to overcome the limitations of traditional μCT segmentation techniques is the combined reconstruction and segmentation of the images [28]: rather than starting the segmentation from the degraded reconstruction, these techniques directly

include the projection data in the segmentation process, allowing incorporation of the resolution properties of the scanner system and leading to more accurate segmentations.

Bearing this limitation on bone segmentation accuracy in mind, we are convinced that the image quality obtained with the proposed 9 μm pixel size in vivo μCT imaging protocol suffices for longitudinal follow-up of both trabecular and cortical bone mass and structure in mice, as demonstrated by the ORX experiment. This protocol can be applied to any experiment in which the trabecular structure of murine bone needs to be evaluated. Extracting accurate quantitative information on trabecular parameters from images acquired with the proposed 18 μm pixel size in vivo μCT imaging protocol is less likely. Yet, the 18 μm pixel size protocol has its merit in its much lower radiation dose compared to the 9 μm pixel size protocol and may allow more frequent imaging. Hence, it might be more suited to monitor distinct changes in bone mass and structure such as callus formation during fracture repair or large bone lesions associated with bone metastasis progression.

3.5 Conclusion

In vivo μCT is a useful tool for the in vivo follow-up of bone mass and structure in mice. However, proper optimisation of the scan parameters and study set-up is necessary, as high radiation doses can alter bone morphological parameters. We here provide two study set-ups for the in vivo follow-up of both young and old mice over a study period of 4 weeks without significant side effects of in vivo X-ray exposure.

Chapter 4

Simultaneous reconstruction and segmentation for CT

4.1 Introduction

Quantitative information on small animal trabecular bone structures is of major interest for bone research. The information is typically gathered by acquiring μCT images of small animal models. μCT systems allow non destructive, high resolution, 3D imaging of bone structures. The quantitative measures are typically calculated from binary images, requiring segmentations of the μCT tomographic images into bone and non-bone voxels [9].

With the introduction of in vivo μCT systems, longitudinal bone studies have become possible. However, radiation side effects have to be considered in case of repeated μCT scanning of the same animal [69]. Lowering the administered dose to avoid radiation side effects results in lower image quality, as manifested by increased noise, reduced sharpness and more intensity inhomogeneity in the reconstructed images [75]. Such artifacts negatively affect the quality of the segmentation, usually obtained by thresholding the reconstruction images [9].

As the purpose of longitudinal studies is to evaluate changes in bone architecture over time, it is of importance that bone segmentation is sufficiently accurate to detect subtle differences. When image artifacts become more pronounced, the assumptions implied in conventional threshold-based segmentation techniques will hold no longer and the segmentation will yield unsatisfactory results [73]. Especially for thin structures relative

to the image resolution, such as murine trabeculae, segmentation becomes problematic. Segmentation methods have to be adapted to cope with such imaging artifacts [147].

Conventional segmentation methods are based solely on the reconstruction image, which is prone to reconstruction errors and artifacts. To obtain a segmentation method more robust to reconstruction artifacts, one could exploit the available projection data in addition to the reconstruction image. This idea has led to the development of the minimum projection distance, where global or local thresholds are determined by minimising the difference between projections of the segmentation and the measured projection data [6, 5, 134].

One could avoid reconstruction artifacts altogether by forcing a segmentation during the reconstruction process. In discrete tomography, the attenuation image consists of a small number of discrete attenuation values. Knowing the finite range of attenuation values may enable determination of the attenuation at points where without this knowledge it could not be determined [49]. One such discrete tomography algorithm is DART, in which an iteration consists of an algebraic reconstruction update of the image, a thresholding of the image into a priori given attenuation values, and updates applied only to the boundaries between tissues to limit the number of unknowns [4].

While discrete tomography explicitly demands a discrete set of attenuation values, simultaneous reconstruction and segmentation (SRS) approaches encode knowledge about the tissue attenuation into the reconstruction using the maximum a posteriori (MAP) framework. The MAP approach enables regularisation to restrict the number of attenuation values, resulting in a segmented reconstruction. Additionally, it allows the straightforward incorporation of the blurring induced by the scanning system.

The prior probability, or simply the prior, is the probability assigned to a variable before the variable is taken into account. In our framework, the prior encodes knowledge about the reconstruction image without taking this specific reconstruction image into account. For example, it is known before performing the reconstruction that a murine bone sample consists of a limited amount of tissues: bone, soft tissue and perhaps water or air. Therefore, a reconstruction image of this sample with a limited amount of grey values is more likely than a reconstruction image with a wide range of grey values. Such knowledge can be expressed mathematically in different ways, leading to different priors.

A straightforward prior consists of modelling the different tissues in the image as mixed Gaussian or gamma distributions [51, 135]. A disadvantage of such priors is that the number of tissues in the image needs to be known before reconstructing, and estimates of the mean and standard deviation of

the attenuation of the tissue classes need to be supplied. Alternatively one could limit the amount of attenuation values by enforcing some kind of edge-preserving smoothing [149]. One way to formulate this mathematically is by penalising relative attenuation differences of neighbouring voxels below an edge-indicating threshold, the relative difference prior [100].

Another approach to limit the number of attenuation values is by means of the total variation prior. This prior is related closely to the domain of compressed sensing, which showed that the image of a sparse representation can, under a set of boundary conditions, be found from random measurements as the ℓ_1-norm subject to the measurement model [15, 30]. While the attenuation image of an object is generally not sparse, its gradient magnitude is likely to be so. Compressed sensing predicts that the image can be found by minimising the ℓ_1-norm of the gradient magnitude, which is identical to the total variation formulation. Total variation has shown promising results in a variety of CT reconstruction applications [125, 132, 156, 60].

Mutual information and joint entropy priors have been applied to account for anatomical information in PET reconstruction [126, 133]. Their value lies in their ability to interpret the histogram without requiring an explicit histogram model such as the mixed distribution priors. In the SRS method proposed in this chapter, we exploit this property and present the minimal entropy prior, an adaptation of the joint entropy prior proposed in [99]. In combination with a physically supported model of the system blurring and noise, the developed algorithm yields more accurate segmentations of bone images, as evaluated by morphological bone parameters.

In this chapter we firstly review how image resolution can be quantified with the point spread function and how it affects various segmentation methods, and formulate the general iterative reconstruction framework. We then introduce the crux of our method, the resolution modelling and minimal entropy prior, and discuss implementation choices and parameter determination. A series of experiments investigates the performance of the algorithm with respect to other methods, and provides example applications. Finally, we discuss the advantages and limitations of the method and the study.

4.2 State of the art

4.2.1 Image resolution

To understand why some segmentation methods fail on low dose images, we inspect how image quality deteriorates upon reducing the dose. The same

mouse tibia was scanned with an ex vivo and an in vivo scanner at different dose levels, which are inversely related to the pixel size as is shown later. The obtained reconstructions were registered and are shown in Figure 4.1(a)-(c). The ex vivo image at 5 μm pixel size displays the sharpest edges. The sharpness decreases for the two images acquired by the in vivo scanner at respectively 9 and 18 μm. The intensity profile of a line through these images is plotted in Figure 4.1(d). It can be seen that the trabecular structures are wider in the in vivo images than in the ex vivo image, corresponding with a smoother image. Additionally, the intensity of the trabeculae is lower.

The sharpness of an image can be described by the image resolution. Resolution describes the ability to resolve small details in the image. The maximum resolution of an image is the voxel size, because structures smaller than a voxel can not be distinguished. The resolution of a reconstructed μCT image depends on properties of the system, the acquisition settings, and the reconstruction settings. Properties of the scanning system that influence the resolution are the focal spot size of the X-ray tube, the system geometry, the zoom factor, the detector element size, and the crosstalk between detector elements. System geometry refers to how precise the positions of the moving scanner components can be controlled. In general, scanners with a rotating sample offer a better resolution than those with a rotating tube and camera. The system properties are inherent to the used scanner and are manifested in the projection data, causing artifacts in the reconstructed image. Acquisition settings that influence the image resolution are the amount of acquired projection angles and the zoom factor, which is adjustable for certain scanners. Reconstruction settings such as the image voxel size and the reconstruction filter used in filtered backprojection techniques can alter the image resolution as well.

To preserve the noise characteristics of the reconstructed image intensities, the administered dose D should be proportional to the fourth power of the spatial resolution [38]

$$D \propto \frac{1}{\Delta x^4 (\sigma/\mu)^2} \tag{4.1}$$

with D the dose, Δx the voxel size which can be considered as the spatial resolution and σ/μ the coefficient of variation, a measure of noise in the image. This implies that under equal noise conditions, doubling the resolution by halving the voxel size requires 16 times more dose.

Image resolution can be quantified by the full-width-at-half-maximum (FWHM) of the system point spread function. The point spread function (PSF) can be computed by scanning a homogeneous object with crisp boundaries and reconstructing the projection data with a particular set of acquisition and

reconstruction parameters [64]. The intensity response is sampled across the boundary of the object and is plotted in Figure 4.1(e) for a cylindrical phantom. This represents the edge response function and displays how much an edge is smoothed. The ex vivo scanner deforms the edge the least, while decreasing the dose increases the smoothing. Upon differentiation of the edge response function, the PSF is obtained (Figure 4.1(f)). The PSF describes the response of a set of acquisition and reconstruction parameters to an object that is a single point. Upon scanning a single point, the reconstruction will show a smooth blob instead of a single point. The PSF can be characterised by its full-width-at-half-maximum (FWHM). A higher resolution corresponds to a lower FWHM value. The resolution of the projection images can be computed using the same approach.

4.2.2 Segmentation

The performance of segmentation methods used in bone imaging can be understood with reference to the PSF. The different methods described below are illustrated in Figure 4.2.

Global thresholding

A threshold is an intensity value that represents the grey value a voxel in the image should exceed to be considered a voxel of some tissue, in our case bone. Global thresholding applies the same threshold value to every voxel in the image. The global threshold is often determined by visually selecting an appropriate threshold, but automatic threshold selection methods exist as well.

The schematic drawing in Figure 4.2(a) shows the intensity of a simulated piece of bone, representing a thick and a thin trabecula, in the black line. A measurement of this piece of bone is blurred by an amount given by the PSF of the system setup. The acquired reconstruction image is shown in the black dashed line. For a system with a relatively small FWHM of the PSF, a global threshold can be selected that gives an accurate segmentation of the bone (Figure 4.2(b)). The threshold value at each location is shown by the grey dash-dot line.

Consider the same piece of bone being scanned by a system setup with a larger PSF (Figure 4.2(c)). Due to the point spread function, the intensity of bone is not constant throughout the image. Thin trabeculae have lower intensity values than thicker structures. The global threshold performs unsatisfactorily, as can be seen in Figure 4.2(d). If the threshold is selected to correctly segment

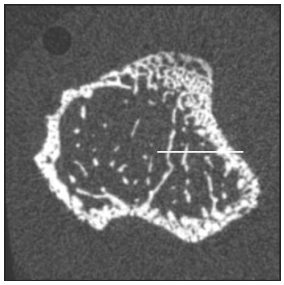

(a) 5 μm ex vivo image

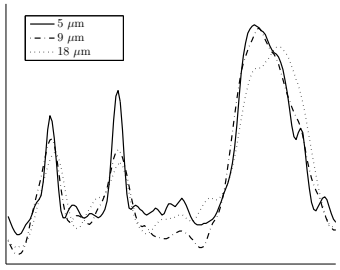

(d) Intensity profile

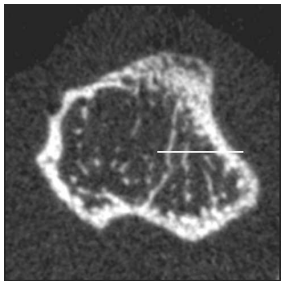

(b) 9 μm in vivo image

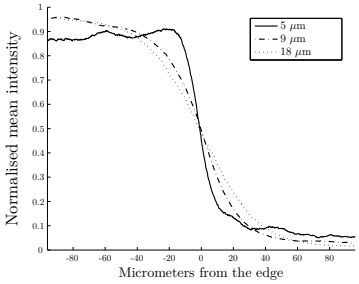

(e) Edge response function

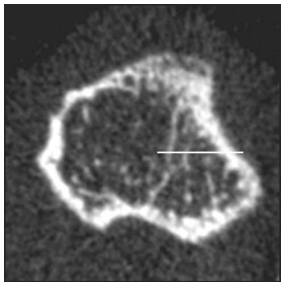

(c) 18 μm in vivo image

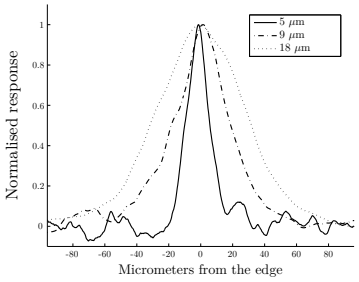

(f) Point spread function

Figure 4.1: Image Resolution (a) Mouse tibia scanned ex vivo at 5 μm pixel size. (b) The same tibia scanned in vivo at 9 μm pixel size. (c) The same tibia scanned in vivo at 18 μm pixel size. (d) Intensity profile through the white line in images (a-c) for the different acquisition settings. (e) Edge Response Function for the different acquisition settings obtained from a cylindrical phantom. (f) Point Spread Function for the different acquisition settings obtained from a cylindrical phantom.

the thick structures, the thin ones will disappear. If the threshold is lowered to segment thinner structures, the thicker ones are overestimated. As a result, global thresholding only performs well when the PSF is small with respect to the thickness of the structures.

Local thresholding

As a single threshold is inappropriate for low quality images, local or adaptive thresholding defines a different threshold in every voxel [73]. The threshold can be adapted in every voxel to correct for the intensity of bone in the neighbourhood of a voxel. There are various ways to determine the local threshold. We use the adaptive thresholding available in CTAn, the μCT software package provided by SkyScan (Kontich, Belgium). In this implementation, the local threshold is calculated as the average of the minimum and maximum values within a spherical region of a certain radius around each voxel. The approach implicitly assumes that each sphere contains bone as well as soft tissue, and sets the threshold in the middle of the intensities corresponding to those two tissues. To compensate for regions that contain no bone or only bone, a range of intensity values can be specified outside of which voxels are excluded from local thresholding. To obtain more robustness to noise, the threshold can also be selected as the mean within the spherical region.

Figure 4.2(e) illustrates the principle of local thresholding. While it performs better than global thresholding, it can be seen that the thickness of the thin trabecula is overestimated.

Waarsing thresholding

Waarsing et al. presented an improved segmentation method that starts similar to local thresholding, but then heuristically increases the local threshold for thinner structures [147]. The method first smooths the image with a Gaussian kernel, to prevent the detection of false edges in the noisy background. Then Sobel operators are used to obtain an edge magnitude image. Edges with magnitude larger than a cut-off value are retained, and connected edges with magnitude larger than a second cut-off value as well. These cut-off values are to be selected as low as possible, including as many edges as possible while avoiding edges associated with noise. At edge voxels, the local threshold is defined as the attenuation values in the image at those voxels. To obtain threshold values in non-edge voxels, the local thresholds are dilated over the entire image, resulting in a local threshold value in each voxel.

	Method	1D scheme	2D illustration
(a)	An ex vivo image has a small FWHM of the PSF.	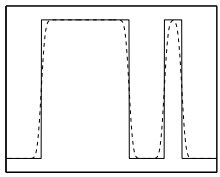	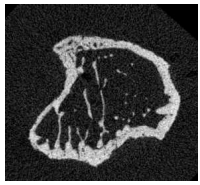
(b)	Global thresholding works well on an ex vivo image.	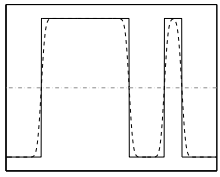	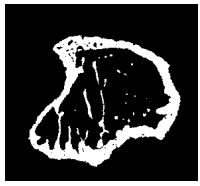
(c)	An in vivo image has a larger FWHM of the PSF.	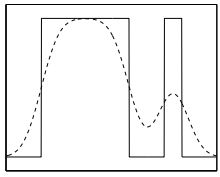	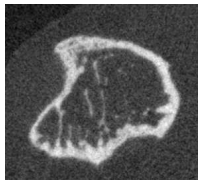
(d)	Global thresholding misses trabeculae on an in vivo image.	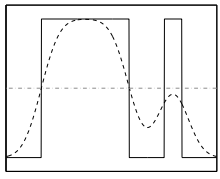	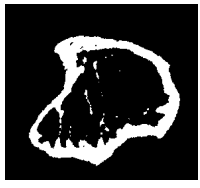
(e)	Local thresholding adjusts the threshold in every voxel but overestimates thin structures.	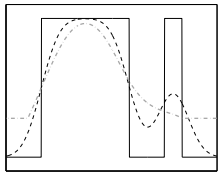	
(f)	Waarsing segmentation [147] heuristically adjusts the local threshold for thin trabeculae.	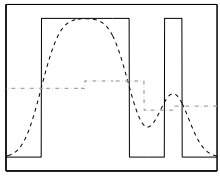	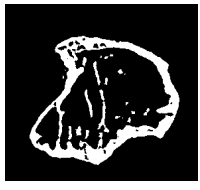

Figure 4.2: Schematic illustration of segmentation methods. The black line is the intensity of the bone object, resembling a thick and a thin trabecula. The black dashed line shows the acquired bone image, obtained by convolving the object with the PSF. The grey dash-dot line shows the threshold in each voxel above which the voxel is regarded as bone.

By assuming that all trabeculae have a similar bone mineral density, voxels that contain thin trabeculae will have below average local thresholds due to the PSF. The threshold T_L of voxels containing thin trabeculae, defined as voxels having a local threshold one standard deviation below the average local threshold, is scaled upwards to obtain an adjusted local threshold $T_{L,adj}$:

$$T_{L,adj} = T_L \left(1 + \frac{T_{L,mean} - T_L}{T_{L,mean} - CT_{BG}}\right) \tag{4.2}$$

$T_{L,mean}$ is the average local threshold over all voxels prior to adjusting the thresholds, and CT_{BG} is a parameter that represents the CT value of the background [147]. In figure 4.2(f) it is seen that Waarsing's adaptation improves the segmentation of thin trabeculae.

4.2.3 Iterative reconstruction

CT reconstruction is the process of computing the 3-dimensional density function from a set of 2-dimensional projections. Projection data obtained from cone-beam scans are generally reconstructed using a weighted filtered backprojection algorithm [35]. The method is fast, and provides accurate results under certain assumptions. However, when the assumptions are not met, artifacts are generated in the reconstruction image, due to the incongruence between model and reality. To allow detailed modelling of the actual physical process, we resort to iterative reconstruction.

Generally, iterative reconstruction techniques define an objective function that relates the reconstruction image to the projection measurements. An optimisation strategy is then required to find the reconstruction image as the maximum of the objective function.

Objective function

The purpose of the reconstruction is to find the attenuation image $\mu = [\mu_1 \mu_2 \dots \mu_J]$ in every voxel $j = [1, 2, \dots, J]$ that best corresponds to the measured projection data $y = [y_1 y_2 \dots y_I]$ at each projection angle and detector element $i = [1, 2, \dots, I]$. Usually, that "best" correspondence is formulated in a statistical framework as the most probable attenuation image given the

measurement [74]:

$$\mu = \arg\max_{\mu} P(\mu|y) \tag{4.3}$$

$$= \arg\max_{\mu} P(y|\mu)P(\mu) \tag{4.4}$$

$$= \arg\max_{\mu} \ln P(y|\mu) + \ln P(\mu) \tag{4.5}$$

where we applied Bayes' theorem, omitted the probability of the measurement $P(y)$ as it is constant and used the monotonicity of the logarithmic function.

The term $P(y|\mu)$ is called the likelihood of the reconstruction image, and $\ln P(y|\mu)$ is referred to as the loglikelihood $L(\mu)$. The likelihood term makes sure that the reconstruction image fits the projection data. $P(\mu)$ is the prior image information, claiming that some reconstructions (e.g. those with less noise) are more probable than others. If no a priori information is known, the prior can be dropped and Equation 4.5 becomes the maximum likelihood (ML) approach. With prior information, the problem is called the maximum a posteriori (MAP) approach.

The different components of the objective function are now discussed in detail, similar to the outline given in [22].

Forward model The forward model describes the physical measurement by defining the relationship between the attenuation μ and expected measurement values $\bar{y}$. The expected value of the photon counts in each detector pixel is conventionally computed using [74]

$$\bar{y_i} = b_i e^{-\sum_j l_{ij}\mu_j} \tag{4.6}$$

which is a discretised version of the law of Beer-Lambert. b_i represents the number of photon counts in the blank projection ray i, l_{ij} the intersection length of projection line i with voxel j, and μ_j the reconstructed attenuation value in voxel j.

The argument of the exponent is computed by a projection:

$$p_i = \sum_j l_{ij}\mu_j \tag{4.7}$$

For each detector pixel, the projection p can be written in matrix form as

$$p = A\mu \tag{4.8}$$

The matrix A (with $A(i,j) = l_{ij}$) is called the projection matrix and maps the reconstruction image into the projection domain. The opposite operation, mapping the projection into the reconstruction domain, is called backprojection. The assumptions and approximations in the implementation of projector and backprojector may differ. When the assumptions and approximations are the same and the backprojection operator is exactly the transpose of the projection matrix, we speak of a matched projector-backprojector pair.

The dimensions of the sparse matrix A are given by the number of measurements and the number of reconstruction voxels. For a typical μCT reconstruction on a grid of $800 \times 800 \times 800$ voxels from 360 projections captured with a 4000×2000 pixel detector, A consists of roughly $10^9 \times 10^9$ elements. Due to its tremendous size, the matrix cannot be stored in memory during reconstruction and is typically recomputed whenever required. The projection and backprojection calculations are the most computationally expensive steps in the iterative reconstruction approach.

The forward model is very flexible and can be refined to model the physical reality as accurately as desired. For instance, one could model the finite beam width of the X-ray beam, the multi-energetic nature of the X-ray beam, the detector cross talk, or anything else deemed relevant.

Noise model When several projections of the same object with the same X-ray settings and the same detector are measured, the detected amount of photons in a detector pixel varies. This unwanted noise is present in any real world measurement and originates in statistical quantum effects. Modeling the noise assures that relatively more weight will be given to reliable measurements, and less weight will be given to noisy measurements [22].

The noise in energy integrating detectors approximately follows a compound Poisson distribution [151], but can be approximated by a Poisson distribution if enough counts are detected [32]. The probability of measuring y_i photons in detector pixel i when the expected value is $\bar{y_i}$ (Equation 4.6), is given by the Poisson noise model as

$$P(y_i|\bar{y_i}) = \frac{\bar{y_i}^{y_i}}{y_i!} e^{-\bar{y_i}} \tag{4.9}$$

The loglikelihood can now be computed as

$$\begin{aligned} L(\mu) &= \ln P(y|\mu) && (4.10)\\ &= \ln P(y|\bar{y}) && (4.11)\\ &= \ln\left(\prod_i P(y_i|\bar{y_i})\right) && (4.12)\\ &= \sum_i y_i \ln(\bar{y_i}) - \bar{y_i} - \ln(y_i!) && (4.13) \end{aligned}$$

noting that measuring y_i depends only on the expected value $\bar{y_i}$, that the statistical variations on the measurements y_i are mutually independent [24], and that the constant $\ln(y_i!)$ can be omitted for maximisation purposes.

Lange and Carson have shown that, for the forward model of Equation 4.6 combined with a Poisson noise model, the loglikelihood is concave if the projection matrix has at least as many measurements as voxels and is of full rank [74]. A concave function is easier to optimise because it has a single maximum.

Prior model The prior describes information about attenuation values or neighbouring voxel relations in the reconstruction image. Knowledge about neighbouring attenuation values is generally incorporated in the form of the Gibbs prior

$$P(\mu) = \prod_j \prod_k e^{-\beta\,\phi(\mu_j,\mu_k)} \tag{4.14}$$

with β a parameter to control the weight of the prior and ϕ a function that penalises certain attenuation differences. Typically ϕ is constructed to penalise small differences to obtain smoothing, yet to allow larger differences to tolerate edges in the image. Taking the logarithm gives

$$\ln P(\mu) = -\beta \sum_j \sum_k \phi(\mu_j, \mu_k) \tag{4.15}$$

For example, a prior penalising relative differences was suggested by Nuyts et al. [100]

$$\phi(\mu_j, \mu_k) = n_{jk} \frac{(\mu_j - \mu_k)^2}{(\mu_j + \mu_k) + \gamma|\mu_j - \mu_k|} \tag{4.16}$$

with $n_{jk} = n_{kj}$ the weights assigned to neighbouring voxels. Typically $n_{jk} = 1$ for direct neighbours and $n_{jk} = 0$ for other voxels. If the prior is concave, it doesn't introduce any local maxima in the objective function. This makes the optimisation strategy less dependent on initialisation or acceleration techniques [100].

Optimisation strategy

Now that the objective function can be computed, an optimisation strategy that finds the $\arg\max_\mu$ is required. A plausible approach would be the expectation maximisation method, but this leads to a transcendental equation that can not be solved exactly [74]. A myriad of alternate optimisation strategies have been developed, but we will focus on a gradient ascent algorithm proposed by Nuyts et al. [101].

The likelihood can be approximated in the neighbourhood of the current reconstruction μ^n by a quadratic function obtained from a truncated Taylor series expansion. A surrogate function that separates the dependency of a voxel on all other voxels is formulated for the quadratic function. The maximum of this surrogate function can be found by gradient ascent, which results in the following update step provided that the likelihood is concave [101, 24, 141]

$$\mu_j = \mu_j^n + \Delta\mu_j \tag{4.17}$$

$$= \mu_j^n - \frac{\frac{\partial L}{\partial \mu_j}}{\sum_h \frac{\partial^2 L}{\partial \mu_j \partial \mu_h}} \tag{4.18}$$

where μ_j and μ_j^n are the new and current reconstructed attenuation values in pixel j and h represents another voxel. This optimisation approach has been named Maximum Likelihood for TRansmission (MLTR). For the forward model and noise model described above, this becomes

$$\Delta\mu_j = -\frac{\sum_i l_{ij}(\bar{y_i} - y_i)}{-\sum_i l_{ij}\bar{y_i} \sum_h l_{ih}} \tag{4.19}$$

The computation of for example $\sum_i l_{ij}(\bar{y}_i - y_i)$ in the denominator corresponds to a backprojection of $(\bar{y}_i - y_i)$. In the case of a prior, we use the implementation of [102]. Defining the logarithm of the prior as N, this leads to the update step:

$$\Delta\mu_j = \left(\frac{\partial L}{\partial \mu_j} + \frac{\partial N}{\partial \mu_j}\right) / \left(\frac{\sum_i l_{ij}}{\mu_j^n} + 2\sum_k n_{jk}\frac{\partial^2 N}{\partial \mu_j^2}\right) \tag{4.20}$$

All partial derivatives are evaluated in the current reconstruction. This optimisation approach has been named Maximum A Posteriori for TRansmission (MAPTR). This is a combination of the gradient ascent method above, with Newton's method. The prior is added to the denominator to be more stable when the prior is large.

4.3 Simultaneous reconstruction and segmentation

4.3.1 Theory

A fundamental feature for correct segmentation of low resolution images is the incorporation of the point spread function into the segmentation process. However, this blurring manifests itself as an artifact in the image, and could be much easier incorporated in the reconstruction algorithm as it actually influences the projections. The quality of the segmentation could be verified by comparing it to the projection data. We pursue a simultaneous reconstruction and segmentation strategy, in which error propagation is prevented by evaluating the segmentation continuously with respect to the projection data. An additional advantage over methods that segment the reconstruction image is that the noise can modelled accurately, which is expected to have a positive impact on the segmentation quality.

Resolution modelling

At this point we can incorporate the PSF of the system in our model. The system properties affect the amount of blurring present in the projections. If the calculated projections are smoothed with a kernel of the same size as the PSF of the scanner, the effect of the PSF is incorporated and the reconstruction estimate is expected to be sharper. Therefore we will model the blurring with a convolution kernel w_{in}.

The main contribution to the scanner PSF comes from detector smoothing, that is associated with the light transport in the scintillator [122]. As it is

the photons that cause the blur, the smoothing should be modelled outside of the exponential. Instead of using Equation 4.6, we will use the following definitions:

$$\bar{y_i} = \sum_n w_{in}\bar{\psi_n} \qquad \text{with } \sum_n w_{in} = 1 \text{ and } w_{in} = w_{ni} \tag{4.21}$$

$$\bar{\psi_i} = b_i e^{-\sum_j l_{ij}\mu_j} \tag{4.22}$$

The smoothing is implemented by a Gaussian kernel whose size is a parameter in the reconstruction process, dependent on the used μCT system. It has been argued that the PSF varies spatially throughout the projection [154, 124], but we assume a constant PSF.

The derivatives of the likelihood become

$$\frac{\partial L}{\partial \mu_j} = \sum_i l_{ij}\bar{\psi_i}\sum_n w_{in}\frac{\bar{y_n} - y_n}{\bar{y_n}} \tag{4.23}$$

$$\sum_h \frac{\partial^2 L}{\partial \mu_j \partial \mu_h} = -\sum_i l_{ij}\bar{\psi_i}\sum_h l_{ih} \tag{4.24}$$

where we assumed that $\sum_h l_{ih}$ is very smooth and not modified by the blurring with the kernel w_{in}.

As a result, the update step of Equation 4.18 becomes

$$\Delta\mu_j = -\frac{\frac{\partial L}{\partial \mu_j}}{\sum_h \frac{\partial^2 L}{\partial \mu_j \partial \mu_h}} \tag{4.25}$$

$$= -\frac{\sum_i l_{ij}\bar{\psi_i}\sum_n w_{in}\frac{\bar{y_n} - y_n}{\bar{y_n}}}{-\sum_i l_{ij}\bar{\psi_i}\sum_h l_{ih}} \tag{4.26}$$

Note that this resolution model does not account for movement artifacts or misalignment. The projections are expected to be free from sample movement and are corrected for misalignment before the reconstruction starts.

Minimal entropy prior

The statistical model also allows incorporation of prior information about the object to be reconstructed. In our bone application, we know that the image

consists of a limited number of tissues: usually bone, soft tissue and air. When for a certain voxel the projection data is indecisive for an attenuation value, the prior information can nudge the voxel towards the most likely attenuation value.

The prior can be implemented as the minimal entropy prior that needs no image specific input, such as how many tissues are present in the object. Entropy is a measure of uncertainty, in this case of the uncertainty regarding the intensity of a pixel in the image. An image with high entropy contains many different grey values, while an image with low entropy consists of limited intensities. Minimising the entropy will reduce the amount of intensities, and hence tissues, in the image.

Computation of the entropy requires sorting the intensities into bins in order to evaluate intensity distributions over the bins. For A bins, the minimal entropy prior is defined as [28]

$$M_{ME} = \ln P(\mu) = -\beta \sum_{a=1}^{A} p_\mu(a) \ln p_\mu(a) \tag{4.27}$$

with $p_\mu(a)$ the normalised histogram, i.e. the probability of image intensity bin a in μ. To ensure differentiability, p_μ is calculated using a Parzen window estimator

$$p_\mu(a) = \frac{\sum_j p_{\mu_j}(a)}{\sum_a \sum_j p_{\mu_j}(a)}, \text{with} \tag{4.28}$$

$$p_{\mu_j}(a) = \frac{1}{\sqrt{2\pi}\sigma} e^{\frac{-(\mu_j - a)^2}{2\sigma^2}} \tag{4.29}$$

σ is the standard deviation of the Gaussian of the Parzen window. Increasing the value of σ leads to a lower number of independent bins, and has a similar effect as decreasing A. Therefore, we fix $\sigma = 1$ and only adjust the amount of bins A.

The gradient of the minimal entropy prior is given by

$$\frac{\partial M_{ME}}{\partial \mu_j} = -\sum_a (1 + \ln p_\mu(a)) p_{\mu_j}(a) \frac{a - \mu_j}{\sigma^2} \tag{4.30}$$

As in [99] we approximate the second derivative heuristically to

$$\frac{\partial^2 M_{ME}}{\partial \mu_j^2} \approx \sum_a \frac{\ln p_\mu(a) p_{\mu_j}(a)}{\sigma^2}. \tag{4.31}$$

The minimal entropy prior is not concave and introduces local maxima. To avoid undesired local minima, we increase the strength of the prior gradually during iterations [99].

The minimal entropy prior is illustrated in Figure 4.3. An artificial image containing two tissues and some noise was generated and shown in Figure 4.3(a). The two intensities and the noise can also be seen in the normalised histogram, where the relative percentage of pixels within a certain bin is plotted (Figure 4.3(b)). After 80 iterations of minimising the entropy of the image, it looks like Figure 4.3(c). As can be seen in the histogram (Figure 4.3(d)), the noise is removed and only the tissue intensities remain, resulting in a segmentation. The histogram has become more peaked, or it has less entropy than in Figure 4.3(b). The opposite effect, maximising the entropy, is illustrated in Figure 4.3(e)-(f). The histogram is now spread out much more, indicating that there is more uncertainty regarding the intensity of a pixel in the image.

The prior restricts the amount of attenuation values in the reconstruction, resulting in a nearly segmented image. Otsu's method is applied to the reconstructed image to automatically obtain a binary segmentation of the bone [104].

Computational complexity

In an FDK reconstruction, each measurement sample is backprojected a single time, after weighting and filtering. In MLTR, one projection and two backprojections are required per iteration, and we use 20 iterations, making it a much more computationally expensive technique.

Additionally, the image intensities need to be distributed over a histogram. The computation time of the first and second derivatives of the minimal entropy prior takes 10 times longer than those of the mixed distribution prior (a Gaussian mixture model) with the current serial implementation. Every pixel needs to be distributed over the histogram by the Parzen window, requiring multiple times the computation power per pixel compared to the mixed distribution prior. This results in a total reconstruction time that is twice as long for the minimal entropy prior compared to the mixed distribution prior.

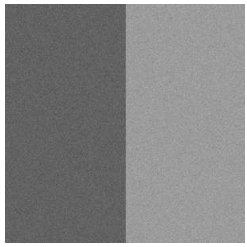

(a) Noisy image

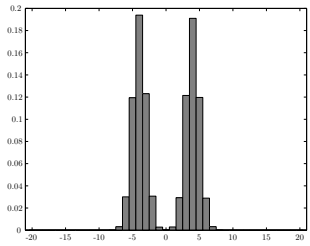

(b) Histogram of (a)

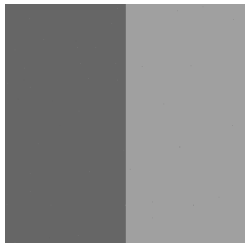

(c) Minimised entropy

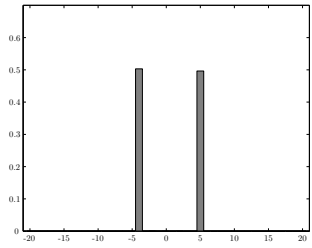

(d) Histogram of (c)

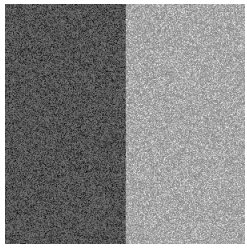

(e) Maximised entropy

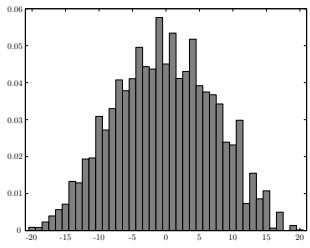

(f) Histogram of (e)

Figure 4.3: Illustration of the minimal entropy prior on an artificial example. (a) and (b) The original noisy image containing two tissues and its normalized histogram. (c) and (d) The image and its normalised histogram after 80 iterations of minimising the entropy. The histogram is more peaked than (b), removing noise. (e) and (f) The image and its normalised histogram after 80 iterations of maximising the entropy. The histogram is more uniform than (b).

4.3.2 Implementation choices

The algorithm is implemented in IDL (Exelis VIS, USA). In order to avoid local minima in the objective function and to obtain a proper reconstruction within reasonable time, certain implementation choices have been made.

Ordered subsets

In a standard iteration of the algorithm, all the projection images are used at once to calculate the update step. Instead of using all the projection data, one could limit the amount of projections used. Ordered subsets group projection data into an ordered sequence of subsets, and uses only the subset to compute the update step [56]. If each subset contains equal information about image attenuation, the convergence increase of a single subset update is similar to the convergence increase of a standard iteration. Balanced subsets are selected in practice by being mutually as different as possible, and having equally spaced projections within a subset. An iteration of an ordered subset scheme is a single pass through all the subsets. An ordered subset iteration has a similar computation time to one standard iteration [56]. As a result, the achieved speed-up is proportional to the number of subsets. All iterative reconstructions in this text use 3 projections per subset, obtaining 66 to 82 subsets, depending on the amount of projections in the dataset.

Focus reconstruction

As the trabecular structures are located in a limited region of the bone, it is generally not required to reconstruct and segment the entire scanned object at high resolution. A rough reconstruction of the entire object can be generated quickly with FDK at large pixel size. In this reconstruction a focus region can be selected on which the SRS approach can be unleashed at small pixel sizes for high resolution. This leads to drastic improvements in reconstruction time.

Projector

Most of the computation time is spent executing the projector and backprojector. For this reason they are implemented in the programming language C, which allows faster computation. Nevertheless, with this implementation 80% of the computation time of an ML reconstruction is spent projecting and backprojecting, according to our timing measurements. A distance driven projector is used [25].

The projector should model the imaging geometry and physics as accurately as possible. It has been shown that using a computationally less expensive back-projector not only reduces computation time but also speeds up convergence, at the cost of possibly having more noise [157]. Such a projector-backprojector pair is no longer matched. We use a mismatched pair that does not apply the resolution modelling in the backprojection. w_{in} is applied during the projection to compute $\bar{y_i}$ according to Equation 4.21, but the smoothing is omitted during the backprojection in the numerator of Equation 4.26.

MAPTR step size

An additional speedup can be obtained in the MAP update equation (4.20). The numerator can be seen as the step size. Taking the sum of the two turns out to be rather conservative. To speed up convergence, we take the maximum of the two.

$$\Delta\mu_j = \frac{\frac{\partial L}{\partial \mu_j} + \frac{\partial N}{\partial \mu_j}}{\max\left(\frac{\sum_i l_{ij}}{\mu_j^n}, \frac{\partial^2 N}{\partial \mu_j^2}\right)} \tag{4.32}$$

Minimal entropy apodisation window

To ensure differentiability of the minimal entropy prior, an apodisation function distributes the value of a single voxel over multiple bins. Initially we used a Parzen window as apodisation function, but its derivative includes the Parzen window again, requiring two windowing operations. We replaced the Parzen window with a Connes window estimator, which is similar to a Parzen window but the derivatives can be computed nearly twice as fast. Equation 4.29 is then computed as

$$p_{\mu_j}(a) \quad = \quad \frac{15}{16c}\left(1 - \frac{(\mu_j - a)^2}{c^2}\right)^2 \tag{4.33}$$

with c a cut-off value.

4.3.3 Parameter selection

While physical modelling generally translates to realistic and intuitive assumptions, it is a cursed blessing with its introduction of parameters that require

careful tuning for proper functioning of the method. In this section, we detail the selection of the parameters of the proposed method.

Resolution modeling

The resolution of reconstructed images from both ex vivo and in vivo acquisitions was measured as detailed before. The PSF of images scanned ex vivo at 5 μm pixel size, in vivo at 9 μm pixel size and in vivo at 18 μm pixel size is shown in Figure 4.1(f). The corresponding FWHM values are 16 μm, 36 μm and 57 μm, respectively.

The PSF is modeled during the projection, and should therefore be measured in the projections themselves. This, however, turned out to be rather tricky without dedicated tools. The sharp edge measurement approach used to measure the PSF in the reconstruction could be used, but requires the edge to be perfectly aligned with the X-ray beam, in practice achieved using laser beams [118]. A line spread function could be measured directly by placing a thin wire on the detector [88], but the detector of our SkyScan 1076 in vivo scanner cannot be reached. A wire placed farther away from the detector is magnified and no longer yields a representative line spread function. Using this technique, Marxen et al. obtain a value of 80 μm for the FWHM of an ex vivo system similar to ours, but with 35 μm detector pixel size [88].

As obtaining FWHM measurements in the projections turns out to be impractical, we resort to theoretical derivations. The projection blur can be computed from the PSF of the reconstruction by multiplying it with the zoom factor [88], which is fixed at 1.3636 for our in vivo scanner. This results in values of 49 and 77 μm for the two imaging protocols.

As a validation of these values, projections of a mouse tibia were collected with the in vivo scanner and settings of interest as well as higher resolution ex vivo projections. As generally 2D projections of a 3D object can not be registered, both datasets were reconstructed and the high resolution image was registered and intensity scaled to match the in vivo reconstruction. The high resolution reconstruction was then projected using the in vivo projector to obtain an artificial high resolution projection. This projection was blurred with Gaussian PSFs of varying standard deviations, representing the resolution modelling. The PSF that provided the best least squares match between blurred high resolution projection and target projection was considered to be the system PSF. A similar procedure has been suggested by Sharma et al., albeit without the reconstruction step [124].

The same PSF least squares fitting procedure could be applied to the

reconstructed in vivo and ex vivo images instead of the projections. For the 9 μm pixel size protocol, this approach in the reconstruction image resulted in a FWHM of 48 μm, and a FWHM of 108 μm in the projection domain. These values are both larger than the expected values of 36 μm in the reconstruction, and the 49 μm in the projection. The larger deviation from the expected value in the projection measurement compared to the reconstruction measurement might be attributed to the difficulty of discerning fine details as the attenuation of trabecular structures is superposed on the attenuation of the thick cortex. Additionally, scatter might introduce an increased background, which could lead to an overestimation of the blurring.

By deriving the PSF from projection data, we are disregarding possible smoothing effects induced by other contributions, such as wobbling of the source position, which can smooth the image but is not visible in the projection. In this sense a PSF derived from a reconstruction image can be considered as a measure of the "effective" resolution. Combined with the indications that projection measurement of the PSF might be less accurate, we will therefore select the FWHM measured in the reconstruction image.

As it seems safer to correct for too little resolution modelling than for too much, we will use the lowest FWHM values obtained in the reconstruction, corrected with the zoom factor. The FWHM of the gaussian kernel was set to 50 μm for the 9 μm protocol and to 80 μm for the 18 μm protocol. Figure 4.4 shows a profile of a reconstruction, illustrating the generally higher and narrower bone peaks thanks to the resolution modelling.

Iteration scheme

As initialisation for μ, either a uniform image or an FDK reconstruction is common. We opt to initialise with a uniform image, as tests indicated that the resolution modelling converges faster from an empty image than adjusting an FDK image.

Maximum likelihood iterative reconstruction methods are known to produce images that become unacceptably noisy [37]. The final reconstruction can be smoothed to remove this artificial feel. Alternatively, the iteration scheme can be stopped before convergence, as the high frequency noise converges slowly. For a conventional MLTR reconstruction without resolution modelling, 3 to 5 iterations of 60 subsets provide a reasonable reconstruction without excess noise modelling. Reconstruction with resolution modelling converges slower, requiring increasing iterations for increasing FWHM values. Figure 4.5 shows the convergence properties of an image with and without resolution modelling.

(a) 5 μm ex vivo image

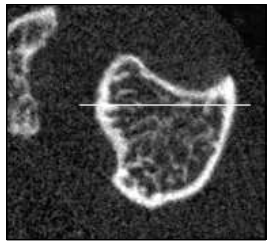

(b) FWHM = 0 μm

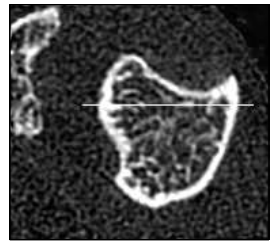

(c) FWHM = 80 μm

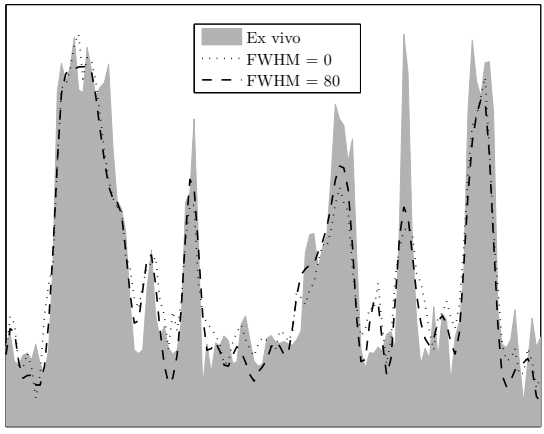

(d) Intensity profile

Figure 4.4: Effect of resolution modelling. (a) Mouse tibia scanned ex vivo at 5 μm pixel size. (b) MLTR reconstruction without resolution modelling (FWHM=0 μm) of 18 μm pixel size in vivo projections. (c) MLTR reconstruction with resolution modelling (FWHM=80 μm) of 18 μm pixel size in vivo projections. (d) Intensity profile through the white line in images (a)-(c). The resolution modelling results in generally higher and narrower bone peaks.

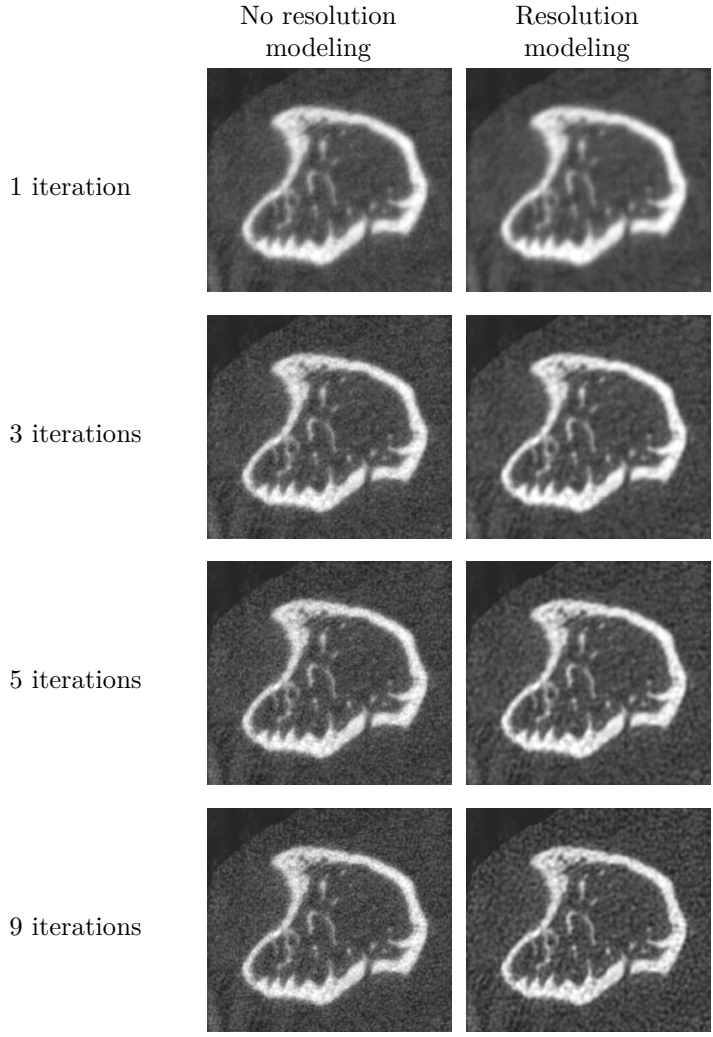

Figure 4.5: 1, 3, 5 and 9 iterations of a reconstruction with and without resolution modelling. Note that the resolution modelling requires more iterations to obtain a sharp image.

The prior evaluates intensity information in the reconstructed image. It only makes sense to evaluate the intensity distributions when they represent the object, i.e. when enough iterations have been performed. As the prior introduces local maxima and the expected optimum lies close to the ML solution, the prior is enforced after 10 iterations of resolution modelling.

To further avoid local maxima, the influence of the prior is increased gradually. The strength of the prior, β, is increased each iteration by 5%. As a compromise between a slow increase in prior strength and long computation time with many iterations, the number of iterations with the prior is set to 15, resulting in a total of 25 iterations. This results in a final prior strength of $1.05^{15}\beta_0 \approx 2.08\beta_0$, with β_0 the prior strength at initialisation.

Prior

All priors have a parameter β_0 that initialises their strength in the MAP framework. The minimal entropy prior has one additional parameter: the amount of bins A. The relative difference prior has an additional parameter γ, indicating which intensity differences are considered edges.

These parameters are determined empirically. A range of values was tested on a few bone samples and values were found to be consistent across samples. The effect of an example set of parameters for the minimal entropy prior is shown in Figure 4.6. For this dataset, the central image was perceived to provide best results.

Obviously the prior strength depends on a certain iteration scheme. If one iterates 20 or 40 iterations with a prior, and the prior strength is increased at every iteration, different values will need to be selected.

4.4 Experimental setup

A series of experiments is conducted to evaluate the proposed algorithm and to compare it to other segmentation methods. The setup of the experiments is detailed in the following section.

4.4.1 Animals and μCT acquisition

We test the segmentation method on μCT images of mouse bones acquired during two experiments with the μCT protocols proposed in Chapter 3. For

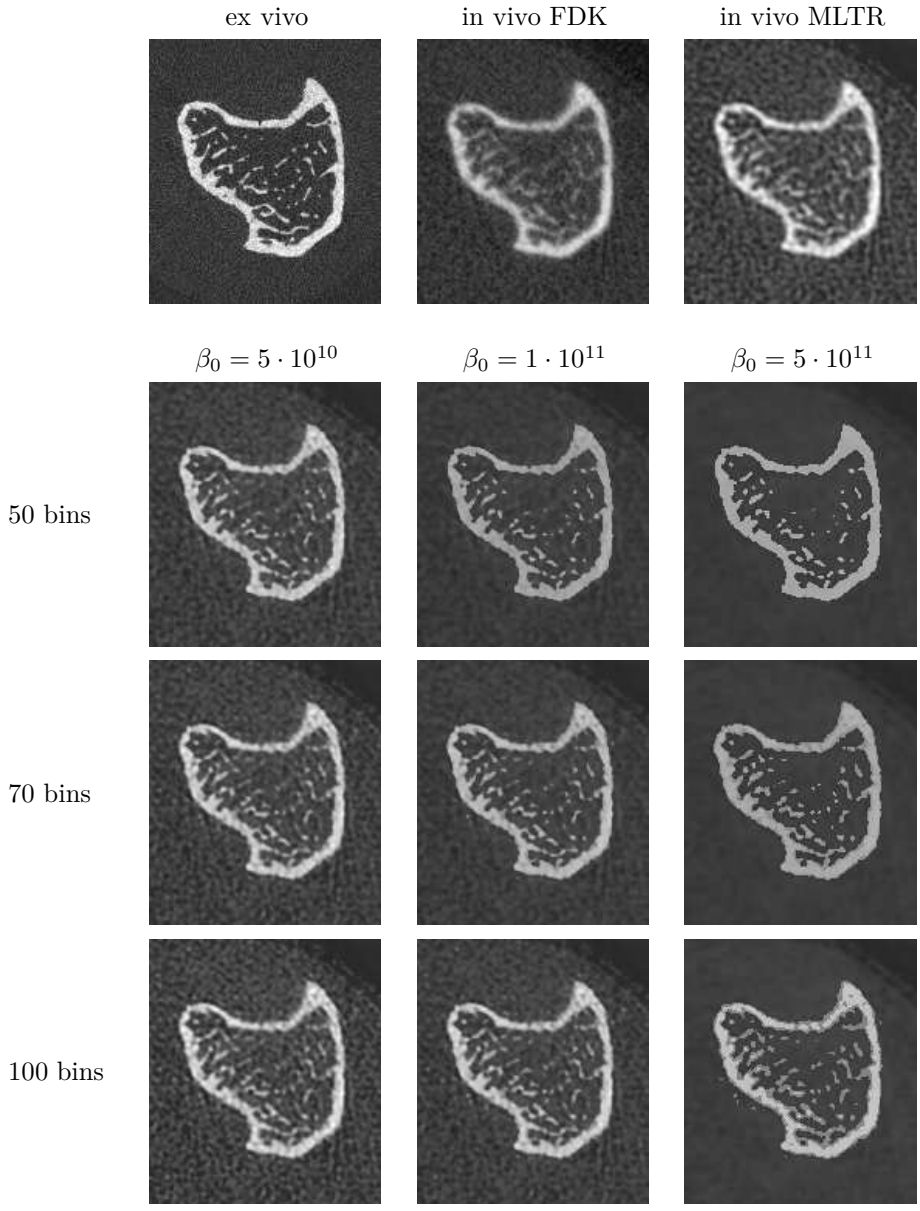

Figure 4.6: Illustration of the 2 parameters involved in the minimal entropy prior selection for a slice of a tibia scanned with the 18 μm protocol.

simplicity, we will refer to the datasets by the protocol they were acquired with.

An ovariectomy (OVX) dataset was obtained on a group of 8 female C57Bl/6 mice, 10 weeks old at the onset of the study. 4 animals received OVX treatment, resulting in reduced bone volume, while the 4 other mice received the sham operation, resulting in normal bone parameters. The left hindlimb of these mice was scanned in vivo at 3 consecutive time points, separated each time by a 2-week interval. The scan was performed with the SkyScan 1076 μCT system, utilising the 9 μm pixel size protocol (50 kV, 100 μA, 1 mm Al filter, angular rotation step 1°, 199 projections, exposure time 3.3 s, scan duration 12 min).

In a follow-up dataset, the left tibia of male mice of 4 and 16 weeks old at the onset of the study, were imaged in vivo 3 times over a period of 4 weeks. They were subjected to the 18 μm pixel size protocol (50 kV, 100 μA, 1 mm Al filter, angular rotation step 0.8°, 248 projections, exposure time 1 s, scan duration 5 min).

After the last in vivo scan, mice of both experiments were sacrificed and dissected tibiae were imaged ex vivo with the SkyScan 1172 μCT system after overnight fixation in 2% paraformaldehyde. Typical ex vivo acquisition settings were 5 μm pixel size, 50 kV, 200 μA, 321 projections, exposure time 590 ms and a filter of 0.5 mm Al. These high resolution ex vivo images are considered to provide a ground truth for in vivo images acquired at the last time point.

To investigate the influence of dose on quantification parameters, a single excised tibia was scanned with the in vivo scanner and the 9 μm protocol, but with an angular rotation step 0.2°, resulting in 986 projections. The availability of the additional projection images allows a finer selection of a set of projections to generate the reconstruction from. This tibia was also scanned ex vivo with the typical settings to provide a reference image.

4.4.2 Reconstruction and segmentation

The in vivo images were reconstructed using the FDK reconstruction algorithm and segmented with global, local and Waarsing thresholding. To remove user influence, the global threshold was selected using Otsu's method, an automatic method that minimises the intra-class variance within the two modes [104]. The local thresholding method used a radius parameter of 100 μm and the background threshold value was determined manually but kept the same within a dataset. The Waarsing thresholding used a Gaussian smoothing with a standard deviation of 20μm and the edge cutoff parameters were determined empirically by trial and error and kept constant within a dataset.

The in vivo images were also reconstructed using the proposed SRS approach. Unless otherwise indicated, images acquired with the 9 and 18 μm pixel size protocols were reconstructed with FWHM values of 50 μm and 80 μm respectively, and to voxelsizes of 10 μm and 20 μm respectively. The iteration scheme consists of 10 MLTR iterations succeeded by 15 MAPTR iterations combined with the indicated prior. The minimal entropy prior parameters were set to $\beta_0 = 1 \cdot 10^{12}$ and $A = 200$ for 9 μm protocol images, and to $\beta_0 = 1 \cdot 10^{11}$ and $A = 70$ for 18 μm protocol images. The relative difference prior parameters were set to $\beta_0 = 1 \cdot 10^3$ and $\gamma = 30$ for both imaging protocols. These values were obtained as explained in the parameter selection section. For the combined prior, the weights of both priors were halved.

The ex vivo images were reconstructed using an FDK algorithm provided by the μCT manufacturer (NRecon, SkyScan) at 5 μm voxelsize. Ex vivo images were aligned to the FDK-reconstructed in vivo images with an affine transformation using registration software based on mutual information [86]. The resampled ex vivo image was segmented using Otsu's method.

For the dose reduction experiment, the same procedures were followed, but the amount of projections used in the reconstruction is varied. The dose administered with the 9 μm pixel size protocol is simulated by using one in five projections. Further subsampling of the number of angular views allows virtual reduction of the dose. Each of the virtual dose reduced datasets is subjected to the techniques expected to have most potential. The FDK reconstruction is smoothed with a standard deviation of 10 μm to mitigate noise and segmented by local thresholding. The SRS approach with the combined minimal entropy and relative difference prior is also applied to the downsampled projection data. As less projections result in less subsets under constant subset size, the number of iterations was increased such that all reconstructions received a similar amount of update steps and hence a similar state of convergence.

4.4.3 Evaluation

In the metaphysis of the registered ex vivo image, the boundary between cortical and trabecular bone was delineated in a 1 mm long region along the bone axis. All evaluations occurred on the 3D volume of interest containing only trabecular bone, as the aim of the proposed algorithm and other segmentation methods is explicitly to segment trabecular bone. Because of the registration, the volume of interest could be imposed on all segmentations.

Morphometric parameters are calculated within this region of interest with the CTAn software (SkyScan). Parameters of interest are bone volume fraction (BV/TV), trabecular thickness (Tb.Th), and trabecular number (Tb.N) (see

Section 2.4). While the number of unconnected objects (Obj.N) is generally not a reported morphometric index, we include it as a measure representing the connectivity of the segmented trabecular structures. The morphometric parameters are computed according to the "Guidelines for the assessment of bone microstructure in rodents using micro-CT" [9]. Results are presented as average values of the percentage errors from the ground truth, combined with the standard deviation on those errors.

As the morphometric parameters are averaged over the entire region, they do not evaluate the local overlap between segmentation and ground truth. It may be of interest to measure the overlap on a voxel by voxel basis. For this reason we compute the overlap coefficient o and the Dice coefficient d with the following equations

$$o = \frac{N_{00} + N_{11}}{N_{00} + N_{01} + N_{10} + N_{11}} \tag{4.34}$$

$$d = \frac{2N_{11}}{N_{01} + N_{10} + 2 * N_{11}} \tag{4.35}$$

where N_{ij} is the amount of voxels where the segmentation has value i and the ground truth value j. Both coefficients yield values of 0 for bad segmentations, and converge to 1 for exactly matching segmentations. Results are posted as average $\pm$ standard deviation over all the animals.

Overlap and Dice coefficients were analysed in SPSS software by one-way repeated measures ANOVA and corrected for sphericity with Greenhouse-Geisser. Post hoc comparisons were adjusted for multiple comparisons using the Bonferroni correction. Differences were considered significant at $p \leq 0.05$.

4.5 Results

In this section we provide the results of experiments that tested the presented method.

4.5.1 Model evaluation

While the objective function and optimisation methods seem valid in theory, it has to be verified that our desired solution is a maximum of the objective function and can be found by the selected optimisation approach. We test the validity of our model by initialising the optimisation with the ex vivo

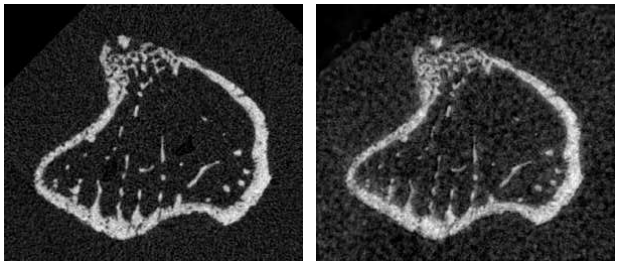

(a) Ground truth (b) MLTR

Figure 4.7: Verification of the acquisition model. (a) Ground truth image. (b) Reconstruction of in vivo data after 9 iterations of resolution modeling initialised with the ground truth image.

ground truth image, and performing the reconstruction with in vivo projections acquired with the 9 μm protocol. Ideally, after applying our iteration scheme, the found solution should not have diverged from the ground truth.

Results of this experiment are shown as a single slice in Figure 4.7. It can be seen that although more noise is introduced to comply with the projection measurements, the structure and thickness of the bone sample are well preserved after 9 iterations of resolution modeling (Figure 4.7(b)).

4.5.2 Performance of the priors

There are a wide variety of priors, and it has to be investigated which one yields the most satisfying results. We investigate the performance of the minimal entropy prior, which encodes intensity information. The relative difference prior, on the other hand, takes spatial information into account. It could be hypothesised that a combination of both intensity and spatial information might be better. The spatial influence is expected to be most beneficial in the presence of noise, therefore we evaluate the different priors on the 18 μm dataset, consisting of 5 male mice of 4 and 16 weeks old. A visual evaluation can be obtained from Figure 4.8. Note that the ME prior yields a more peaked histogram as expected.

The congruence between segmentations and ground truth by means of morphometric parameters is shown in Table 4.1. As similar morphometric errors were obtained for both 4 and 16-week old mice, all animals were pooled. The minimal entropy (ME) and combination of minimal entropy and relative

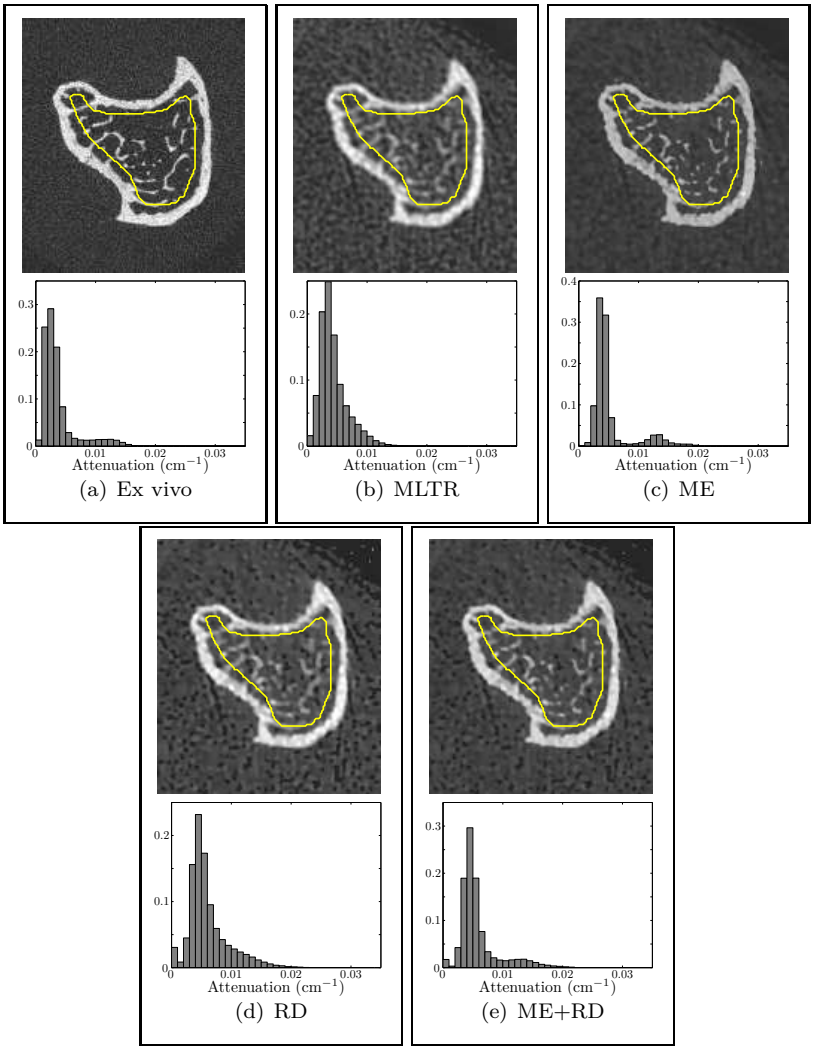

Figure 4.8: Comparison of in vivo SRS results obtained with different priors and their histogram distributions. (a) The ex vivo ground truth. (b) The MLTR reconstruction without prior. (c) The minimal entropy prior (ME). (d) The relative difference prior (RD). (e) The combination of minimal entropy and relative difference priors (ME+RD). Note that the ME prior yields a more peaked histogram. The histogram is computed in the the volume of interest, which is indicated by the contour.

Table 4.1: Average percentage error values from the ground truth (± standard deviations) for morphological parameters obtained with the SRS approach (n=5). The tested priors are no prior (MLTR), the minimal entropy prior (ME), the relative difference prior (RD), and the combination of minimal entropy and relative difference priors (ME+RD).

Method	BV/TV	Tb.Th	Tb.N	Obj.N
MLTR	-5.40 ± 21.17	21.51 ± 8.63	26.29 ± 15.46	31.06 ± 27.11
ME	15.15 ± 10.81	17.70 ± 8.56	9.19 ± 9.50	79.57 ± 44.43
RD	16.82 ± 18.39	21.24 ± 9.31	23.22 ± 14.51	27.84 ± 31.07
ME+RD	9.45 ± 10.39	18.78 ± 9.14	15.07 ± 8.95	26.10 ± 27.22

Table 4.2: Overlap and Dice coefficient average values (± standard deviation) for no prior (MLTR), the minimal entropy prior (ME), the relative difference prior (RD), and the combination of minimal entropy and relative difference priors (ME+RD) (n=5).

Method	Overlap	Dice
MLTR	0.927 ± 0.013	0.671 ± 0.021
ME	0.921 ± 0.015	0.678 ± 0.020
RD	0.924 ± 0.013	0.666 ± 0.021
ME+RD	0.926 ± 0.014	0.682 ± 0.023

difference priors (ME+RD) provide the best results. The spatial information incorporated in the relative difference prior seems to have a positive influence on the number of objects estimation.

As there is no prior which scores consistently better over all morphometric parameters, the overlap and Dice coefficients are reported in Table 4.2. These values are similar for all priors, impeding straightforward conclusions. We continue with the minimal entropy prior and the combined prior, as reconstructions with these priors obtained the highest Dice coefficients.

4.5.3 Segmentation quality

In this section the proposed method is compared to other segmentation methods. Table 4.3 shows the morphological parameters for images obtained with the 9 μm pixel size protocol. As similar morphometric errors were obtained for both OVX and sham-operated mice, all animals were pooled. These

Table 4.3: Average values of the percentage error from the ground truth of morphological parameters and average values of overlap and Dice coefficients for images obtained with the 9 μm pixel size protocol (n=7). The standard deviation of all measurements is indicated after the ± sign.

Method	BV/TV	Tb.Th	Tb.N	Obj.N	Overlap	Dice
Global	-31.64 ± 10.19	15.58 ± 1.91	-40.86 ± 8.60	53.20 ± 59.91	0.978 ± 0.005	0.645 ± 0.075
Local	-12.64 ± 17.54	17.49 ± 2.46	-25.69 ± 14.61	67.62 ± 67.50	0.979 ± 0.004	0.687 ± 0.075
Waarsing	14.28 ± 20.12	3.19 ± 7.03	10.32 ± 14.97	44.30 ± 55.18	0.975 ± 0.006	0.673 ± 0.074
SRS ME	-8.89 ± 13.59	0.85 ± 3.28	-9.45 ± 14.82	161.24 ± 123.42	0.979 ± 0.005	0.693 ± 0.083
SRS ME+RD	-18.27 ± 7.09	3.52 ± 2.63	-21.06 ± 4.90	42.40 ± 76.10	0.980 ± 0.003	0.696 ± 0.113

Table 4.4: Average values of the percentage error from the ground truth of morphological parameters and average values of overlap and Dice coefficients for images obtained with the 18 μm pixel size protocol (n=5). The standard deviation of all measurements is indicated ± sign.

Method	BV/TV	Tb.Th	Tb.N	Obj.N	Overlap	Dice
Global	-19.73 ± 25.43	20.10 ± 8.46	-33.74 ± 18.69	110.44 ± 88.38	0.924 ± 0.011	0.632 ± 0.027
Local	10.29 ± 17.70	23.30 ± 6.90	-10.64 ± 12.78	96.94 ± 87.40	0.912 ± 0.019	0.656 ± 0.025
Waarsing	34.86 ± 11.30	19.77 ± 10.40	12.83 ± 8.01	30.95 ± 29.58	0.899 ± 0.016	0.624 ± 0.030
SRS ME	11.66 ± 10.81	15.95 ± 8.56	-3.51 ± 9.50	68.94 ± 44.43	0.921 ± 0.015	0.678 ± 0.020
SRS ME+RD	1.75 ± 10.38	16.91 ± 9.14	-12.77 ± 8.95	9.38 ± 27.23	0.926 ± 0.014	0.682 ± 0.023

results of the morphological parameters confirm the theory described. Local thresholding outperforms global thresholding, while Waarsing thresholding particularly improves the thickness estimate. The proposed SRS method with the minimal entropy prior performs slightly better than the Waarsing method, except for the number of objects. The addition of spatial information with relative difference prior improves the Obj.N estimate, at the cost of larger errors for other indices.

The results of the 18 μm dataset are listed in Table 4.4. For these low quality, noisy images, the Waarsing algorithm obtains large overestimations of the bone volume fraction. This can be attributed to all trabeculae being thin relative to the resolution, while the heuristic correction formula assumes only the extremes are thin and accordingly adjusted. Lower overlap and Dice coefficients than for the 9 μm dataset, indicate worse performance on these lower dose images. In general, the SRS approach obtains similar or lower standard deviation values, indicating more consistent results.

For both datasets, the overlap coefficient is rather high for global segmentation, while the global segmentation approach yields the highest morphological parameter errors. The Dice coefficient indicates best performance for the SRS approaches, which corresponds with the general trend of the morphological indices. This better congruence, makes the Dice coefficient a more suitable estimator of morphometrical parameter performance.

The 12 samples were pooled and overlap and Dice coefficients were compared between the methods. Waarsing thresholding yielded overlap coefficients with a significantly lower mean compared to the other segmentation approaches. Both SRS priors obtained Dice coefficients with significantly higher means than global and Waarsing thresholding.

The segmentations of a particular slice of the 9 μm dataset are shown in Figure 4.9. The yellow outline indicates the trabecular region used for quantitative evaluation. Note that global, local and Waarsing segmentation methods are inferred from the FDK reconstruction of the image. The bad segmentation of the cortex in the locally thresholded image can be corrected easily, but is not done here as only the trabecular region is of interest.

4.5.4 Dose reduction

For in vivo imaging, limiting the dose is crucial to minimise radiation side effects. We investigate whether the increase in image quality obtained by the improved estimation of the morphological parameters can be used to reduce the dose and maintain similar bone structure estimates.

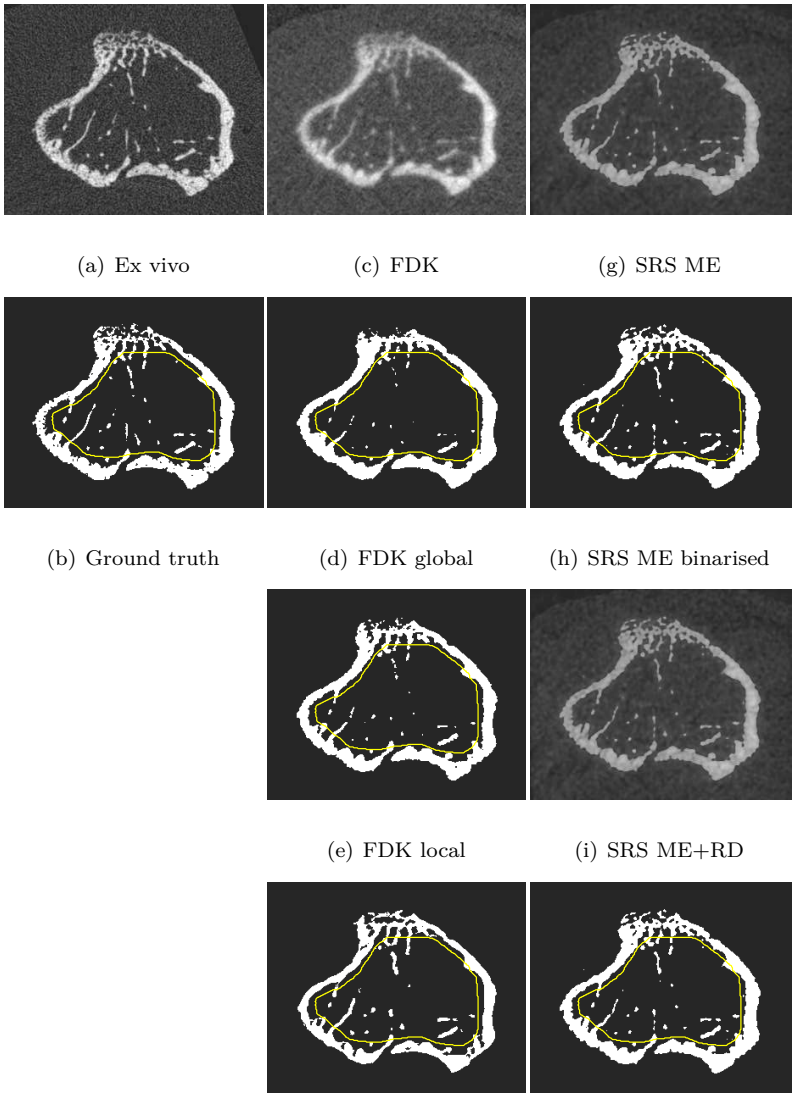

(a) Ex vivo (c) FDK (g) SRS ME

(b) Ground truth (d) FDK global (h) SRS ME binarised

(e) FDK local (i) SRS ME+RD

(f) FDK Waarsing (j) SRS ME+RD binarised

Figure 4.9: Representative segmentation results of one particular slice of the 09 μm dataset. The segmentation is evaluated in a region in the metaphysis consisting of 100 slices with a voxelsize of 10 μm. The region boundary is indicated on the segmented images by the contour.

With a constant tube voltage, the administered dose can be lowered by reducing the amount of projections (angular sampling) or by shortening the exposure time (noise sampling). In this experiment we investigate the influence of the angular sampling. An excised mouse tibia was scanned with the 9 μm pixel size protocol, but with 5 times more projections. The original protocol image can be obtained by using 1 in 5 projections for the reconstruction. The dose is virtually reduced by using less projections in the reconstruction.

Bone volume fraction, trabecular thickness, trabecular number and Dice coefficient measures are shown in Figure 4.10 for local thresholding and SRS, for a range of dose reduction factors. Reducing the dose gives larger underestimations for BV/TV and Tb.N and lower Dice coefficient values. The trabecular thickness is highly varying for local thresholding, while the thickness obtained from SRS reconstructions is less sensitive to dose reduction. In general, the SRS approach yields lower errors and higher Dice coefficient values than local thresholding.

The higher values of the Dice coefficient compared to the previous experiment can be explained by the higher bone volume fraction and increased trabecular thickness of the bone sample compared to the previous bone samples. In the presence of thicker trabeculae, it is easier to get a larger fraction of bone voxels correctly segmented.

4.6 Discussion

We propose a statistical iterative reconstruction algorithm, intended to segment bone from low quality μCT images. The resolution of the reconstruction is enhanced by modelling the blurring that occurs in the X-ray detector. A segmentation of the reconstruction is forced by adding prior information to the objective function and solving it with the MAP approach. We introduce the minimal entropy prior that aspires a maximal peakedness of the reconstruction histogram, deriving the retained attenuation values simply from the data.

The presented method is tested on images of a variety of mice hindlimbs: male and female, old and young, low as well as regular bone volume fractions, all scanned with in vivo protocols used in practice. Morphological parameters and their errors with respect to the high resolution reference are computed for the presented method as well as threshold-based segmentation methods. Our method generally obtains lower errors from the ground truth, most convincingly on the lowest quality images. Similar or smaller standard deviations on errors are observed for the proposed method, indicating more consistent results. The

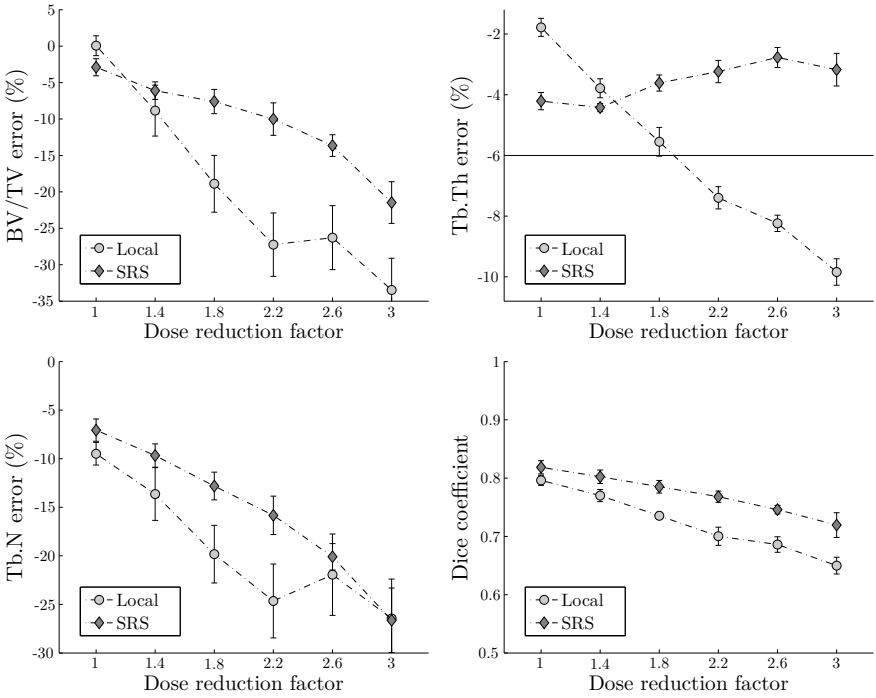

Figure 4.10: Effect of dose reduction on BV/TV, Tb.Th, Tb.N and the Dice coefficient (n=6). The error bars represent the standard deviation.

SRS approach yielded statistically significant improvements in Dice coefficient compared to global and Waarsing thresholding.

The minimal entropy prior does not include spatial knowledge, while it is known that trabecular bone is mostly connected. The relative difference prior does imply some sort of connectivity, and using it resulted in much better estimates for object number. The combined prior imposing both intensity and connectivity constraints provided the highest Dice coefficients.

The SRS technique performed better than typical threshold-based segmentation methods, because global and local thresholding do not correctly incorporate the system blurring in their method. Waarsing et al. correct for this blurring heuristically, which performs well on images of adequate quality. The method was validated on rats which have thicker trabeculae and can be expected to sustain more dose than mice [147]. Despite the smoothing step, the segmentation method of Waarsing turns out to be rather sensitive to noise. If an edge is assigned to noise, this threshold value will be extended over a

large region due to the dilation process, segmenting a patch of background into bone. To prevent this from occurring, the edge cutoff parameters are set to only retain the strongest edges, at the cost of missing thin trabeculae with relatively weak edges. Additionally, the heuristic correction formula for thin structures is unsuited for images where nearly all trabeculae are thin relative to the resolution. By segmenting during the reconstruction, the proposed method has the ability to model the system blurring as it physically occurs, resulting in an increased robustness towards noise and system blurring.

In an attempt to classify the different segmentation approaches with respect to performance, it is hypothesised that in general the different morphometric parameters should improve when more voxels are segmented correctly. Local voxel accuracy is quantified with overlap and Dice coefficients. The Dice coefficient was observed to correspond better to morphometric parameters than the overlap coefficient. This might be attributed to the omission of background voxels in the Dice coefficient computation.

A major drawback of the method is the high computational complexity, which is 100 times larger than FDK reconstructions combined with segmentation arithmetic. Graphical card implementations of the projector and backprojector exploit the parallel nature of the operations, and should yield reconstructions in a couple of hours. It could be argued that for preclinical applications the computation time is not a limiting factor to the adoption of the method.

The presented technique requires an estimate of the FWHM of the PSF of the combination of scanner and acquisition settings. The method models the detector blur, measurement of which requires dedicated tools. Scanning a phantom with a sharp edge, determining the PSF in the reconstruction image and multiplying that with the zoom factor, seems a feasible method to get an approximate value of the effective blur in the projection. This estimate includes other sources of blur, such as source wobbling and resolution blur, and results in modelling the effective blur by overestimating the detector blur. This effective blur value yielded satisfying results in the presented resolution modelling framework.

The sensitivity of the method to FWHM values is mitigated by the strength of the prior. Each reconstruction voxel contributes to the loglikelihood term as well as the prior term in the objective function. By gently increasing the strength of the prior there is a point where the effect on the prior dominates, and segmentation provides higher objective function values than correct projections. Setting the prior too high can force a segmentation when the resolution modelling has not yet converged. As a result, FWHM value, iteration scheme and prior strength are intertwined and should be optimised together.

While our method performed better than threshold-based segmentation models, errors of up to 15% remain for some morphometric indices. In our opinion, refining the model by adding scatter or focal spot blur would increase computational complexity without corresponding accuracy gain. A limitation of the study is the lack of comparison to other priors and other optimisation strategies. The amount of priors and optimisation approaches is endless, without consensus on any particular ones outperforming the other methods. In spite of arbitrary choices, the iterative procedure yields better results than the state-of-the-art threshold-based segmentation methods. Better convergence to the optimal reconstruction could be obtained with faster implementations. It is expected that other iterative approaches, such as discrete tomography, can obtain similar results if they incorporate resolution modelling. A minor drawback of the study is that segmentation parameters were determined from the same datasets on which the method is evaluated. The dose reduction experiment should be extended with more reconstructions in order to draw proper conclusions.

With regard to the prior information, the previous murine bone examples are relatively simple applications, consisting of just three different tissues that are known beforehand. As the minimal entropy prior does not require any input regarding the amount or intensity of image tissues, it can be applied to cases where the number of image tissues or their attenuation is unknown. For example in bone fracture models, a callus with unknown bone mineralisation density is expected to form and the minimal entropy prior could be useful. In the clinic, it could for example assist in segmenting the clinical CT data of a heart in the process of being ablated, to provide the surgeon with additional 3D information on the location of the catheters.

4.7 Conclusion

In this chapter, we have presented the minimal entropy prior that aspires maximal peakedness of the reconstruction histogram, deriving the retained attenuation values simply from the data. We used the prior in a statistical iterative reconstruction framework with resolution modelling to simultaneously reconstruct and segment low quality μCT bone images. With high resolution μCT images as ground truth, the method was shown to yield more accurate morphometric trabecular bone parameters than threshold-based segmentation methods. The approach yields opportunities for improved segmentations and dose reduction in a variety of applications.

Chapter 5

Dual energy CT reconstruction for a K-edge contrast material

5.1 Introduction

Micro-computed tomography systems offer sufficiently high resolution to image bone structures of small animals such as rats and mice in preclinical research [119]. Bone development and repair requires a normal vascular system to supply the bone with oxygen and essential nutrients. To study the interaction between the vasculature inside the bone and the bone itself, accurate information on their 3D structure is required. As it is not possible to discern blood from soft tissue by CT imaging, detecting vasculature requires altering the attenuation of blood by injecting a contrast agent based on iodine, barium, or lead. Small animals perfused with contrast agents based on lead or barium display high variability in attenuation of the contrast agent, even within the same vessel [88]. The high variability makes it hard to discriminate contrast agent from bone, which has a similar attenuation coefficient at such energies.

One approach to discriminate bone from vasculature is to use vascular corrosion casting: the perfused bony tissue sample is scanned by μCT, subsequently the calcium in the bone is chemically removed during a decalcification process, and finally the sample is scanned again with only the contrast agent having

high attenuation. Image post-processing allows to extract the vasculature from the second scan, and after registration with the first scan the bone can be determined. The decalcification process can take weeks, and can induce morphological changes [121]. To overcome these limitations, dual energy μCT imaging has recently been used to distinguish bone from vascular contrast agents [45].

Dual energy CT enables discrimination of materials with similar linear attenuation coefficients. For dual energy CT applications, two datasets of the same object are acquired with two spectrally separated X-ray beams. Dual energy algorithms convert the attenuation integrals in the projection domain into tissue specific properties in the image domain, enabling the discrimination of materials with similar linear attenuation coefficients. The K-edge of an element is a sudden increase in the attenuation coefficient at an X-ray energy just above the binding energy of the K-shell electron. X-rays with a higher energy than the binding energy can be absorbed and cause an increase in the attenuation. If this K-edge lies in the imaging energy range, it can be exploited.

Both noise and beam hardening can be problematic when using a μCT system to image vasculature around bony tissue in small animals. Limiting radiation dose to prevent radiation effects is essential for in vivo experiments and negatively influences the noise. For ex vivo measurements, obtaining images with high signal-to-noise ratios can require cumbersome long scan durations, and heat dissipation issues. In addition, blood vessels filled with highly dense contrast agent or the presence of metal implants can cause significant beam hardening artifacts. Hence, this application would benefit from a dual energy algorithm that is robust to noise and beam hardening.

Algorithms for dual energy CT reconstruction can be classified as either post-reconstruction, pre-reconstruction or iterative. Post-reconstruction dual energy techniques first reconstruct the two sets of projection data into attenuation coefficients. With knowledge about the attenuation of some basis materials at both energies, material fractions can be computed from the attenuation coefficients on a voxel by voxel basis [67, 144]. This approach is computationally simple and has been applied to μCT [45]. However, this voxel by voxel comparison of attenuation coefficients is sensitive to noise. For instance in [45], dual energy imaging of a rat specimen by μCT was performed based on an averaging of 6 scans to reduce the noise. Attempts to reduce the sensitivity to noise are being investigated [107]. Additionally, beam hardening effects influence the accuracy of this method, because the X-ray spectrum is usually not incorporated in the reconstruction [148].

In pre-reconstruction methods the measured line integrals are converted to basis function integrals, and these are reconstructed into basis function coefficients [2,

158]. This approach is also sensitive to noise, as the decomposition step is nonlinear and amplifies the noise [65, 47]. Furthermore, exactly the same line integrals have to be measured with the two distinct X-ray spectra, excluding for example the use of fast kV switching CT systems, in which the X-ray tube alternates voltage between adjacent views, or dual source CT systems in which the two sources are positioned at a 90 degrees angle of each other. This constraint limits the applicability of a pre-reconstruction approach.

Iterative methods formulate an objective function that models the energy dependence of the attenuation coefficient, and can therefore be expected to cope better with dense materials than the other approaches. The incorporation of statistical noise models leads to better signal-to-noise ratios. The function can be formulated using least squares [131], maximum likelihood with Poisson noise [23], or penalised likelihood [81]. Most iterative dual energy reconstruction techniques are either unable to deal with K-edge materials [131] or require a third measurement [130] or the use of photon-counting detectors [116], that are not yet widely available. Recently, an iterative method was presented that can solve for more basis functions by grouping the basis functions in triplets and assigning to each voxel the most likely triplet [81].

We propose an iterative dual energy maximum likelihood reconstruction algorithm that allows a K-edge material to be present in the object and that requires only two spectral measurements. The purpose is to discriminate bone from contrast agent in μCT images as robust to noise as possible. First, we revise the post reconstruction approach and the usual attenuation model. We then introduce the adaptive material constraints and detail the maximum-likelihood reconstruction. A preliminary version of this model was published in [29]. Simulated and real experiments illustrate the potential of the method and strengths and weaknesses of the proposed method and experiments are discussed.

5.2 State of the art

5.2.1 Post-reconstruction approach

A standard dual energy post-reconstruction approach was implemented by Granton et al. [45]. The two projection data sets acquired at energy E_i are reconstructed separately by FDK. For every voxel that consists of three additive

base materials, the following set of equations is valid

$$\mu(E_1) = f_1\mu_1(E_1) + f_2\mu_2(E_1) + f_3\mu_3(E_1) \tag{5.1}$$

$$\mu(E_2) = f_1\mu_1(E_2) + f_2\mu_2(E_2) + f_3\mu_3(E_2) \tag{5.2}$$

$$1 = f_1 + f_2 + f_3 \tag{5.3}$$

with f_m the tissue fractions and $\mu_m(E_i)$ the attenuation of base material m for photons with energy E_i. This explicitly assumes that the sum of the volumes of the three base materials is equivalent to the volume of the mixture [80]. The set of equations is solved for f_m for every image voxel using non-negative least squares [45], as tissue fractions cannot be negative. The attenuation of the different substances at each energy $\mu_m(E_i)$ is computed from a manually delineated, representative region in the appropriate reconstruction. The base materials we used for this approach are soft tissue, bone and the contrast agent. Regions for which this model was not valid (such as air in the background) are excluded from analysis, as they require a different triplet of base materials to be modelled correctly. A more rigourous way to deal with such regions is to solve the equations for a variety of triplets, thus allowing multi-material tissue decomposition [92]

5.2.2 X-ray attenuation model

Beam hardening artifacts are caused by the faulty assumption that the X-ray beam in μCT systems is monochromatic, while dual energy applications attempt to exploit the dependence of the linear attenuation coefficient on the photon energy. Reducing beam hardening and differentiating materials with similar attenuation coefficients both benefit from using a polychromatic model to account for the energy spectrum of the X-ray beam and the energy dependence of the material attenuation. The dependence of the linear attenuation coefficient μ on the photon energy E can be described by a linear combination of B basis functions $\alpha_b(E)$

$$\mu(E) = \sum_{b=1}^{B} a_b\alpha_b(E) \tag{5.4}$$

with b the index of the basis function and a_b the coefficient of the basis function.

It has been shown that 2 basis functions are enough to approximate all materials without a K-edge in the imaging energy range [76]. A possible set of basis

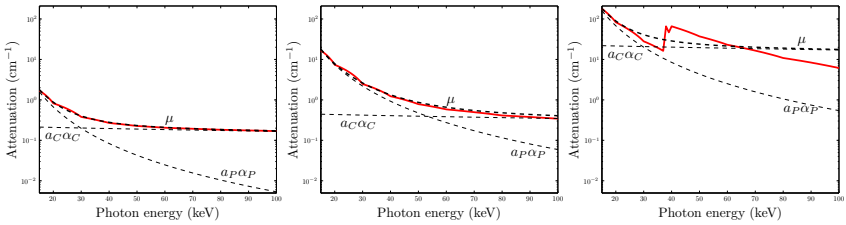

(a) Soft Tissue (b) Bone (c) Barium sulfate

Figure 5.1: Least squares fitting of the photoelectric (α_P) and Compton (α_C) basis functions to the exact attenuation (shown in the solid line) for soft tissue, bone and barium sulfate, according to Equation 5.5. While the approximation is good for soft tissue and bone, it cannot model the K-edge of barium correctly.

functions $\alpha_b(E)$ are the energy dependent mass attenuation coefficients of two basis materials, e.g. water and calcium. Alternatively, functions that describe the physical effects of electromagnetic radiation with matter can be chosen. In the relevant energy range, these are the photoelectric interactions $\alpha_P(E)$, modelled as $1/E^3$, and the Compton scattering $\alpha_C(E)$, modelled by the Klein-Nishina function [2]:

$$\mu(E) \approx a_C\alpha_C(E) + a_P\alpha_P(E) \tag{5.5}$$

This approximation works well for materials such as soft tissue and bone, but is not able to model barium sulfate well (Figure 5.1). In clinical CT scanners, the low energy X-rays emitted by the X-ray source that will not pass through the patient are filtered to minimise the administered radiation dose. As a result, the energy range of the clinical X-ray beam typically lies between 40 and 140 keV [62, 108]. The K-edges of contrast agents such as iodine (33.2 keV) and barium (37.5 keV) fall outside the imaging energy range, and equation 5.5 is valid. For μCT applications, the energy range of the X-ray beam is typically from 20 to 100 keV due to smaller samples. As a result, when the attenuation is modelled as the sum of photoelectric and Compton scatter components, a third basis function modelling the mass attenuation coefficient of the K-edge material α_K has to be added [112, 116].

$$\mu(E) \approx a_C\alpha_C(E) + a_P\alpha_P(E) + a_K\alpha_K(E) \tag{5.6}$$

The improved modeling of tissues containing the K-edge is shown in Figure 5.2. Solving Equation 5.6 for the coefficients a_P, a_C and a_K requires three

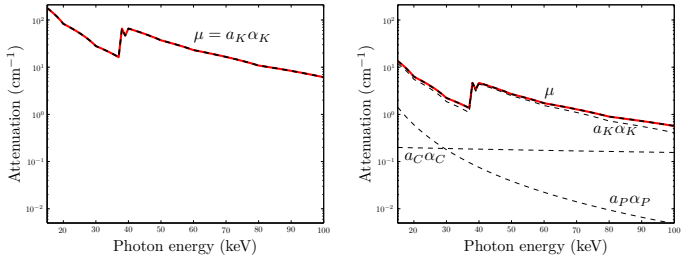

(a) Barium sulfate (b) 30% m/v barium sulfate

Figure 5.2: Least squares fitting of the photoelectric (α_P), Compton (α_C) and barium sulfate (α_K) basis functions to the exact attenuation (shown in the solid line) for barium sulfate and 30% m/v barium sulfate, according to Equation 5.6.

measurements at different energies. These measurements can be obtained by taking a third CT scan [130], or in a single scan by using multi-bin photon counting detectors [116]. We adopt the approach of De Man et al. and restrict the relative weights of the photoelectric and Compton components based on material assumptions [23].

5.3 Dual energy reconstruction for a K-edge

5.3.1 Theory

Material constraints

The coefficients a_P and a_C of the Compton scatter and photoelectric basis functions $\alpha_C(E)$ and $\alpha_P(E)$ are plotted in Figure 5.3a (circles) for some materials without K-edge that are of interest in a biomedical μCT imaging. The coefficients are computed by applying a least squares fit of Equation 5.5 to the known energy dependent attenuation coefficient (data from the National Institute of Standards and Technology) of these materials. Voxels containing a single material without K-edge should be assigned a pair of coefficients (a_P, a_C) equal to the corresponding combination for this material. At tissue borders, partial volume voxels can be expected to contain multiple materials.

We assume that all voxels in the image contain, in addition to a possible K-edge material, a combination of not more than 2 adjacent base materials (air, soft tissue), (soft tissue, bone), (bone, aluminium), such that only combinations of

a_P and a_C that lie on the dashed line in Figure 5.3(a) are allowed. Under this assumption, the relationship between a_P and a_C can be approximated by a piecewise-linear curve defined by the precomputed coefficients $c^m = (c_P^m, c_C^m)$ of a set of m base materials. For more details about this model, we refer to De Man et al. [23].

For our choice of base materials, both a_P and a_C are monotonic functions of the monochromatic attenuation μ_{mono} of the base materials at a reference energy E_{ref} (Figure 5.3(b)). As a result, μ_{mono} defines both a_P and a_C via a set of base materials, for example [air, soft tissue, bone, aluminium]. However, μ_{mono} is the monochromatic attenuation accounted for by the Compton scatter and photoelectric basis functions only, and does not account for attenuation contributions by other basis functions. As μ_{mono} is not representative of the actual monochromatic attenuation, we will denote it by a_{CP}. With these material constraints the attenuation model becomes

$$\begin{aligned} \mu(E) \quad &\approx \quad a_C(a_{CP}, c^m)\alpha_C(E) + a_P(a_{CP}, c^m)\alpha_P(E) \\ &\qquad +a_K\alpha_K(E) \end{aligned} \tag{5.7}$$

As there are only two unknown values (a_{CP}, a_K) in each voxel, the solution can be found with just two measurements at different energies.

In practice, the precomputed constraints on the basis materials c^m might not correspond exactly to the experimental data. As Equation 5.5 is an approximation, c_P^m and c_C^m are determined using a least squares fit. In the experimental case, the fitting is weighted by the spectrum of the X-ray beam, leading to deviations from the precomputed values of c^m. In the case of multiple spectral measurements, the different spectra should be taken into account by weighting the least squares fit with the corresponding spectra. To compensate for experimental deviations from our theoretical model, such as slight differences in X-ray source spectra or detector properties, we allow the basis function coefficients of the basis materials c^m to adapt to the data, and treat them as values to be optimised.

We allow variation of the coefficients that make up a base material, not the attenuation of a base material. This implies that the values of material constraints c_P^m and c_C^m can change, allowing the decomposition of base materials to move freely to a more appropriate position in Figure 5.3(a). The monoenergetic attenuation of a base material at a reference energy E_{ref} should not change, meaning that the coefficients can only move vertically in Figure 5.3(b).

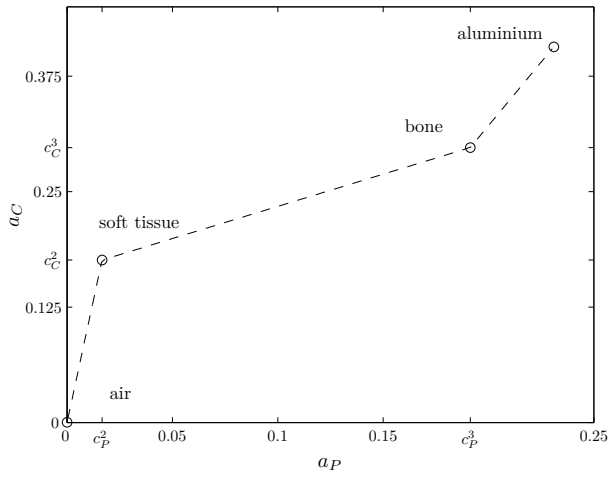

(a)

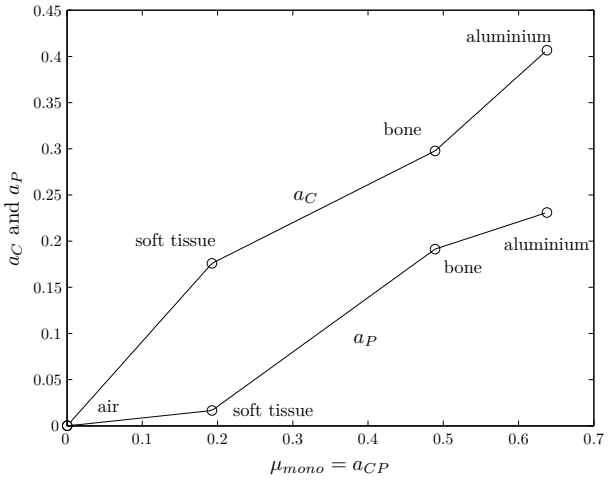

(b)

Figure 5.3: Illustration of the material assumptions for the set of base substances [air, soft tissue, bone, aluminium]. (a) Photoelectric coefficient versus Compton scatter coefficient. (b) Monochromatic linear attenuation coefficient at 70 keV versus photoelectric coefficient and Compton scatter.

Generalised attenuation model

To allow comparisons of different attenuation models, we formulate a generalised framework in which the different models fit:

$$\mu(E) \approx a_C(a_{CP}, c^m)\alpha_C(E) + a_P(a_{CP}, c^m)\alpha_P(E) + \sum_{b=1}^{B} a_b\alpha_b(E) \qquad (5.8)$$

The generalised framework allows application of the material constraints between photoelectric and Compton scatter basis functions and any number of basis functions B. The framework puts no assumptions on the basis functions, except that they compose an adequate model for the imaged object.

For $a_{CP} = 0$, Equation 5.8 becomes a traditional modelling of independent basis functions, for $B = 0$ (i.e. without the sum term) it becomes the IMPACT model presented by De Man et al. [23] with fitting of the material constraints, and for $B = 1$ and $\alpha_1(E) = \alpha_K(E)$ it becomes the proposed algorithm for a K-edge material. The required number of spectral measurements equals the length of the vector of unknowns $\boldsymbol{a}$:

$$\boldsymbol{a} = \begin{bmatrix} a_{CP} & a_1 & a_2 & \dots & a_B \end{bmatrix}^T \qquad (5.9)$$

Maximum likelihood optimisation

The goal of the reconstruction is to determine the values of $\boldsymbol{a}$ in every voxel. We pursue the same maximum likelihood approach with Poisson noise model as in Chapter 4. The loglikelihood L is given by

$$L = \sum_i y_i \ln(\bar{y_i}) - \bar{y_i} \qquad (5.10)$$

with y_i the acquired noisy projection ray i, and $\bar{y_i}$ the expected projection ray i.

To account for the energy dependence of the X-ray spectrum and attenuation coefficients, the forward model is extended to a polychromatic model, as

presented by De Man et al. [23]

$$\bar{y}_i = \sum_{k=1}^{K} \bar{y}_{ik} \tag{5.11}$$

$$= \sum_{k=1}^{K} b_{ik} e^{-\sum_j l_{ij}\mu_{jk}} \tag{5.12}$$

with k the energy index and b_{ik} the total energy of photons with energy k detected by detector i in absence of an object. b_{ik} models the source spectrum and the detector sensitivity and is different for each distinct spectral acquisition. It is considered known as it can be computed from the scanner characteristics. l_{ij} is the intersection length of projection i with voxel j, and μ_{jk} is the discretised $\mu(E)$ in voxel j at energy index k:

$$\mu_{jk} = a_C(a_{CP,j}, c^m)\alpha_{Ck} + a_P(a_{CP,j}, c^m)\alpha_{Pk} + \sum_b a_{b,j}\alpha_{bk} \tag{5.13}$$

The loglikelihood is iteratively maximised by updating a in voxel j with the update steps presented by Nuyts et al. [101]:

$$a_j^{n+1} = a_j^n + \Delta a_j^n \tag{5.14}$$

$$\Delta a_j = -\frac{\frac{\partial L}{\partial a_j}}{\sum_h \frac{\partial^2 L}{\partial a_j \partial a_h}} \tag{5.15}$$

Considering all partial derivatives, we have to distinguish the update steps for a_{cp} and a_b:

$$\Delta a_{CP,j} = -\frac{\frac{\partial L}{\partial a_{CP,j}}}{\sum_h \frac{\partial^2 L}{\partial a_{CP,j}\partial a_{CP,h}} + \sum_h \sum_b \frac{\partial^2 L}{\partial a_{CP,j}\partial a_{b,h}}} \tag{5.16}$$

$$\Delta a_{b,j} = -\frac{\frac{\partial L}{\partial a_{b,j}}}{\sum_h \sum_l \frac{\partial^2 L}{\partial a_{b,j}\partial a_{l,h}} + \sum_h \frac{\partial^2 L}{\partial a_{b,j}\partial a_{CP,h}}} \tag{5.17}$$

In detail, the derivatives are given by the following formulae:

$$\frac{\partial L}{\partial a_{b,j}} = \sum_i l_{ij} e_i Y_i^b \tag{5.18}$$

$$\frac{\partial L}{\partial a_{CP,j}} = a'_{C,j} \sum_i l_{ij} e_i Y_i^C + a'_{P,j} \sum_i l_{ij} e_i Y_i^P \tag{5.19}$$

$$\sum_h \frac{\partial^2 L}{\partial a_{b,j} \partial a_{l,h}} = -\sum_i l_{ij} H_i Z_i^{bl} \tag{5.20}$$

$$\sum_h \frac{\partial^2 L}{\partial a_{CP,j} \partial a_{b,h}} = -\sum_i l_{ij} H_i \left(a'_{C,j} Z_i^{Cb} + a'_{P,j} Z_i^{Pb} \right) \tag{5.21}$$

$$\sum_h \frac{\partial^2 L}{\partial a_{CP,j} \partial a_{CP,h}} = -a'_{C,j} \sum_i l_{ij} M_i - a'_{P,j} \sum_i l_{ij} N_i \tag{5.22}$$

where these shorthand notations were used:

$$e_i = 1 - \frac{y_i}{\bar{y}_i} \tag{5.23}$$

$$Y_i^s = \sum_k \alpha_{sk} \bar{y}_{ik} \tag{5.24}$$

$$Y_i^{st} = \sum_k \alpha_{sk} \alpha_{tk} \bar{y}_{ik} \tag{5.25}$$

$$Z_i^{st} = e_i Y_i^{st} + \frac{y_i Y_i^s Y_i^t}{\bar{y}_i^2} \tag{5.26}$$

$$M_i = \sum_h l_{ih} a'_{C,h} Z_i^{CC} + \sum_h l_{ih} a'_{P,h} Z_i^{CP} \tag{5.27}$$

$$N_i = \sum_h l_{ih} a'_{C,h} Z_i^{CP} + \sum_h l_{ih} a'_{P,h} Z_i^{PP} \tag{5.28}$$

$$a'_{s,j} = \frac{\partial a_s}{\partial a_{CP,j}} \tag{5.29}$$

$$H_i = \sum_h l_{ih} \tag{5.30}$$

Additionally, the material constraints c_C^m and c_P^m are optimised to maximise the likelihood. Generalising the coefficient notation to c_q^m where $q = \{C, P\}$ distinguishes between the Compton and photoelectric constraints, the update steps become:

$$\Delta c_q^m = -\frac{\frac{\partial L}{\partial c_q^m}}{\sum_{j,h,r,o} \frac{\partial^2 L}{\partial c_q^m \partial c_r^o}} \tag{5.31}$$

$$\frac{\partial L}{\partial c_q^m} = \sum_j D_{jq}^m \sum_i l_{ij} e_i Y_i^q \tag{5.32}$$

$$\frac{\partial^2 L}{\partial c_q^m \partial c_r^o} = -D_{jq}^m D_{hr}^o \sum_i l_{ij} l_{ih} Z_i^{qr} \tag{5.33}$$

$$D_{jq}^m = \frac{\partial a_{q,j}}{\partial c_q^m} \tag{5.34}$$

with h another pixel, r another basis function $\{C, P\}$ and o another material. Note that these constraints apply to all voxels.

Convergence properties

A function is concave if all its second derivatives are non-positive. The derivatives $a'_{s,j}$ are always positive because a_C and a_P are monotonic functions. Hence all the second derivatives of the loglikelihood will be non-positive if for any combination of basis functions s and t

$$Z_i^{st} \geq 0 \tag{5.35}$$

$$\left(1 - \frac{y_i}{\bar{y}_i}\right) Y_i^{st} + \frac{y_i Y_i^s Y_i^t}{\bar{y}_i^2} \geq 0 \tag{5.36}$$

α_s and α_t are always positive, and the measured detector energy $\bar{y}_{ik}$ is nonnegative. Hence, all Y_i are nonnegative.

In the neighbourhood of the optimum, $y_i \approx \bar{y}_i$, and the second derivative of the likelihood is non-positive if

$$\frac{1}{\bar{y}_i} Y_i^s Y_i^t \geq 0 \tag{5.37}$$

which is always the case. As a result, the algorithm will converge to the global optimum if initialised close enough to the optimum.

Computational complexity

Equation 5.12 requires K projections of μ_{jk}. If we substitute μ_{jk} with Equation 5.13, we can see that it can be calculated more efficiently by projecting the basis function coefficients $\boldsymbol{a}$ and weighting the projections with the energy dependent basis functions α.

$$\bar{y}_i = \sum_{k=1}^{K} b_{ik} e^{-\sum_j l_{ij}\left(a_C \alpha_{Ck} + a_P \alpha_{Pk} + \sum_b a_{b,j} \alpha_{bk}\right)} \tag{5.38}$$

$$= \sum_{k=1}^{K} b_{ik} e^{-\alpha_{Ck} \sum_j l_{ij} a_C - \alpha_{Pk} \sum_j l_{ij} a_P - \sum_b \alpha_{bk} \sum_j l_{ij} a_{b,j}} \tag{5.39}$$

The proposed model with material constraints and one K-edge material requires in each update step 3 projections to compute Equation 5.12, 3 backprojections to compute the first derivatives (Equations 5.18 and 5.19), 1 backprojection to compute Equation 5.20, 2 backprojections to compute Equation 5.21, 2 projections of the derivatives of $a_{C,j}$ and $a_{P,j}$ to compute M_i and N_i, and 2 backprojections in Equation 5.22. This results in a total of 5 projections and 8 backprojections. Without the K-edge basis function, this would reduce to 4 projections and 4 backprojections.

Updating the material constraints requires an additional 4 projections. The material constraints are optimised at each update of the basis function coefficients to prevent faulty constraints from propagating errors throughout the reconstruction images.

5.3.2 Implementation choices

The algorithm is implemented in IDL. The discretisation of the energy dependence of the various functions and Gibbs overshoot requires special attention.

Energy sampling

The polychromatic model requires a discretisation of the spectrum and of the basis functions. As the method exploits the K-edge jump in the K-edge basis function $\alpha_K(E)$, the sampling should be fine enough to retain the K-edge jump in the discretised K-edge basis function. In our implementation, we assure this is the case by generating two energy bins, split exactly at the K-edge energy. The two bins can then be split up into smaller bins to obtain the requested amount of K energy bins.

A reasonable approach to determining the remaining bin edges would be to select spectrally equally important bins. The spectrum can be computed as

$$b(E) = I(E)F(E)D(E)E \tag{5.40}$$

The X-ray spectrum $I(E)$ emitted by the X-ray source is given by the spectra measured by Hammersberg et al. [46]. The source emitted spectrum is adjusted with filters F, detector sensitivity D and multiplied with the energy to account for the energy-integrating characteristics of the detector.

Selecting spectrally equally important bins then comes down to defining the range of energies r_k that belong to each energy bin k, so that equally large b_{ik} values are obtained.

$$b_{ik} = \frac{\int_{r_k} b(E)dE}{\int b(E)dE} \tag{5.41}$$

The r_k are computed using the spectrum of the first measurement, and applied to compute the b_{ik} of all spectral measurements. The discretisation of the basis functions can then be computed as

$$\alpha_{bk} = \frac{1}{r_k}\int_{r_k} \alpha_b(E)dE \tag{5.42}$$

The Compton scatter and photoelectric basis functions are normalised to have unit value at the reference energy E_{ref}. The K edge basis function is the mass attenuation coefficient so that coefficients a_K will represent the mass volume fraction of the K-edge material.

Gibbs overshoot

In the unconstrained dual energy algorithm, the coefficients of the Compton scatter and photoelectric effect basis functions converge to their optimal values.

The Compton scatter basis function converges faster than the photoelectric basis function, causing Gibbs overshoots to be observed at tissue edges. These artifacts are a convergence problem, and disappear after many iterations. The constrained dual energy algorithm does not suffer from these artifacts, as the Compton and photoelectric coefficients are tied to each other. When adding a third basis function to model the K-edge, Gibbs overshoot is observed in the K-edge coefficients. To minimise these effects and limit the amount of iterations required for a converged image, the K-edge coefficients a_K are kept zero during the first iteration.

5.4 Experimental setup

Experiments are conducted on different simulated and real data sets to analyse the behaviour of the different models and to compare the iterative approach to the post-reconstruction approach.

Reconstructions with the proposed method are initialised with a uniform image, use the set of basis materials given by [air, soft tissue, bone, aluminium], perform 50 iterations, are sped up with 100 ordered subsets [56], use $K = 15$ energy bins, and are computed with a reference energy E_{ref} of 70 kV.

5.4.1 Simulations

Simulated projections of a virtual phantom were generated that modelled the X-ray spectrum (K=30), material attenuation and detector characteristics, while ignoring scatter. Material mass attenuation coefficients were obtained from the XCOM web database [7], and may deviate slightly from the attenuation model of Equation 5.6. The low energy X-ray beam corresponded to a tube voltage of 70 kV and a filter of 0.5 mm aluminium, while the high energy scan put the tube voltage at 100 kV and used a filter of 0.5 mm aluminium and 0.038 mm copper. These filters were used because they are installed by default on our SkyScan 1172 μCT system. At each energy 400 projections were acquired.

The first simulation experiment investigates the effect of updating the material constraints by reconstructing noiseless projections. The phantom is designed to represent a mouse paw consisting of soft tissue, a ring of cortical bone, and three pieces of trabecular bone. The acquired projection data were reconstructed with 3 different methods: the dual energy model, the constrained dual energy model without updating the constraints, and the constrained dual energy model

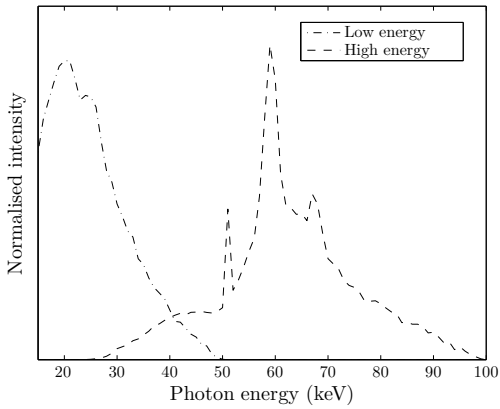

Figure 5.4: Normalised intensity distributions of the low and high energy X-ray spectra used in the measurements.

with updating the constraints. The projection sets acquired at both energies are used in all these reconstructions.

In the second simulation we added three perfused blood vessels to the mouse paw phantom. The contrast agent is a mixture of water and barium sulfate with 0.3, 0.2 and 0.15 gram barium sulfate per ml mixture in the three regions respectively, to mimic the variability in attenuation. Different amounts of Poisson noise were included in this simulation. The data was reconstructed using the constrained dual energy model with updating the constraints. This phantom is used to validate the constrained dual energy model with a K-edge material.

5.4.2 Measurements

Real μCT measurements were acquired to investigate the influence of realistic noise conditions. 360 projections were acquired with a low energy X-ray beam of 50 kV tube voltage and 0.5 mm aluminium filter, and 360 projections were acquired with a high energy X-ray beam of 100 kV tube voltage and a filter of 0.5 mm aluminium and 0.038 mm copper. The X-ray spectra corresponding to these settings are shown in Figure 5.4. These measurements have previously been presented at a conference [29].

The first measurement consists of a polypropylene tube filled with water that contains a mix of barium sulfate, water and gelatine to prevent sedimentation, and a cylinder of bone equivalent material, calcium hydroxyapatite (CaHA).

The vasculature around bone was investigated in real small animal data. Mice were first perfused with ± 10 ml of heparinised saline to remove the blood, then with ± 10 ml of a 10% neutral-buffered formalin solution to fix the tissue and afterward with ± 10 ml of saline to remove the formalin. Finally, animals were perfused with ± 5 ml of a preheated 30% m/v barium sulfate solution (Micropaque, Guerbet) containing 2% gelatin. After perfusion, animals were placed on ice for at least 1 hour to allow the gelatin to solidify, before removing the hind legs for μCT analysis.

Both projections datasets were decomposed into tissues by the post reconstruction approach and the proposed approach, but without updating of the constraints.

5.5 Results

5.5.1 Simulations

The results of the simulated mouse paw are shown in Figure 5.5. The results of the unconstrained dual energy decomposition are shown in the top row. When using the constrained single energy model (second row), oscillations appear in both components. They occur because the optimal combination of (a_P,a_C) is not allowed by the material constraints. The algorithm alternates voxels with allowed combinations so that the average of multiple voxels approaches the optimal combination. When the material constraints are updated (third row) this issue is resolved, and the results are similar to those of the dual energy decomposition. In Figure 5.6 it can be seen that the only substantial change of constraints is the Compton coefficient of bone. Note that the final material constraint for bone does not necessarily correspond to the actual bone coefficients, the actual coefficients merely lie on the piecewise-linear curve.

The results of the simulated perfused mouse paw under different noise conditions are shown in Figure 5.7. It can be seen that the contrast agent a_K is recovered in all cases. A quantitative evaluation of the obtained K-edge basis function coefficients is given in Table 5.1. The reconstructed coefficients for barium sulfate correspond well with the expected values. Bone and soft tissue are attributed low levels of barium sulfate, particularly when the noise increases.

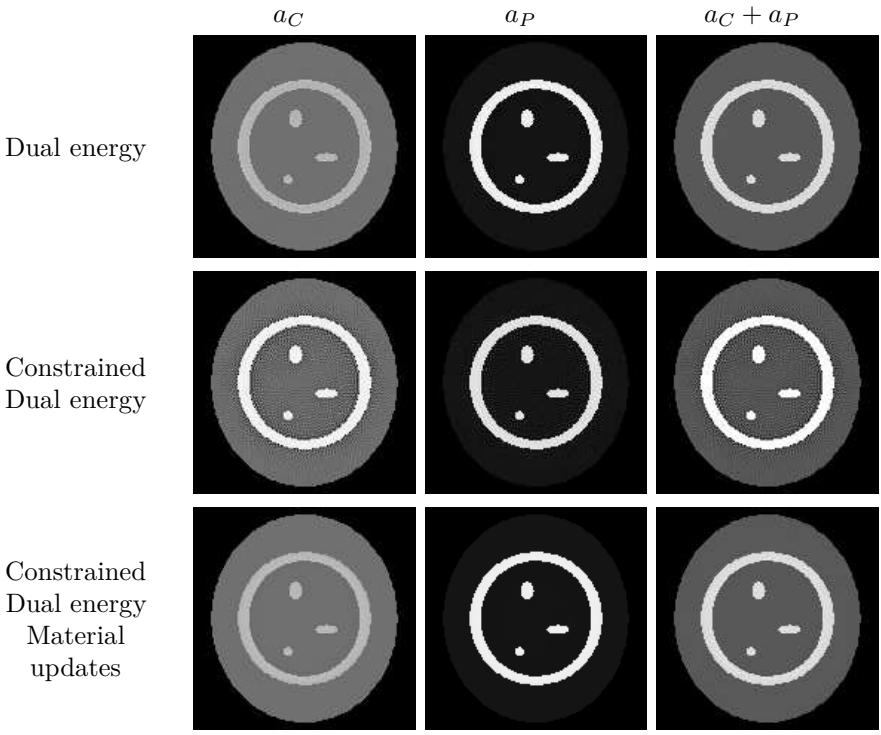

Figure 5.5: Dual energy reconstruction of the simulated mouse paw. The top row shows the results of the dual energy decomposition. The second row shows that applying material constraints without updates results in oscillations. The third row illustrates that applying the constraint updates resolves the oscillations. Each column is shown with the same window-level.

Table 5.1: Quantitative evaluation of the images in Figure 5.7. Coefficients of a_K for different mass volume fractions (m/v) of barium sulfate, bone and soft tissue under different noise conditions. Values are reported as average ± standard deviation (n=5).

	Expected	No noise	Mild noise	Strong noise
30% m/v $BaSO_4$	0.300	0.294	0.297 ± 0.010	0.305 ± 0.010
20% m/v $BaSO_4$	0.200	0.197	0.202 ± 0.006	0.201 ± 0.013
15% m/v $BaSO_4$	0.150	0.150	0.155 ± 0.007	0.151 ± 0.010
Bone	0	0.003	0.009 ± 0.001	0.016 ± 0.003
Soft tissue	0	0.005	0.014 ± 0.001	0.024 ± 0.001

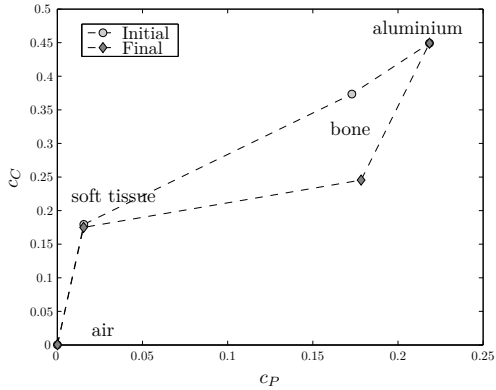

Figure 5.6: The initial and final material constraints for the dual energy reconstruction with constraint updates of Figure 5.5. The only substantial change is the Compton coefficient of bone. Note that the final material constraint for bone does not necessarily correspond to the actual bone coefficients, the actual coefficients merely lie on the piecewise-linear curve.

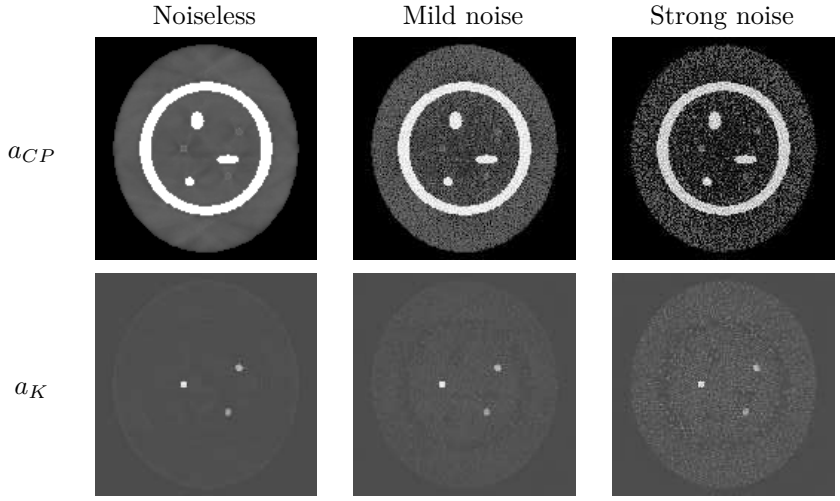

Figure 5.7: Constrained dual energy reconstruction with material updates of a simulated perfused mouse paw. The contrast agent is recovered in all cases. Each row is shown with the same window-level.

5.5.2 Measurements

The results of the phantom measurement are shown in Figure 5.8. The FDK reconstruction shows a beam hardening artefact between the CaHA and the contrast and is noisy (Figure 5.8(a)). It is hard to tell which circle is contrast agent and which is bone from this image. The post-reconstruction tissue decomposition results in a coefficient of variation of 0.36 in the barium sulfate region (Figure 5.8(b)). The iterative approach is more robust to noise in these conditions with a coefficient of variation of 0.15 in the same region (Figure 5.8(c) and (d)). Due to the inhomogeneity of the CaHA, some particles exhibit K-edge behaviour and are detected as such by both methods.

Finally, the proposed method is tested on an ex vivo mouse tibia perfused with barium sulfate. In the FDK reconstruction of Figure 5.9(a), the two large grey structures represent bone, while the white dots are cross sections of blood vessels perfused with barium sulfate. Due to noise, the post-reconstruction decomposition considers several bone voxels as contrast agent (Figure 5.9(b)), while the iterative approach does not suffer from this issue (Figure 5.9(c)). The vasculature can be interpreted more easily when viewed as a red overlay on the FDK reconstruction (Figure 5.9(d)).

5.6 Discussion

In clinical settings, the K-edge of contrast agents falls out of the imaging range and does not require a dedicated model. We have proposed a method that can deal with K-edges in the imaging energy range, as is the case in preclinical μCT imaging. Material constraints developed by De Man et al. are applied to parameterise the Compton and photoelectric basis functions with a single value per voxel, compensating the unknown introduced by the additional basis function. The dual energy measurements hamper correct computation of the material constraints and these are therefore optimised with respect to the likelihood.

The validity of the material constraints and their updates are shown on simulated images. Although some tissues are attributed a small amount of K-edge material, the concentrations of barium sulfate are reconstructed to their expected values. The method was shown to exhibit better noise and beam hardening properties than a typical post reconstruction approach on a phantom measurement. We show that the method allows imaging of the bone and a K-edge contrast agent with a standard μCT desktop system.

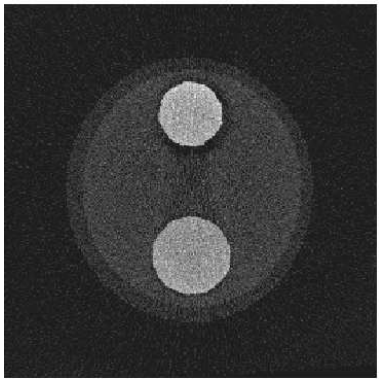

(a) FDK reconstruction

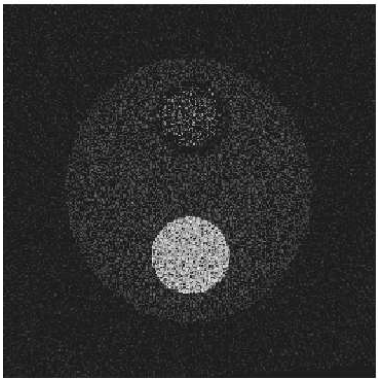

(b) Barium sulfate fraction

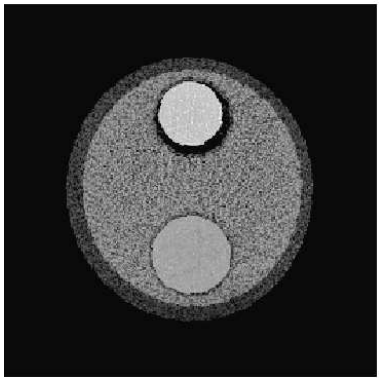

(c) a_{CP}

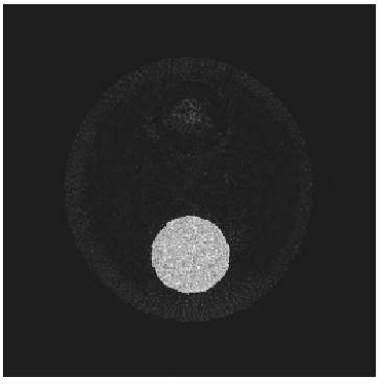

(d) a_K

Figure 5.8: Results of the phantom. (a) FDK reconstruction of the 50kV image. (b) Barium sulfate tissue fractions as estimated by the post-reconstruction approach. (c) Monochromatic reconstruction a_{CP} of the iterative method at 70kV, without the barium sulfate component. (d) The barium sulfate component a_K as computed by the iterative method.

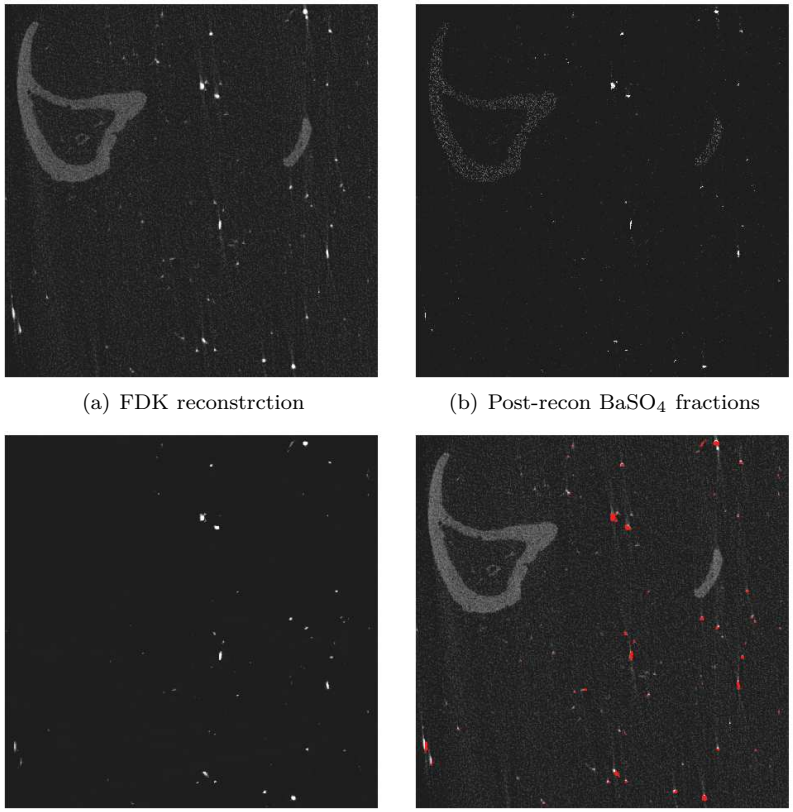

(a) FDK reconstrction

(b) Post-recon $BaSO_4$ fractions

(c) Coefficients of a_k

(d) Overlay of a_K on (a)

Figure 5.9: Results of the mouse tibia. (a) FDK reconstruction of the 50kV image. (b) Barium sulfate tissue fractions as estimated by the post-reconstruction approach. (c) The barium sulfate component a_K as computed by the iterative method. (d) Overlay of the contrast a_K in red on (a).

As with any iterative reconstruction method, the increased modelling accuracy comes at the cost of significant increased computational complexity compared to post reconstruction approaches. Although this should not deter the adoption of the method in preclinical research, it could be worthwhile to investigate whether update steps can be found with less projections or backprojections per iteration.

Most approaches model the attenuation with two basis functions, which can be considered linear combinations of Compton scatter and photoelectric effect. This implies that the the other X-ray interaction with matter, Rayleigh scatter and pair production are deemed negligible. Pair production can indeed be disregarded as it requires X-ray energies of at least 1.022 MeV, which is not achievable with current μCT X-ray tubes. The omittance of Rayleigh scatter is debatable, but its cross sectional area is typically an order of magnitude smaller than the dominant interaction effect at any X-ray energy in the CT imaging range.

In the presented attenuation model, a K-edge material was added to the model, allowing dual energy reconstructions on μCT images with contrast agents. The additional unknown basis function coefficient is compensated by removing an unknown variable under the assumption that besides K-edge material, each voxel consists of not more than 2 adjacent base materials. The assumption allows flexibility in the choice of base materials and experience indicates that the assumption holds well in practice.

Truncated projections are generally not a problem in iterative reconstruction methods, as all attenuating tissue located outside the field of view contributing to the projections, is attributed to a few voxels right outside the field of view. These compensatory voxels are highly unlikely to satisfy the material constraints, hence imposing the material constraints on all the voxels in the image requires the object to be entirely positioned in the field of view. A possible work-around to apply the proposed method to truncated projection data could involve a limited number of voxels to which the material constraints do not apply.

A specific application where combined bone and vasculature information is desirable, are bone grafts (see Section 6.4). A common object in images of bone grafts is the metal pin used to stabilise to graft. The pin in question consists of stainless steel type AES 304, an alloy composed primarily of iron, chromium and nickel. Although the alloy material does not violate the assumptions in the attenuation model, it could not be reconstructed correctly. The chemical characterisation of the metal was confirmed with energy dispersive X-ray spectroscopy. Polychromatic simulations of the alloy correspond well to measurements of the pin. A satisfying explanation has not been found.

The attenuation model with material constraints restricts the allowed combinations of Compton and photoelectric coefficients in a voxel, indirectly limiting noise in the reconstruction. A more aggressive noise reducing strategy could be to include a prior and resort to the MAP approach. The MAP approach enables the incorporation of spatial information into the algorithm as well. For the current applications, integration of this additional information was deemed unnecessary.

The presented method is shown to behave as expected on simulations, and the performance in realistic noise conditions is evaluated on measurements. Validation of the method would benefit from experiments on additional measurements. In particular, the phantom measurement was limited to a single acquisition, and no exact ground truth of contrast density was available due to precipitation of barium sulfate. The experiment should be repeated with multiple measurements of an iodine based contrast agent of which the iodine content is known exactly.

The proposed method is formulated in a generic framework, enabling straightforward application to datasets containing no or multiple K-edge materials, acquired with photon counting detectors or with different scanner geometries, provided that the number of measurements matches the number of unknowns.

5.7 Conclusion

We have presented an iterative dual energy maximum likelihood reconstruction algorithm, that is able to deal with one K-edge material. Hence, our method provides the ability to discriminate contrast enhanced structures such as vasculature from surrounding bony structures. The algorithm is based on a relationship between two of the three basis functions describing the energy dependence of the linear attenuation coefficient. We adopt the relationship between Compton and photoelectric coefficients of common substances presented by De Man et al. [23], and adjust it to cope with multiple energy measurements. This relationship is then applied to parameterise the Compton and photoelectric basis functions with a single value per voxel. By reducing the number of unknowns to two per reconstruction voxel, this approach does not require a third scan or a photon counting detector and can therefore be applied to any kind of CT scanner. The algorithm is validated on simulated and real μCT images of bone and barium sulfate contrast agent. The method performs better than a typical post-reconstruction approach with respect to beam-hardening and noise at the expense of increased computation time.

Chapter 6

Applications

6.1 Introduction

The protocols and algorithms developed in the previous chapters are interesting in their own right, yet the aim of the research is to answer relevant bone research questions. In this chapter, we list a few examples of how the developed algorithms and expertise can contribute to and benefit life science research. First, we verify the reliability of μCT imaging by comparing morphological parameters with those obtained by histology. As blood vessels are suggested to affect bone formation, the vasculature of an ischemic mouse model is characterised. Finally, the complementary information provided by both bone and vasculature μCT imaging is illustrated in a study concerning bone grafts.

The discussed applications do not intend to validate the presented reconstruction techniques, which have been evaluated in their respective chapters. The purpose of the chapter is to illustrate the biological relevance of the developed quantification and visualisation software, that can process data obtained by both conventional approaches and the presented algorithms. As these applications have been pursued at the same time as more fundamental methodological work, our reconstruction algorithms were not always available when analysing datasets.

6.2 Validation of μCT with histology

6.2.1 Introduction

The traditional gold standard method of imaging the internal structure of bone is histology. The histological procedure typically consists of sectioning and staining the tissue, after which an image at high resolution can be acquired with light microscopy. The advent of μCT systems provides opportunities to non-destructively image the internal bone structure in 3D. For reliable results, μCT imaging should provide accurate and reproducible images. As it has been shown that μCT images are reproducible when imaged in the same system [143], we investigate the accuracy in this section.

A high correlation between histology and μCT has previously been found for human bone specimens [73, 97]. For the detection of trabecular bone in small animals, more demands are put on the image resolution [147, 19]. We verify if a typical ex vivo scan setup resulting in a 5 μm voxelsize image provides sufficient resolution to accurately quantify bone morphometric indices.

6.2.2 Materials and methods

Sample and image acquisition

A tibia removed from a wild type mouse was scanned in the Skyscan 1172 μCT system. The voltage and current of the X-ray source were put at 50 kV and 200 μA. 481 projections with an angle stepsize of 0.400 degrees were taken. These projections were reconstructed using the NRecon software (SkyScan) to produce a 3D image with an isotropic voxel size of 5.04 μm.

After μCT scanning the piece of bone underwent histological treatment, as explained in Section 2.3.1. Concisely, the entire bone was cut longitudinally in slices of 4 μm thick, subjected to von Kossa staining, and photographed under a microscope with a varying pixelsize between 1.06 and 2.18 μm. The standard procedure cuts 55 slices, of which alternatingly 10 are kept and 5 are discarded. This yields 4 sets of 10 consecutive slices, with 5 slices missing in between every set. Out of every set of 10 slices, three are stained and imaged, resulting in 12 photographed slices. Exceptionally for this experiment the procedure was extended for the entire bone, yielding 150 photographed sections with limited artifacts. The slices were numbered in the order that they were cut, so that they could be realigned in their relative positions.

Registration

Consecutive histological slices were registered to each other using MIRIT [86] with a rigid transformation matrix. This assumes that the slices differ only due to their positioning on the microscope, and is invalid for artifacts generated by the histological process such as crevices or cracks.

The aligned histological sections could be stacked on top of each other to create a pseudo-3D or ∼3D image. 5 such images were generated, each containing 12 different sections, distributed through the sample conform the histological procedure, with blank slices inserted for missing sections. These images were registered with a single rigid transformation matrix to the 3D μCT image to investigate feasibility of the registration.

A series of 41 subsequent histological sections without major artifacts were stacked to create a ∼3D image, resulting in a high resolution image with a voxelsize of $2.05\times2.05\times4$ μm. This image is registered to the μCT image to evaluate 3D morphometric indices.

Quantification

Histology as well as ex vivo μCT images are generally segmented using a global threshold. The histology image is converted to greyscale by retaining only the red colour channel. All image blocks were segmented with Otsu's automatic threshold for further investigation [104].

To evaluate the congruence of histological sections and μCT images, morphological parameters are computed on three sets of corresponding regions of interest. Three different setups are investigated: 2D images, ∼3D, and a full 3D measurement.

In order to obtain trabecular morphometric indices from 2D histology images, care must be taken to have representative samples of the bone. Typically, three sections of the bone are sampled, and on each section three non-overlapping rectangles of 500×400 μm are selected. Structural parameters are computed on each 2D rectangle, and averaging the obtained values over the 9 rectangles provides a good estimate of the parameter. This method is referred to as the 2D measurement.

In a second approach the ∼3D image consisting of 41 consecutive histological sections was resampled to an isotropic voxelsize of 4 μm and a volume of interest was delineated. Morphological parameters are computed in 3D from these

~3D images. To improve the image quality, the histological ~3D image was smoothed and morphologically closed to remove small cracks in the bone.

Finally, a volume of interest comprising the entire trabecular region was delineated on the μCT image, and 3D morphometric indices are computed on this volume. This approach is the standard μCT analysis procedure and in this section we call it the full 3D measurement.

Care was taken upon selecting the regions and volumes of interest in the metaphysis to remain at least 0.5 mm and at most 3 mm below the growth plate, and to contain only trabecular bone. For both the 2D and the ~3D measurement, the selected regions could be transferred to the μCT image thanks to the registration, and the measurements were also performed on the μCT data. The full 3D measurement can only be performed on the μCT image.

For all approaches, the morphometric indices BV/TV, Tb.Th, Tb.N and Tb.Sp are computed. The 3D measurements were computed with CTAn (SkyScan). As 3D measurements cannot be performed on 2D images, assumptions about the 3D structure of the bone are required (see Section 2.4). We assume that the structure follows the plate model and use the following definitions for 2D measurements [27]

$$\text{Tb.Th} = 2\frac{\text{BV}}{\text{BS}} \tag{6.1}$$

$$\text{Tb.N} = \frac{\text{BV/TV}}{\text{Tb.Th}} \tag{6.2}$$

$$\text{Tb.Sp} = \frac{1}{\text{Tb.N}} - \text{Tb.Th} \tag{6.3}$$

with BV the bone volume and BS the bone surface, extrapolations of the 2D bone area and perimeter respectively. The computation of trabecular thickness assumes a plate model, and the other parameters are a function of the trabecular thickness and thus rely on the same assumption. The 2D measurements were computed in Matlab (Mathworks, MA, USA).

6.2.3 Results

Registration

The different ~3D images consisting of 12 sections and blank slices could all be registered successfully to the μCT image. Registrations were deemed successful

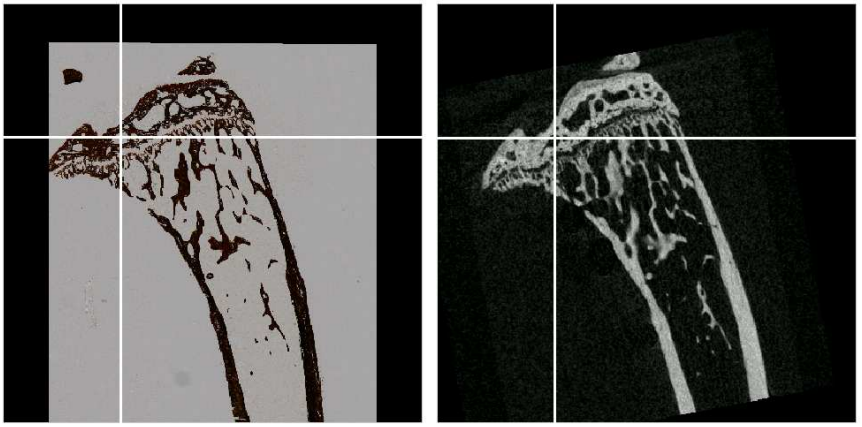

Figure 6.1: Results of the registration of an image containing 12 histological sections with the μCT image. Left a slice of the histological image, right the corresponding plane in the 3D μCT image. The red lines occupy the same relative position.

if object landmarks were visually confirmed to occupy the same relative position. An example of a successful registration is shown in Figure 6.1.

The result of the registration of the μCT and ~3D image of 41 subsequent histological sections is shown in Figure 6.2. The histological image on the top shows much finer details of the growth plate which is blurry in the μCT image at the bottom. When examining images orthogonal to the histological sections, the bone in the histological image is jagged due to imperfect registration and artifacts.

Quantification

The computed morphometric indices are listed in Table 6.1. For the indices computed on 2D regions of interest, μCT yields slightly thicker trabeculae, resulting in an increased BV/TV. This can be attributed to the decreased resolution of the μCT in the 2D plane compared to histology.

The histological ~3D images show decreased values of trabecular thickness and trabecular number compared to both the corresponding μCT measurement and the 2D measurements. These effects can be attributed to small cracks in trabeculae, and the jaggedness of the bone in the dimensions perpendicular to the histological sections, which both hardly influence the bone volume fraction.

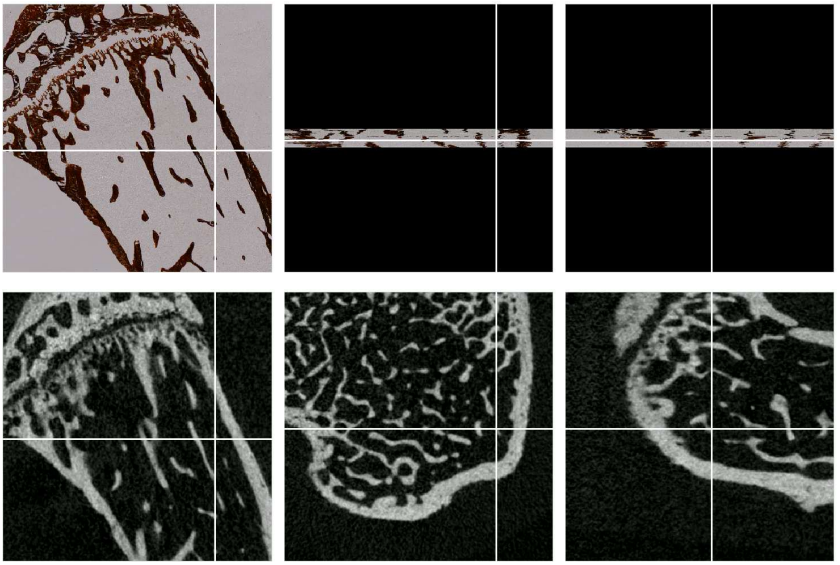

Figure 6.2: Results of the registration of ~3D image with 41 subsequent histological sections. The top row contains three orthogonal views of histological image, the bottom row the corresponding planes in the μCT image. The red lines denote the location of the corresponding planes.

Table 6.1: Morphometric indices computed from histological and μCT images with the different approaches. The 2D measurements are reported as mean $\pm$ standard deviation, the 3D methods resulted in a single value.

Method	BV/TV (%)	Tb.Th (mm)	Tb.N ($mm^{-}1$)	Tb.Sp (mm)
Histology 2D	14.15 $\pm$ 1.53	0.046 $\pm$ 0.002	2.91 $\pm$ 0.34	0.34 $\pm$ 0.036
μCT 2D	16.35 $\pm$ 0.80	0.053 $\pm$ 0.001	2.99 $\pm$ 0.21	0.32 $\pm$ 0.014
Histology ~3D	15.37	0.027	5.59	0.10
μCT ~3D	17.01	0.043	3.89	0.12
μCT full 3D	14.25	0.046	3.08	0.17

The volume of interest selected in the ~3D image has a larger bone volume fraction due to to a decreased trabecular separation, compared to the entire trabecular region. Except for the trabecular separation, all 2D histomorphometric measurements correspond fairly well to the full 3D μCT measurement. It appears that the trabecular separation index is most sensitive to violations of the plate model assumption in the 2D measurement.

6.2.4 Discussion

We have shown that registration of histological sections acquired by a standard procedure with a 3D μCT image is feasible, provided that a sequential numbering of the sections is available. Additionally, a ~3D histological image can be registered with the μCT image and shows a higher resolution in the sagittal plane.

The quantification showed that the 2D morphological indices computed on the same volumes produced lower BV/TV and Tb.Th values for histology than for μCT. Except for trabecular separation, the full 3D μCT measurement correlates well with the 2D histological sections measurement.

Histology provides a high resolution image in one dimension, but is time consuming, destructive, and requires assumptions to compute characteristics of the 3D structure. μCT imaging obtains similar morphometric indices with a faster, reproducible, and non destructive approach that provides 3D information.

6.3 Visualisation and quantification of vasculature

6.3.1 Introduction

Bone development and repair requires a normal vascular system to supply the bone with oxygen and essential nutrients. μCT imaging can provide 3D vascular information if the subject is perfused with a contrast agent such as barium sulfate prior to scanning. Unfortunately such contrast agents have attenuation coefficients similar to bone, and the variation in attenuation can be high, making it hard to discriminate the contrast from bone. This discrimination can be done by manual delineation (if the interest is not in the vasculature close to the bone), by vascular corrosion casting, or by dual energy approaches (see Chapter 5). In this section we assume that the vascular information has been obtained with one of these methodologies, and that visualisation and quantification of the vessel network is of interest.

In this study we investigate whether changes in the vascular network induced by ischemia can be visualised and characterised. A disruption in the blood flow causes hypoxia (a lack of oxygen), which stimulates the secretion of angiogenic growth factors, stimulating at first the formation of a dense network of thin blood vessels, which are later remodelled in a mature vascular network [48]. Although the images in this study were not acquired with dual energy μCT,

this experiment is discussed for validatory purposes, as the ischemia model is well studied. In section 6.4, the vascular network will be analysed from dual energy images.

6.3.2 Materials and methods

The femoral artery was ligated in the right leg of two mice, with the left leg left unharmed as control. Three weeks post-ligation, the animals were perfused with barium sulfate and had both hindlimbs scanned by ex vivo μCT (50 kV, 200 μA, 590 ms, 3 frame averages, 321 projections, 0.5 mm Al filter). As the vascular characteristics were not considered to be close to the bone interface, the dual energy approach was not required.

A volume of interest containing the vascular network was delineated on a number of slices and the delineations were interpolated to obtain a full volume of interest. Proximal and distal boundaries of the volume were determined from representative femoral landmarks. The bone was manually delineated and interpolation yielded the volume of interest encompassing the bone. The bone volume of interest was excluded from the vascular volume of interest.

The bone was segmented using a global threshold in the bone volume of interest. The vasculature was segmented using hysteresis thresholding, which was originally proposed for use in the Canny edge detector [16]. Hysteresis thresholding consists of two thresholds. Voxels with intensities below the lower threshold are omitted, voxels above the upper threshold are retained, and intermediate voxels are retained if they are connected to retained voxels. The hysteresis thresholding is followed by a despeckle step, both steps attempt to minimise the influence of noise. The vasculature tree was analysed with the algorithm proposed by Selle et al. [123]. This algorithm determines the skeleton of the vascular network, and then detects branch points and builds a graph. Every graph edge is assigned a radius corresponding to the vessel thickness by measuring the minimal distance between any two opposite points on the vessel boundary surface, in a plane perpendicular to the centerline.

The graph allows for easy computation of the total skeleton length representing the combined length of all blood vessels, the combined skeleton length of blood vessels of a certain thickness, and the number of branch points. All quantifications were normalised to the unit volume. To avoid measuring differences in perfusion quality, all parameters were normalised with respect to the left control leg. Dedicated software was developed in MeVisLab (MeVis Medical Solutions AG and Fraunhofer MEVIS, Bremen, Germany) to facilitate processing, visualisation and quantification of vasculature.

6.3.3 Results

3D models of the vasculature in a control leg and after ligation in the same mouse are shown in Figure 6.3. The colour of the blood vessels indicated the local vessel diameter. It can be observed that the ischemic leg has a denser network of vessels. This was confirmed quantitatively in Figure 6.4, with the ischemic hindlimbs having larger vessel volumes, longer skeleton lengths and more branch points than their control counterparts.

To investigate the contribution of vessels of different thicknesses to these global measures, the contribution to the skeleton length of vessels of different diameters can be plotted (Figure 6.5). Vessels with diameters up to 150 μm contribute more to the skeleton length in ischemic legs compared to control legs. For vessels of larger diameters this incongruity between ischemic and control hindlimbs is not observed. This difference can also be observed by the vessel colours in Figure 6.3, where the ischemic model shows an increase of predominantly yellow blood vessels.

6.3.4 Discussion

In this section we have presented methods for visualising and quantifying the vasculature network. In an aggressive pathology model such as ischemia, trends could already be picked up from a sample of only two mice. These techniques are not limited to imaging blood vessels in the described hindlimb, but have already been applied to for example brain vasculature [140]. Due to the high interest in investigating and quantifying vasculature, software has been developed that is being used by 4 different KULeuven research groups. Besides the intensive collaborations with clinical and experimental endocrinology, the software is being used by researchers in cardiology (Dieter Dauwe), molecular and vascular biology (Ine Vandersmissen) and biomedical MRI [140], indicating the relevance of the conducted research.

As can be seen from the 3D models, several perfused vessels are composed of unconnected patches, while in reality they form a connected vessel network. This patchy behaviour is not a resolution effect, as it is observed in nanoCT images as well (data not shown), but is likely tissue dependent. In the same mouse, the vasculature surrounding the bone was observed as disconnected, while for example the kidney portrays a well connected vascular network (data not shown). It is hypothesised that perfusion near bone is more challenging possibly due to a different structure or composition of the blood vessels. While this aspect should be kept in mind, it is not a limitation of the imaging

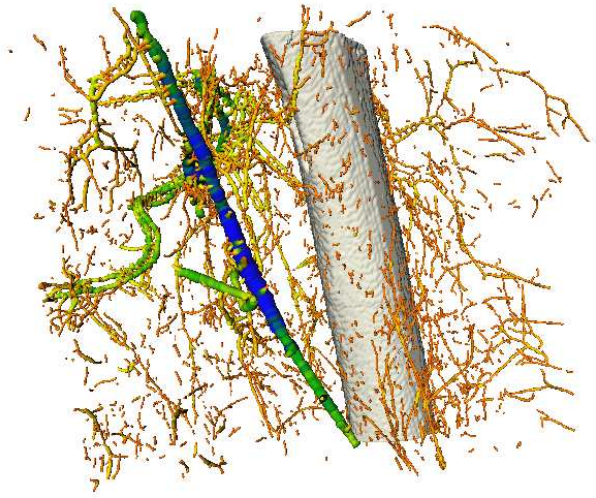

(a) Control

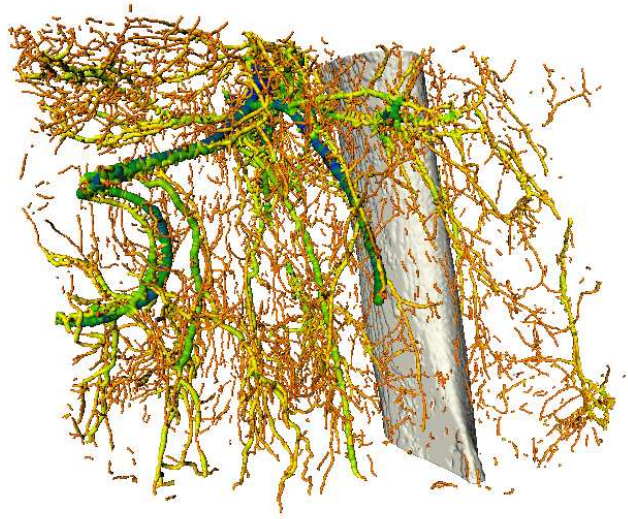

(b) Ischemia

Figure 6.3: 3D visualisation of vasculature in a control situation and after induction of ischemia. The vessel colour codes the local vessel diameter, with red representing 0 μm, yellow 80 μm, green 160 μm and blue 320 μm.

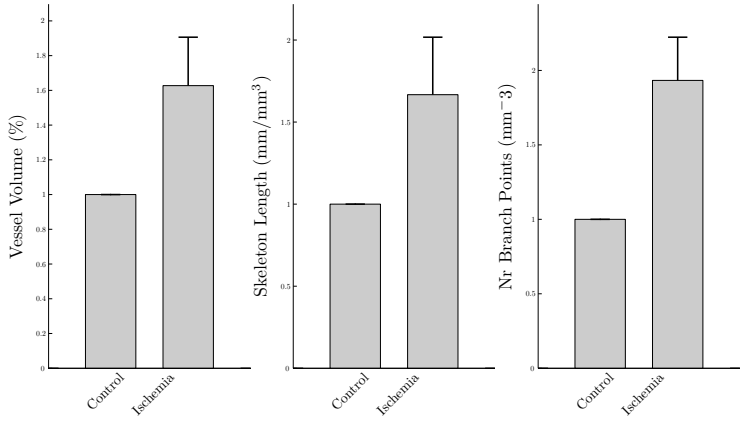

Figure 6.4: Quantitative parameters of the vascular network (n=2). The data is normalised to the values in the control leg and the error bars represent the standard deviation.

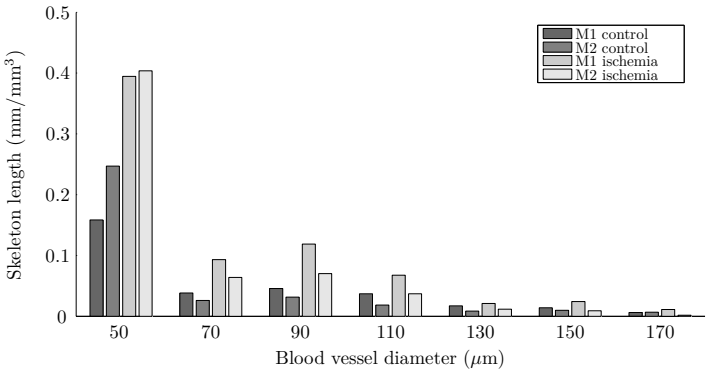

Figure 6.5: Contributions of vessels of a certain diameter to the skeleton length. For each diameter, the results of the ischemic leg of mouse 1 (M1) and 2 (M2) are plotted, followed by the control legs of both mice. The ischemic leg has more vessels of these small diameters than the control legs.

methodology, and can be mitigated by comparing the vasculature to the control limb that can be considered to have a similar perfusion quality.

6.4 Quantification of bone healing in bone grafts

6.4.1 Introduction

Although bone has an enormous regenerative capacity, 10% of all bone fractures result in slow or defective healing. To fill the gap between bone ends in large bone defects, a substitute bone graft or engineered material can be implanted. Bone tissue engineering is a relatively new research domain that tries to promote bone repair by engineering materials and cells that stimulate bone formation. Stem cells can be incorporated on the bone graft to stimulate the formation of blood vessels and bone. A metal pin is implanted to secure the graft in the required position.

Bone healing can be characterised by the formation of a callus, a mixture of woven bone and cartilage that is formed around the fracture. The bone graft, the host bone and the callus can be visualised and measured using μCT imaging. Additionally, bone healing is assumed to be highly influenced by the vascular network, which can also be detected by μCT. In this section, we analyse both the bone and the vasculature in a graft mouse model of bone healing.

6.4.2 Materials and methods

Animals and image acquisition

In 8-week old mice, a 4 mm diaphyseal segment of the femur was removed and replaced by either an autograft or allograft, fixed with a pin. Prior to implantation, the cell-free allografts were imaged with the ex vivo SkyScan 1172 system. Four weeks after implantation, the animals were sacrificed and their femur was subjected to different imaging protocols. Three animals of each condition were scanned by ex vivo μCT with typical settings to obtain images for callus quantification. Six animals of each condition were subjected to immunohistochemistry with CD31 to visualise the vasculature 2.5.1.

To evaluate the vasculature in 3D with μCT, six animals of each condition were perfused with barium sulfate and imaged using dual energy μCT. The effective energy of the beam was adapted to be once below and once above the K-edge by adjusting the maximum tube voltage and the filter. The perfused bone

samples were first scanned with the low energy beam, obtained by setting the peak voltage to 50kV and filtering the beam with 0.5 mm of aluminium. For the high energy scan, the settings were altered to a maximal tube voltage of 100 kV and filtering with 0.5 mm of aluminium and 0.038 mm of copper. Both scans were performed with an image pixel size of 5 μm in the SkyScan 1172 μCT system and both filters are standard installed on this scanner. To reduce noise, both scans were performed over 360 degrees with a rotation step size of 0.6 degrees and a frame averaging of 3.

Although in the results presented here the bone and vasculature were evaluated on different samples, both analyses can be performed on the data obtained by the perfusion experiment. Callus formation had been analysed first on non-perfused samples and yielded conclusive results, time constraints prevented us from repeating the same analyses on perfused datasets.

Bone quantification

The metal pin used to stabilise the bone grafts within the bone defect results in streak artifacts in reconstructed μCT images, hampering correct interpretation and quantification of the images. To reduce the metal artifacts, μCT projection data was reconstructed using an iterative reconstruction technique and projection completion. The iterative reconstruction technique partly models the physics behind the metal artifact by modelling the noise [101]. Projection completion replaces the projection rays through the metal with values interpolated between the measured data [41]. This results in datasets with reduced metal artifacts.

Custom made software was made in MeVisLab to visualise and analyse the obtained μCT images. The images were segmented in the different tissue classes. Due to its high attenuation, voxels belonging to the metal pin could be determined easily with a global threshold value. Distinguishing between graft and callus is not straightforward as bone remodelling can alter the graft greatly, especially in autografts. The boundary between graft and callus was manually delineated on a number of slices, and interpolated to form the boundary at slices in between. When the allograft had been scanned with μCT prior to implantation, the pre-implant graft was spatially aligned to the post-implant graft with registration software based on mutual information [86]. In this case, manual delineation was superfluous as the boundary could be obtained by slightly dilating the pre-implant graft. The graft was segmented with global thresholding in the obtained graft region. The callus was segmented in the region outside of the graft using hysteresis thresholding in order to discriminate low density cartilage from noise peaks.

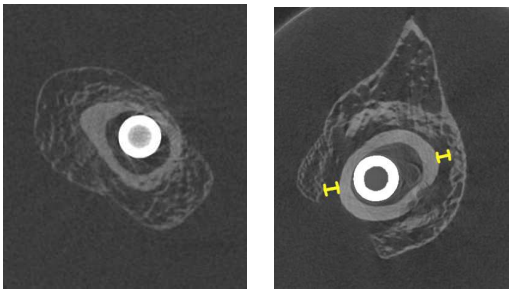

(a) Union (b) Non-union

Figure 6.6: Examples of union and non-union between callus and graft bone. In (a) the callus forms a union with the graft. In (b) the callus remains at a distance form the graft, as indicated by the distance marks.

To determine a representative region of interest for analysis, the image was realigned with the main axis of the graft. The 5% lower and upper parts of the graft were removed, to obtain a region where the graft can be assumed to be cylindrical in any cross-sectional slice. For every slice we calculate the union ratio and the coverage ratio. The union ratio estimates the union between graft and callus and is computed by Reynolds et al. as the percentage of the graft surface of which the first 55 μm along the surface normal are callus [111]. Both the inside and outside surface of the graft contribute to the union ratio in each slice [111]. In this experiment, only the outside surface of the graft was considered, as the inside surface is deemed unreliable due to artifacts invoked by the metal pin, and a union is defined as evidence of callus within a distance of 50 μm of the graft.

In autografts, the callus forms a union with the graft, as can be seen in Figure 6.6(a). In some other conditions, the callus regularly forms all around the graft, but remains at a distance, never forming a union. In Figure 6.6(b), this distance is indicated with yellow distance marks. To discriminate between this type of callus and the total absence of a callus, we introduce the coverage ratio. The coverage ratio defines the percentage of the graft that is covered with callus. A graft surface voxel is considered covered if callus is encountered along the surface normal. Averages and standard deviations across all the slices are computed for union and coverage ratios to obtain values representative for the entire graft.

Global parameters typically computed over the entire structure are the mineralised callus volume and the mineralised graft volume [70]. To get a better idea of the spatial distribution of mineralised voxels, the total volumes

encompassed by callus and graft are computed as well.

Vasculature quantification

We use a post reconstruction approach to combine the two datasets and to obtain a tissue decomposition. We reconstructed both datasets with the projection completion technique. The mean intensities for bone and soft tissue were determined in the two reconstructions and the intensities of the low energy reconstruction were linearly transformed to match those of the high energy reconstruction. After smoothing and subtraction of the low from the high energy reconstruction, the matched bone and soft tissue voxels have very small intensities, while voxels containing contrast agent have higher intensities due to the attenuation jump. The resulting vasculature image is segmented with hysteresis thresholding and subjected to measurements of average thickness and vessel number in a cylindrical volume of interest around the graft. The entire μCT image processing and visualisation is performed in custom made software.

The vasculature is evaluated on the histological sections by delineating the vessels in a similar region around the graft on 2 sections of each animal and measuring the relative area occupied by the vessels.

6.4.3 Results

A representative visualisation of callus formation 4 weeks post-operation can be seen in Figure 6.7. The autograft is entirely covered by callus, while the allograft callus is limited to regions near the host bone.

The quantitative parameters in Figure 6.8 confirm this observation. Allografts have significantly smaller callus volumes, and significantly lower union and coverage ratios.

Figure 6.9 illustrates that the reduced callus formation in allografts is accompanied by a reduction in blood vessels. Indeed, allografts are surrounded by significantly less vessels, and the remaining blood vessels are on average significantly thinner (Figure 6.10). These findings could be confirmed by immunohistochemistry (Figure 6.9(c)-(d)) and histomorphometry (Figure 6.10(c)).

(a) Autograft (b) Allograft

Figure 6.7: Visualisation of representative autograft and allograft callus formation. The graft is coloured grey, the host bone and callus brown.

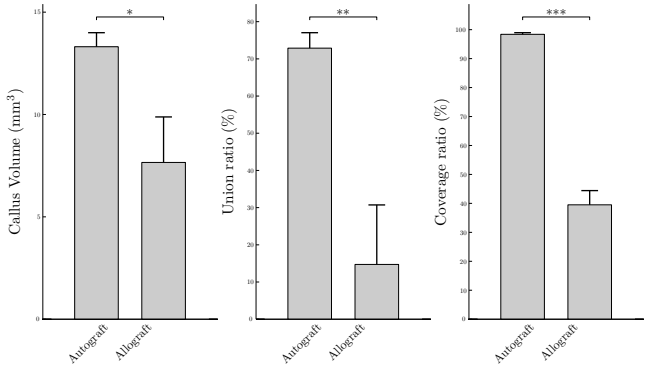

Figure 6.8: Quantitative parameters on bone healing of autografts and allografts (n=3). The error bars represent the standard deviation. * $p \leq 0.05$; ** $p \leq 0.01$; *** $p \leq 0.001$.

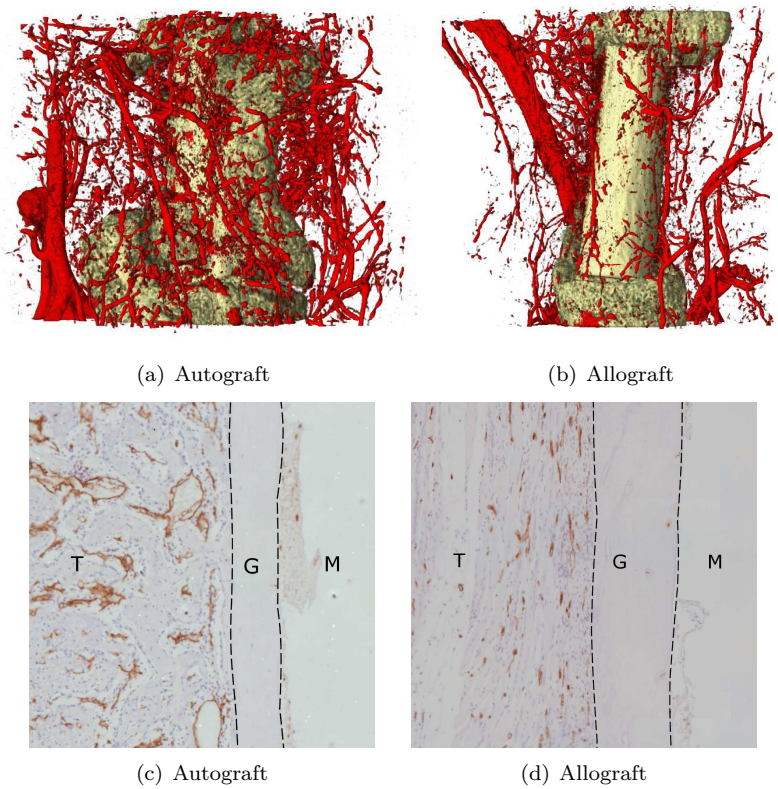

(a) Autograft (b) Allograft

(c) Autograft (d) Allograft

Figure 6.9: Visualisation of representative autograft and allograft vasculature with both μCT (top) and histology (bottom). In the histology images, labels indicate the soft tissue (T), graft bone (G) and bone marrow (M).

6.4.4 Discussion

The presented bone grafting experiment illustrates the complementary information obtained by analysing the bone and vasculature. Segmentation, visualisation and quantification methods were developed specifically to compute characteristics of the callus and were combined into a useful software package. Additionally, a post reconstruction dual energy program was developed that allows visualisation and quantification of vasculature characteristics. Vascular network characteristics obtained from μCT and immunohistochemistry were found to correspond well.

The autograft and allograft models are two extreme conditions, as the autograft

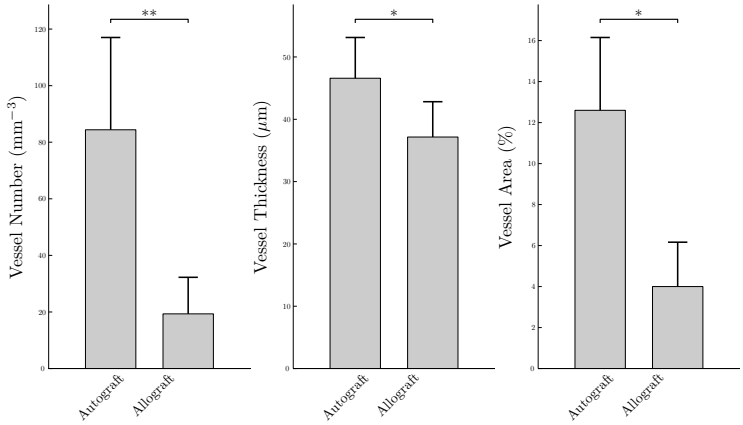

Figure 6.10: Quantification of the blood vessel network. Vessel number and vessel thickness are obtained from μCT images (n=6). Vessel area is computed on histological images (n=3). The error bars represent the standard deviation. * $p \leq 0.05$; ** $p \leq 0.01$.

contains an ideal composition of cells and growth factors while the allograft is devoid of any cells. Seeding the allografts with different combinations of cells and growth factors yields less extreme callus and vasculature characteristics, which the developed methods have been able to detect [139, 137, 136, 138]. Quantification and visualisation of callus and vasculature is highly valuable considering that certain growth factors are expected to influence bone and vasculature. The presented results give an indication of the relevance of the methods, and the 3D visualisations facilitate interpretation of the results. Screening of different combinatory therapies will be facilitated using the developed methods.

6.5 Discussion

This chapter has provided examples of applications of the methods developed in this thesis. In realistic experimental conditions, the proposed acquisition protocols and reconstruction and segmentation techniques yield images of sufficient quality to visualise and quantify bone and vasculature characteristics of interest. Visualisation and quantification software was created that allows researchers to obtain valuable insights and answers to their research questions. These applications indicate that the conducted research is relevant to biological research questions, and that it succeeds in imaging, visualising and quantifying bone and vasculature.

The provided applications can be considered validation experiments, the disease models are well known and outcomes expected. We are not the principal investigators of studies with more animals, innovative therapeutic conditions or staggering results, and those experiments and results do not belong in this thesis. We believe that the discussed examples do indicate the applicability and relevance of the conducted research.

We have developed and distributed numerous programs that enable researchers to analyse their own images. This approach raises concerns about the validity of possible quantified experimental outcomes. Restricting input images to satisfy rigourous constraints under which proper functioning can be guaranteed is a possible approach, but would be tedious and require a lot of programs as no experimental conditions are the same. Instead, we opt for a generic program that involves the user and informs him or her about each processing step. For this reason, all visualisation and quantification software was developed in MeVisLab, a development environment for medical image processing and visualisation which provides excellent support for interactive visualisation.

In the developed programs, every data processing step that requires manual interaction, such as selecting a representative volume of interest, segmenting some structure or registering images, is visible to the user in an interactive viewer. Benefits for the user are the continuous visual validation, awareness about all processing steps and possible errors, and the development of a good understanding of the data. The continuous visualisation does however require additional memory and computation power, slowing processing of large datasets down. As final output the quantitative measures are computed, and interactive 3D renderings are available to make figures and verify congruence with the quantitative results. We believe that this approach allows the user to convince himself of the validity of the obtained results, or to contact us in case of doubt.

6.6 Conclusion

Visualisation and quantification software is essential to interpret data and extract information from images. In this chapter, we have shown that the proposed imaging algorithms combined with visualisation and quantification software can detect bone and vasculature characteristics in experimental settings. This indicates that the conducted research is relevant to biological research questions, and that the intended aims of imaging, visualising and quantifying bone and vasculature have been met.

Chapter 7

General conclusion

μCT systems that image the internal 3D structure of small objects have become the preferred method to study bone mass and architecture in mice. In this thesis, dedicated μCT image acquisition, reconstruction, visualisation and quantification tools essential to solving specific bone research questions are developed.

7.1 Main contributions

As X-rays are ionising radiation, the effect of taking sequential μCT scans of mouse hindlimbs on living tissue was investigated. The relationship between administered dose and image quality was reviewed, and imaging protocols were designed with this trade-off in mind. The protocols were designed for three sequential scans separated by a 2-week interval, a typical setup for bone pathology studies. Possible tissue damage caused by these protocols was investigated on young and old mice, and on cell differentiation as well as macroscopical bone characteristics. The development of these protocols allows the execution of follow-up studies without significant side effects of X-ray exposure.

Limiting the dose inevitably reduces the image quality, hampering accurate segmentation to quantify bone structure. Threshold-based segmentation methods were reviewed and their limited ability to cope with image blurring was illustrated. The physical blurring processes occurring during measurement defy the assumptions in analytical reconstruction algorithms, but can be

modelled in iterative reconstruction algorithms, which are commonplace in nuclear medicine for PET and SPECT imaging. Using the MAP framework allowed us to incorporate a specially accommodated version of information theoretic priors and restrict the number of grey values in the reconstruction, at the cost of significantly longer computation times. The method was validated on young and old mouse hindlimbs scanned with the proposed in vivo imaging protocols, and performed better than the threshold-based segmentation methods in quantifying morphological parameters. Conversely, it was shown that similar quantification errors can be obtained from projection data with angular samples, corresponding to less dose.

To visualise the vascular system with CT, its attenuation properties have to be adjusted by injecting a contrast agent, typically based on iodine, barium or lead. Due to the high variability in the attenuation of the injected contrast agent, the contrast can not easily be discriminated from bone. The vascular corrosion casting technique acquires a μCT scan before and after decalcification of the bone, which takes weeks and introduces shrinkage artifacts. Alternatively, the energy dependence of the attenuation coefficient can be exploited, more precisely the K-edge of the contrast agent. Because post-reconstruction dual energy algorithms are very sensitive to noise, we developed a novel iterative dual energy algorithm with much better noise properties. The method differs from medical dual energy algorithms, because the K-edge of contrast agents lies within the μCT imaging energy range but out of the medical CT imaging energy range. The proposed algorithm is shown to have improved noise properties, enabling shorter scan times and eliminating movement caused by heating of the sample during long scans.

The developed reconstruction algorithms achieve higher quality reconstruction images, but this is no end point for the bone researcher. Typically, characteristics of mice with different genetic profiles, certain bone diseases, or receiving bone therapeutic strategies are compared. Increased image quality yields improved detectability of the characteristics of interest, but the features need to be extracted from the image by quantifying representative parameters. First, the validity of bone imaging with μCT is verified by comparing it with histology. Next, the vasculature tree is analysed in terms of vessel volume, vessel thickness and branching. Finally, callus formation of different graft models is compared and new measures are developed. These examples of tailored solutions to specific questions illustrate the relevance of the conducted research.

It should be emphasised that this thesis is the product of applied research. Investigations are motivated by challenges met by bone researchers. The objective of this work lies in finding solutions for these challenges. For some questions, such as bone tumour characterisation or vessel network

interpretation with graphs, literature provided satisfying solutions and these were implemented. For other problems, such as segmenting low dose μCT images, existing approaches yielded unconvincing results, and we resorted to relevant algorithms of other research domains. In studying and optimising these methods, the focus was on the validation with respect to small animal bone imaging, not on rigourous mathematical proofs or derivations. This approach accentuates the added value of μCT imaging by providing the tools and experience to detect and evaluate the characteristics of their interest.

7.2 Future perspectives

Overall, μCT has proven to be a valuable imaging modality in bone and other preclinical research. The key feature provided by μCT imaging is the measurement of the 3D internal sample structure at high resolution. The non-destructiveness of the technique, combined with limited sample preparation and relatively straightforward scanning procedures make it an easily accessible technique. In the preclinical bone field, μCT imaging enables fast analyses of bone phenotype, and perfusion with contrast agents enables imaging of the vascular network and its relation to mineralised bone. In vivo follow up of bone architecture in the same animal provides insight into dynamic tissue processes. μCT imaging serves as a complementary technique to histology, which can detect a wider variety of tissues at higher resolution, albeit in 2D.

Recent advances indicate that attenuation-based X-ray imaging can be expected to be further refined in the near future. The soon available photon counting detectors will allow spectral imaging, enhancing material discrimination. In particular for bone imaging, recent contrast enhanced nanoCT imaging allows the detection of cartilage [68], although cartilage segmentation appears challenging. Acquisition protocols and reconstruction algorithms will have to be adapted to make full use of these opportunities. The additional spectral information provided by photon counting detectors will enable reconstruction algorithms to reduce the amount of assumptions made and yield more generally applicable algorithms.

Recent increases in computation power have revitalised the iterative CT reconstruction domain. The major drawback of increased computation time can be reduced by graphical card implementations of projector and backprojector, which has not yet been incorporated in our algorithms. The enhanced image quality provided by such techniques enables increased image quality or associated dose reduction, which would benefit clinical CT applications as well. The developed algorithms for μCT are straightforwardly applicable to clinical

CT, provided that the scanner geometry is known. A trial study has been set up in collaboration with clinical partners to investigate achievable amounts of CT dose reduction. The clinic is a more constrained environment than the preclinical research facility, requiring cooperation of the CT manufacturer to correctly model the preprocessing on the raw data.

The availability of μCT and nanoCT systems forces us to reflect about the scalability of CT imaging. Increasing resolution allows imaging ever finer structures, such as murine osteocyte lacunae, but yields massive datasets which are challenging to process even with today's high performance computers. Cutting the sample in pieces and scanning representative regions can reduce the amount of data substantially, but approaches the limits of sectioning techniques and destroys the sample. As this text has indicated my natural response is to turn towards the field of reconstruction, and I believe it could provide a solution with interior tomography algorithms that enable reconstructing images out of truncated data. An entirely different solution might be provided by compressed sensing, which states that an image, sparse in some kind of representation, can be recovered from relatively few measurements. Currently, it is economically favourable to produce large flat detector arrays that collect large datasets, but theoretically reconstructions could be made with considerable less projection measurements, provided that hardware developers can find an economically viable technique of producing incoherent sensors.

Developing advanced image quantification methods and finding predictors for bone remodelling would arguably have a larger impact on the bone community. The current quantification approaches leave much of the information content in the data untended. For example, evaluating dynamic changes in bone over time by comparing global morphometric indices disregards much of the available information in the obtained images. Registering successive bone images and comparing local characteristics extracts more information, but image processing can search actively for predictors of for example bone adaptation [150]. Similarly, quantifying vascular structures and bone separately provides useful information, but does not investigate the mutual influences these two exercise on each other. Providing requested quantification parameters could be supplemented with more integrated approaches such as building models around the many datasets that are continuously being acquired, similar to population databases that are being mined in neuroimaging. In such a holistic approach, image processing of μCT images could actively find clues that help unravel the elusive mechanisms of bone.

Bibliography

[1] Alexander J. M., Bab I., Fish S., Müller R., Uchiyama T., Gronowicz G., Nahounou M., Zhao Q., White D. W., Chorev M., Gazit D., and Rosenblatt M., "Human parathyroid hormone 1-34 reverses bone loss in ovariectomized mice," *Journal of Bone and Mineral Research*, vol. 16, no. 9, pp. 1665–1673, 2001.

[2] Alvarez R. E. and Macovski A., "Energy-selective reconstructions in X-ray computerised tomography," *Physics in Medicine & Biology*, vol. 21, no. 5, pp. 733–744, 1976.

[3] Barrett J. F. and Keat N., "Artifacts in CT: Recognition and avoidance," *Radiographics*, vol. 24, no. 6, pp. 1679–1691, 2004.

[4] Batenburg K. J. and Sijbers J., "DART: a fast heuristic algebraic reconstruction algorithm for discrete tomography," in *Proceedings of the IEEE International Conference on Image Processing*, vol. 4, pp. IV133–IV136, 2007.

[5] Batenburg K. J. and Sijbers J., "Adaptive thresholding of tomograms by projection distance minimization," *Pattern Recognition*, vol. 42, no. 10, pp. 2297–2305, 2009.

[6] Batenburg K. J. and Sijbers J., "Optimal threshold selection for tomogram segmentation by projection distance minimization," *IEEE Transactions on Medical Imaging*, vol. 28, no. 5, pp. 676–686, 2009.

[7] Berger M., Hubbell J., Seltzer S., Chang J., Coursey J., Sukumar R., Zucker D., and Olsen K., "XCOM: Photon cross sections database," National Institute of Standards and Technology, Tech. Rep., 1998.

[8] Bethesda M., "Tissue substitutes in radiation dosimetry and measurement," International Comission in Radiation Units and Measurements, Tech. Rep. 44, 1989.

[9] Bouxsein M. L., Boyd S. K., Christiansen B. A., Guldberg R. E., Jepsen K. J., and Muller R., "Guidelines for assessment of bone microstructure in rodents using micro-computed tomography," *Journal of Bone and Mineral Research*, vol. 25, no. 7, pp. 1468–1486, 2010.

[10] Boyd S. K., Moser S., Kuhn M., Klinck R. J., Krauze P. L., Muller R., and Gasser J. A., "Evaluation of three-dimensional image registration methodologies

for in vivo micro-computed tomography," *Annals of Biomedical Engineering*, vol. 34, no. 10, pp. 1587–1599, 2006.

[11] Brouwers J. E., van Rietbergen B., and Huiskes R., "No effects of in vivo micro-CT radiation on structural parameters and bone marrow cells in proximal tibia of wistar rats detected after eight weekly scans," *Journal of Orthopaedic Research*, vol. 25, no. 10, pp. 1325–1332, 2007.

[12] Buzug T., *Springer Handbook of Medical Technology*. Springer Berlin Heidelberg, 2012, ch. Computed Tomography, pp. 311–342.

[13] Cai Q.-Y., Kim S., Choi K., Kim S., Byun S., Kim K., Park S., Juhng S., and Yoon K.-H., "Colloidal gold nanoparticles as a blood-pool contrast agent for X-ray computed tomography in mice," *Investigative Radiology*, vol. 42, pp. 797–806, 2007.

[14] Cancedda R., Giannoni P., and Mastrogiacomo M., "A tissue engineering approach to bone repair in large animal models and in clinical practice," *Biomaterials*, vol. 28, no. 29, pp. 4240–4250, 2007.

[15] Candès E. J., Romberg J., and Tao T., "Robust uncertainty principles: Exact signal reconstruction from highly incomplete frequency information," *IEEE Transactions on Information Theory*, vol. 52, no. 2, pp. 489–509, 2006.

[16] Canny J., "A computational approach to edge detection," *IEEE Transactions on Pattern Analysis and Machine Intelligence*, no. 6, pp. 679–698, 1986.

[17] Carano R. A. D. and Filvaroff E. H., "Angiogenesis and bone repair," *Drug Discovery Today*, vol. 8, no. 21, pp. 980–989, 2003.

[18] Colijn A., Zbijewski W., Sasov A., and Beekman F., "Experimental validation of a rapid Monte Carlo based micro-CT simulator," *Physics in Medicine & Biology*, vol. 49, no. 18, pp. 4321–4333, 2004.

[19] Cooper D., Turinsky A., Sensen C., and Hallgrimsson B., "Effect of voxel size on 3D micro-CT analysis of cortical bone porosity," *Calcified Tissue International*, vol. 80, no. 3, pp. 211–219, 2007.

[20] Daci E., "The role of the plasminogen system in bone resorption in vitro," *Journal of Bone and Mineral Research*, vol. 14, no. 6, pp. 946–952, 1999.

[21] Dare A., Hachisu R., Yamaguchi A., Yokose S., Yoshiki S., and Okano T., "Effects of ionizing radiation on proliferation and differentiation of osteoblast-like cells," *Journal of Dental Research*, vol. 76, no. 2, pp. 658–664, 1997.

[22] De Man B. and Fessler J., *Biomedical Mathematics: Promising Directions in Imaging, Therapy Planning and Inverse Problems*. Medical Physics Publishing, 2010, ch. Statistical iterative reconstruction for X-ray computed tomography, pp. 113–140.

[23] De Man B., Nuyts J., Dupont P., Marchal G., and Suetens P., "An iterative maximum-likelihood polychromatic algorithm for CT," *IEEE Transactions on Medical Imaging*, vol. 20, no. 10, pp. 999–1008, 2001.

[24] De Man B., "Iterative reconstruction for reduction of metal artifacts in computed tomography," Ph.D. dissertation, KULeuven, 2001.

[25] De Man B. and Basu S., "Distance-driven projection and backprojection in three dimensions," *Physics in Medicine & Biology*, vol. 49, no. 11, pp. 2463–2475, 2004.

[26] Dempster D. W., "Anatomy and functions of the adult skeleton," in *Primer on the Metabolic Bone Diseases and Disorders of Mineral Metabolism*, 6th ed. John Wiley & Sons Inc., 2006, pp. 7–11.

[27] Dempster D. W., Compston J. E., Drezner M. K., Glorieux F. H., Kanis J. A., Malluche H., Meunier P. J., Ott S. M., Recker R. R., and Parfitt A. M., "Standardized nomenclature, symbols, and units for bone histomorphometry: A 2012 update of the report of the ASBMR Histomorphometry Nomenclature Committee," *Journal of Bone and Mineral Research*, vol. 28, no. 1, pp. 2–17, 2013.

[28] Depypere M., Nuyts J., Laperre K., Carmeliet G., Maes F., and Suetens P., "The minimal entropy prior for simultaneous reconstruction and segmentation of in vivo microCT trabecular bone images," in *Proceedings IEEE International Symposium on Biomedical Imaging*, pp. 586–589, 2009.

[29] Depypere M., Nuyts J., van Gastel N., Carmeliet G., Maes F., and Suetens P., "An iterative dual energy CT reconstruction method for a K-edge contrast material," in *Proceedings of SPIE Medical Imaging: Physics of Medical Imaging*, vol. 7961, pp. 79 610M1–79 610M7, 2011.

[30] Donoho D. L., "Compressed sensing," *IEEE Transactions on Information Theory*, vol. 52, no. 4, pp. 1289–1306, 2006.

[31] Dudziak M. E., Saadeh P. B., Mehrara B. J., Steinbrech D. S., Greenwald J. A., Gittes G. K., and Longaker M. T., "The effects of ionizing radiation on osteoblast-like cells in vitro," *Plastic and Reconstructive Surgery*, vol. 106, no. 5, pp. 1049–1061, 2000.

[32] Elbakri I. A. and Fessler J., "Efficient and accurate likelihood for iterative image reconstruction in X-ray computed tomography," in *Proceedings of SPIE Medical Imaging: Image Processing*, vol. 5032, pp. 1839–1850, 2003.

[33] Elefteriou F. and Yang X., "Genetic mouse models for bone studies - strengths and limitations," *Bone*, vol. 49, no. 6, pp. 1242–1254, 2011.

[34] Erben R. G., Eberle J., Stahr K., and Goldberg M., "Androgen deficiency induces high turnover osteopenia in aged male rats: a sequential histomorphometric study," *Journal of Bone and Mineral Research*, vol. 15, no. 6, pp. 1085–1098, 2000.

[35] Feldkamp L. A., Davis L. C., and Kress J. W., "Practical cone-beam algorithm," *Journal of the Optical Society of America A*, vol. 1, no. 6, pp. 612–619, 1984.

[36] Fessler J. (2001). [Online]. Available: http://web.eecs.umich.edu/~fessler/misc/opinion/opinion,2001.html

[37] Fessler J. A. and Rogers W. L., "Spatial resolution properties of penalized-likelihood image reconstruction: space-invariant tomographs," *IEEE Transactions on Image Processing*, vol. 5, no. 9, pp. 1346–1358, 1996.

[38] Ford N. L., Thornton M. M., and Holdsworth D. W., "Fundamental image quality limits for microcomputed tomography in small animals," *Medical Physics*, vol. 30, no. 11, pp. 2869–2877, 2003.

[39] Gal T. J., Munoz-Antonia T., Muro-Cacho C. A., and Klotch D. W., "Radiation effects on osteoblasts in vitro: a potential role in osteoradionecrosis," *Archives of Otolaryngology - Head & Neck Surgery*, vol. 126, no. 9, pp. 1124–1128, 2000.

[40] Giannoudis P. V., Dinopoulos H., and Tsiridis E., "Bone substitutes: an update," *Injury*, vol. 36, no. 3, pp. S20–S27, 2005.

[41] Glover G. H. and Pelc N. J., "An algorithm for the reduction of metal clip artifacts in CT reconstructions," *Medical Physics*, vol. 8, pp. 799–807, 1981.

[42] Goldman L. W., "Principles of CT: radiation dose and image quality," *Journal of Nuclear Medicine Technology*, vol. 35, no. 4, pp. 213–225, 2007.

[43] Goldner J., "A modification of the masson trichrome technique for routine laboratory purposes," *The American Journal of Pathology*, vol. 14, pp. 237–243, 1938.

[44] Grande T. and Bueren J. A., "Analysis of hematopoiesis in mice irradiated with 500 mGy of X rays at different stages of development," *Radiation Research*, vol. 143, no. 3, pp. 327–333, 1995.

[45] Granton P. V., Pollmann S. I., Ford N. L., Drangova M., and Holdsworth D. W., "Implementation of dual- and triple-energy cone-beam micro-CT for postreconstruction material decomposition," *Medical Physics*, vol. 35, no. 11, pp. 5030–5042, 2008.

[46] Hammersberg P., Stenström M., Hedtjärn H., and Mångård M., "Measurements of absolute energy spectra for an industrial micro focal X-ray source under working conditions using a Compton scattering spectrometer," *Journal of X-ray science and Technology*, vol. 8, no. 1, pp. 5–18, 1998.

[47] Heismann B. J., "Noise transfer analysis of base material decomposition methods," in *Proceedings of SPIE Medical Imaging: Physics of Medical Imaging*, vol. 6510, pp. 6 510 111–6 510 116, 2007.

[48] Hellingman A., Bastiaansen A., de Vries M., Seghers L., Lijkwan M., Löwik C., Hamming J., and Quax P., "Variations in surgical procedures for hind limb ischaemia mouse models result in differences in collateral formation," *European Journal of Vascular and Endovascular Surgery*, vol. 40, no. 6, pp. 796–803, 2010.

[49] Herman G. T. and Kuba A., "Discrete tomography in medical imaging," *Proceedings of the IEEE*, vol. 91, no. 10, pp. 1612–1626, 2003.

[50] Hildebrand T. and Ruegsegger P., "A new method for the model-independent assessment of thickness in three-dimensional images," *Journal of Microscopy*, vol. 185, no. 1, pp. 67–75, 1997.

[51] Hsiao I.-T., Rangarajan A., and Gindi G., "Joint-MAP bayesian tomographic reconstruction with a gamma-mixture prior," *IEEE Transactions on Image Processing*, vol. 11, no. 12, pp. 1466–1477, 2002.

[52] Hsieh J., *Computed tomography: principles, design, artifacts, and recent advances*. SPIE - The International Society for Optical Engineering, 2003.

[53] Huang W., Yang Y., Sun Z., and Zeng X., "Early radiation-induced bone marrow injury: serial MR imaging during initial 4 weeks after irradiation," *Academic Radiology*, vol. 16, no. 6, pp. 733–738, 2009.

[54] Hubbell J., "Photon mass attenuation and energy-absorption coefficients," *The International Journal of Applied Radiation and Isotopes*, vol. 33, no. 11, pp. 1269–1290, 1982.

[55] Hubbell J. and Seltzer S., "Tables of X-ray mass attenuation coefficients and mass energy-absorption coefficients 1 keV to 20 MeV for elements Z = 1 to 92 and 48 additional substances of dosimetric interest," National Institute of Standards and Technology, Tech. Rep., 1995.

[56] Hudson H. M. and Larkin R. S., "Accelerated image reconstruction using ordered subsets of projection data," *IEEE Transactions on Medical Imaging*, vol. 13, no. 4, pp. 601–609, 1994.

[57] Hutchinson F., "The molecular basis for radiation effects on cells," *Cancer Research*, vol. 26, no. 9, pp. 2045–2052, 1966.

[58] Iliakis G., Wang Y., Guan J., and Wang H., "DNA damage checkpoint control in cells exposed to ionizing radiation," *Oncogene*, vol. 22, no. 37, pp. 5834–5847, 2003.

[59] Jee W. S. and Yao W., "Overview: animal models of osteopenia and osteoporosis," *Journal of Musculoskeletal & Neuronal Interactions*, vol. 1, no. 3, pp. 193–207, 2001.

[60] Jia X., Lou Y., Li R., Song W. Y., and Jiang S. B., "GPU-based fast cone beam CT reconstruction from undersampled and noisy projection data via total variation," *Medical Physics*, vol. 37, no. 4, pp. 1757–1760, 2010.

[61] Jiang Y., Zhao J., White D. L., and Genant H. K., "Micro CT and micro MR imaging of 3D architecture of animal skeleton," *Journal of Musculoskeletal & Neuronal Interactions*, vol. 1, no. 1, pp. 45–51, 2000.

[62] Johnson T., Krauß B., Sedlmair M., Grasruck M., Bruder H., Morhard D., Fink C., Weckbach S., Lenhard M., Schmidt B., Flohr T., Reiser M., and Becker C., "Material differentiation by dual energy CT: initial experience," *European Radiology*, vol. 17, no. 6, pp. 1510–1517, 2007.

[63] Judex S., Chung H., Torab A., Xie L., Rubin C., Donahue L., and Xu S., "Micro-CT induced radiation does not exacerbate disuse related bone loss," in *Transactions of the 51st annual meeting of the ORS*, 2005.

[64] Judy P. F., "The line spread function and modulation transfer function of a computed tomographic scanner," *Medical physics*, vol. 3, no. 4, pp. 233–236, 1976.

[65] Kalender W., Klotz E., and Kostaridou L., "An algorithm for noise suppression in dual energy CT material density images," *IEEE Transactions on Medical Imaging*, vol. 7, no. 3, pp. 218–224, Sep 1988.

[66] Kalu D. N., "The ovariectomized rat model of postmenopausal bone loss," *Bone and Mineral*, vol. 15, no. 3, pp. 175–191, 1991.

[67] Kelcz F., Joseph P. M., and Hilal S. K., "Noise considerations in dual energy CT scanning," *Medical Physics*, vol. 6, no. 5, pp. 418–425, 1979.

[68] Kerckhofs G., Sainz J., Wevers M., Van de Putte T., and Schrooten J., "Contrast-enhanced nanofocus computed tomography images the cartilage subtissue architecture in three dimensions," *European Cells and Materials*, vol. 25, pp. 179–189, 2013.

[69] Klinck R. J., Campbell G. M., and Boyd S. K., "Radiation effects on bone architecture in mice and rats resulting from in vivo micro-computed tomography scanning," *Medical Engineering & Physics*, vol. 30, no. 7, pp. 888–895, 2008.

[70] Koefoed M., Ito H., Gromov K., Reynolds D. G., Awad H. A., Rubery P. T., Ulrich-Vinther M., Soballe K., Guldberg R. E., Lin A. S., O'Keefe R. J., Zhang X., and Schwarz E. M., "Biological effects of rAAV-caAlk2 coating on structural allograft healing," *Molecular Therapy*, vol. 12, no. 2, pp. 212–218, 2005.

[71] Kopp H. G., Avecilla S. T., Hooper A. T., and Rafii S., "The bone marrow vascular niche: home of HSC differentiation and mobilization," *Physiology*, vol. 20, pp. 349–356, 2005.

[72] Kristensen H. B., Andersen T. L., Marcussen N., Rolighed L., and Delaisse J.-M., "Increased presence of capillaries next to remodeling sites in adult human cancellous bone," *Journal of Bone and Mineral Research*, vol. 28, no. 3, pp. 574–585, 2013.

[73] Kuhn J. L., Goldstein S. A., Feldkamp L. A., Goulet R. W., and Jesion G., "Evaluation of a microcomputed tomography system to study trabecular bone structure," *Journal of Orthopaedic Research*, vol. 8, no. 6, pp. 833–842, 1990.

[74] Lange K. and Carson R., "EM reconstruction algorithms for emission and transmission tomography." *Journal of Computer Assisted Tomography*, vol. 8, no. 2, pp. 306–316, 1984.

[75] Laperre K., Depypere M., Van Gastel N., Torrekens S., Moermans K., Bogaerts R., Maes F., and Carmeliet G., "Development of micro-CT protocols for in vivo follow-up of mouse bone architecture without major radiation side effects," *Bone*, vol. 49, no. 4, pp. 613–622, 2011.

[76] Lehmann L. and Alvarez R., *Energy-selective radiography: A review*, Kareiakes J., Thomas S., and Orton C., Eds. New York: Plenum, 1986.

[77] Li M., Jee W. S., Ke H. Z., Tang L. Y., Ma Y. F., Liang X. G., and Setterberg R. B., "Prostaglandin E2 administration prevents bone loss induced by orchidectomy in rats," *Journal of Bone and Mineral Research*, vol. 10, no. 1, pp. 66–73, 1995.

[78] Li W., Wang G., Cui J., Xue L., and Cai L., "Low-dose radiation (LDR) induces hematopoietic hormesis: LDR-induced mobilization of hematopoietic progenitor cells into peripheral blood circulation," *Experimental Hematology*, vol. 32, no. 11, pp. 1088–1096, 2004.

[79] Lieben L., Benn B. S., Ajibade D., Stockmans I., Moermans K., Hediger M. A., Peng J. B., Christakos S., Bouillon R., and Carmeliet G., "Trpv6 mediates intestinal calcium absorption during calcium restriction and contributes to bone homeostasis," *Bone*, vol. 47, no. 2, pp. 301–308, 2010.

[80] Liu X., Yu L., Primak A. N., and McCollough C. H., "Quantitative imaging of element composition and mass fraction using dual-energy CT: Three-material decomposition," *Medical Physics*, vol. 36, no. 5, pp. 1602–1609, 2009.

[81] Long Y. and Fessler J. A., "Multi-material decomposition using statistical image reconstruction in X-ray CT," in *Proc. 2nd International Meeting on image formation in X-ray CT*, pp. 413–416, 2012.

[82] Maes C., Carmeliet P., Moermans K., Stockmans I., Smets N., Collen D., Bouillon R., and Carmeliet G., "Impaired angiogenesis and endochondral bone formation in mice lacking the vascular endothelial growth factor isoforms $VEGF_{164}$ and $VEGF_{188}$," *Mechanisms of Development*, vol. 111, no. 1, pp. 61–73, 2002.

[83] Maes C., Coenegrachts L., Stockmans I., Daci E., Luttun A., Petryk A., Gopalakrishnan R., Moermans K., Smets N., Verfaillie C. M., Carmeliet P., Bouillon R., and Carmeliet G., "Placental growth factor mediates mesenchymal cell development, cartilage turnover, and bone remodeling during fracture repair," *Journal of Clinical Investigation*, vol. 116, no. 5, pp. 1230–1242, 2006.

[84] Maes C., Stockmans I., Moermans K., Van Looveren R., Smets N., Carmeliet P., Bouillon R., and Carmeliet G., "Soluble VEGF isoforms are essential for establishing epiphyseal vascularization and regulating chondrocyte development and survival," *Journal of Clinical Investigation*, vol. 113, no. 2, pp. 188–199, 2004.

[85] Maes C. and Carmeliet G., "Vascular and nonvascular roles of VEGF in bone development," in *VEGF in Development*. Springer New York, 2008, pp. 79–90.

[86] Maes F., Collignon A., Vandermeulen D., Marchal G., and Suetens P., "Multimodality image registration by maximization of mutual information," *IEEE Transactions on Medical Imaging*, vol. 16, no. 2, pp. 187–98, 1997.

[87] Marieb E., *Essentials of Human Anatomy & Physiology*. Pearson/Benjamin Cummings, 2009.

[88] Marxen M., Thornton M. M., Chiarot C. B., Klement G., Koprivnikar J., Sled J. G., and Henkelman R. M., "MicroCT scanner performance and considerations for vascular specimen imaging," *Medical Physics*, vol. 31, no. 2, pp. 305–313, 2004.

[89] Masuyama R., Stockmans I., Torrekens S., Van Looveren R., Maes C., Carmeliet P., Bouillon R., and Carmeliet G., "Vitamin D receptor in chondrocytes promotes osteoclastogenesis and regulates FGF23 production in osteoblasts," *Journal of Clinical Investigation*, vol. 116, no. 12, pp. 3150–3159, 2006.

[90] Matsumura S., Jikko A., Hiranuma H., Deguchi A., and Fuchihata H., "Effect of X-ray irradiation on proliferation and differentiation of osteoblast," *Calcified Tissue International*, vol. 59, no. 4, pp. 307–308, 1996.

[91] Meloan S. N. and Puchtler H., "Chemical mechanisms of staining methods: Von Kossa's technique: What von Kossa really wrote and a modified reaction for selective demonstration of inorganic phosphates," *Journal of Histotechnology*, vol. 8, no. 1, pp. 11–13, 1985.

[92] Mendonca P. R. S., Bhotika R., Maddah M., Thomsen B., Dutta S., Licato P. E., and Joshi M. C., "Multi-material decomposition of spectral CT images," in *Proceedings of SPIE Medical Imaging: Physics of Medical Imaging*, vol. 7622, pp. 76 221W1–76 221W9, 2010.

[93] Minkin C., "Bone acid phosphatase: Tartrate-resistant acid phosphatase as a marker of osteoclast function," *Calcified Tissue International*, vol. 34, pp. 285–290, 1982.

[94] Mitchell M. J. and Logan P. M., "Radiation-induced changes in bone," *Radiographics*, vol. 18, no. 5, pp. 1125–1136, 1998.

[95] Morgan E. F. and Einhorn T. A., "Biomechanics of fracture healing," in *Primer on the Metabolic Bone Diseases and Disorders of Mineral Metabolism*, 6th ed. John Wiley & Sons Inc., 2009, pp. 65–69.

[96] Mouse Genome Sequencing Consortium, "Initial sequencing and comparative analysis of the mouse genome," *Nature*, vol. 420, no. 6915, pp. 520–562, 2002.

[97] Müller R., Van Campenhout H., Van Damme B., Van Der Perre G., Dequeker J., Hildebrand T., and Rüegsegger P., "Morphometric analysis of human bone biopsies: a quantitative structural comparison of histological sections and micro-computed tomography." *Bone*, vol. 23, no. 1, pp. 59–66, 1998.

[98] Nishiyama K. K., Campbell G. M., Klinck R. J., and Boyd S. K., "Reproducibility of bone micro-architecture measurements in rodents by in vivo micro-computed tomography is maximized with three-dimensional image registration," *Bone*, vol. 46, no. 1, pp. 155–161, 2009.

[99] Nuyts J., "The use of mutual information and joint entropy for anatomical priors in emission tomography," in *IEEE Nuclear Science Symposium Conference Record*, vol. 6, pp. 4149–4154, 2007.

[100] Nuyts J., Beque D., Dupont P., and Mortelmans L., "A concave prior penalizing relative differences for maximum-a-posteriori reconstruction in emission tomography," *IEEE Transactions on Nuclear Science*, vol. 49, no. 1, pp. 56–60, 2002.

[101] Nuyts J., De Man B., Dupont P., Defrise M., Suetens P., and Mortelmans L., "Iterative reconstruction for helical CT: a simulation study," *Physics in Medicine & Biology*, vol. 43, no. 4, pp. 729–737, 1998.

[102] Nuyts J., Bal G., Kehren F., Fenchel M., Michel C., and Watson C., "Completion of a truncated attenuation image from the attenuated PET emission data," *IEEE Transactions on Medical Imaging*, vol. 32, no. 2, pp. 237–246, 2013.

[103] Olive P. L., Banath J. P., and Durand R. E., "Heterogeneity in radiation-induced DNA damage and repair in tumor and normal cells measured using the "comet" assay," *Radiation Research*, vol. 122, no. 1, pp. 86–94, 1990.

[104] Otsu N., "A threshold selection method from gray-level histograms," *Automatica*, vol. 11, no. 285-296, pp. 23–27, 1975.

[105] Parfitt A. M., Drezner M. K., Glorieux F. H., Kanis J. A., Malluche H., Meunier P. J., Ott S. M., and Recker R. R., "Bone histomorphometry: standardization of nomenclature, symbols, and units. Report of the ASBMR Histomorphometry Nomenclature Committee," *Journal of Bone and Mineral Research*, vol. 2, no. 6, pp. 595–610, 1987.

[106] Parfitt A., Mathews C., Villanueva A., Kleerekoper M., Frame B., and Rao D., "Relationships between surface, volume, and thickness of iliac trabecular bone in aging and in osteoporosis. implications for the microanatomic and cellular mechanisms of bone loss," *Journal of Clinical Investigation*, vol. 72, no. 4, pp. 1396–1409, 1983.

[107] Park K.-K., Pavlicek W., Boltz T., Paden R., Hara A., and Akay M., "Image-based dual energy CT improvements using Gram-Schmidt method," in *Proceedings of SPIE Medical Imaging: Physics of Medical Imaging*, vol. 7258, pp. 72 583S1–72 583S9, 2009.

[108] Primak A. N., Ramirez Giraldo J. C., Liu X., Yu L., and McCollough C. H., "Improved dual-energy material discrimination for dual-source CT by means of additional spectral filtration," *Medical Physics*, vol. 36, no. 4, pp. 1359–1369, 2009.

[109] Reid I. R., "Menopause," in *Primer on the Metabolic Bone Diseases and Disorders of Mineral Metabolism.* John Wiley & Sons Inc., 2009, pp. 95–97.

[110] Revell P., "Histomorphometry of bone," *Journal of Clinical Pathology*, vol. 36, no. 12, pp. 1323–1331, 1983.

[111] Reynolds D. G., Shaikh S., Papuga M. O., Lerner A. L., O'Keefe R. J., Schwarz E. M., and Awad H. A., "μCT-based measurement of cortical bone graft-to-host union," *Journal of Bone and Mineral Research*, vol. 24, no. 5, pp. 899–907, 2008.

[112] Riederer S. J. and Mistretta C. A., "Selective iodine imaging using K-edge energies in computerized X-ray tomography," *Medical Physics*, vol. 4, no. 6, pp. 474–481, 1977.

[113] Ritman E. L., "Micro-computed tomography-current status and developments," *Annual Review of Biomedical Engineering*, vol. 6, no. 1, pp. 185–208, 2004.

[114] Ritman E. L., "Small-animal CT: its difference from, and impact on, clinical CT," *Nuclear Instruments and Methods in Physics Research Section A: Accelerators, Spectrometers, Detectors and Associated Equipment*, vol. 580, no. 2, pp. 968–970, 2007.

[115] Robey P. G. and Boskey A. L., "Extracellular matrix and biomineralization of bone," in *Primer on the Metabolic Bone Diseases and Disorders of Mineral Metabolism*, 6th ed. John Wiley & Sons Inc., 2006, pp. 12–19.

[116] Roessl E. and Proksa R., "K-edge imaging in X-ray computed tomography using multi-bin photon counting detectors," *Physics in Medicine & Biology*, vol. 52, no. 15, pp. 4679–4696, 2007.

[117] Rubin C. and Rubin J., "Biomechanics and mechanobiology of bone," in *Primer on the Metabolic Bone Diseases and Disorders of Mineral Metabolism*, 6th ed. John Wiley & Sons Inc., 2006, pp. 36–41.

[118] Samei E., Flynn M. J., and Reimann D. A., "A method for measuring the presampled MTF of digital radiographic systems using an edge test device," *Medical Physics*, vol. 25, pp. 102–113, 1998.

[119] Schambach S. J., Bag S., Schilling L., Groden C., and Brockmann M. A., "Application of micro-CT in small animal imaging," *Methods*, vol. 50, no. 1, pp. 2–13, 2010.

[120] Scheven B. A., Burger E. H., Kawilarang-de Haas E. W., Wassenaar A. M., and Nijweide P. J., "Effects of ionizing irradiation on formation and resorbing activity of osteoclasts in vitro," *Laboratory Investigation*, vol. 53, no. 1, pp. 72–79, 1985.

[121] Schneider P., Krucker T., Meyer E., Ulmann-Schuler A., Weber B., Stampanoni M., and Müller R., "Simultaneous 3D visualization and quantification of murine bone and bone vasculature using micro-computed tomography and vascular replica," *Microscopy Research and Technique*, vol. 72, no. 9, pp. 690–701, 2009.

[122] Seifert A. and Flynn M. J., "Resolving power of 3D X-ray microtomography systems," in *Proceedings of SPIE Medical Imaging: Physics of Medical Imaging*, vol. 4682, pp. 407–413, 2002.

[123] Selle D., Preim B., Schenk A., and Peitgen H.-O., "Analysis of vasculature for liver surgical planning," *IEEE Transactions on Medical Imaging*, vol. 21, no. 11, pp. 1344–1357, 2002.

[124] Sharma K. S., Seshadri S., Feser M., Wang G., McNulty I., Eyberger C., and Lai B., "Accurate resolution measurement for X-ray micro-CT systems," in *AIP Conference Proceedings*, vol. 1365, no. 1, pp. 337–340, 2011.

[125] Sidky E. Y. and Pan X., "Image reconstruction in circular cone-beam computed tomography by constrained, total-variation minimization," *Physics in Medicine & Biology*, vol. 53, no. 17, pp. 4777–4807, 2008.

[126] Somayajula S., Asma E., and Leahy R., "PET image reconstruction using anatomical information through mutual information based priors," in *IEEE Nuclear Science Symposium Conference Record*, vol. 5, pp. 2722–2726, 2005.

[127] Song S. and Lambert P. F., "Different responses of epidermal and hair follicular cells to radiation correlate with distinct patterns of p53 and p21 induction," *The American Journal of Pathology*, vol. 155, no. 4, pp. 1121–1127, 1999.

[128] Street J., Bao M., deGuzman L., Bunting S., Peale F. V., Ferrara N., Steinmetz H., Hoeffel J., Cleland J. L., Daugherty A., van Bruggen N., Redmond H. P., Carano R. A. D., and Filvaroff E. H., "Vascular endothelial growth factor stimulates bone repair by promoting angiogenesis and bone turnover," *Proceedings of the National Academy of Sciences*, vol. 99, no. 15, pp. 9656–9661, 2002.

[129] Suetens P., *Fundamentals of Medical Imaging*. Cambridge University Press, 2002.

[130] Sukovic P. and Clinthorne N., "Basis material decomposition using triple-energy X-ray computed tomography," in *Instrumentation and Measurement Technology Conference*, vol. 3, pp. 1615–1618, 1999.

[131] Sukovic P. and Clinthorne N., "Penalized weighted least-squares image reconstruction for dual energy X-ray transmission tomography," *IEEE Transactions on Medical Imaging*, vol. 19, no. 11, pp. 1075–1081, 2000.

[132] Tang J., Nett B. E., and Chen G.-H., "Performance comparison between total variation (TV)-based compressed sensing and statistical iterative reconstruction algorithms," *Physics in Medicine & Biology*, vol. 54, no. 19, pp. 5781–5804, 2009.

[133] Tang J., Tsui B., and Rahmim A., "Bayesian PET image reconstruction incorporating anato-functional joint entropy," in *Proceedings IEEE International Symposium on Biomedical Imaging*, pp. 1043–1046, 2008.

[134] Van Aarle W., Batenburg K. J., and Sijbers J., "Optimal threshold selection for segmentation of dense homogeneous objects in tomographic reconstructions," *IEEE Transactions on Medical Imaging*, vol. 30, no. 4, pp. 980–989, 2011.

[135] Van de Sompel D. and Brady M., "Simultaneous reconstruction and segmentation algorithm for positron emission tomography and transmission tomography," in *Proceedings IEEE International Symposium on Biomedical Imaging*, pp. 1035–1038, 2008.

[136] van Gastel N., Depypere M., Moermans K., Stockmans I., Schrooten J., Maes F., Luyten F., and Carmeliet G., "Interactions between periosteal cells and muscle-derived blood vessels are essential for bone autograft healing," in *Annual meeting of the American Society for Bone and Mineral Research*, 2012.

[137] van Gastel N., Depypere M., Stockmans I., Schrooten J., Maes F., Luyten F., and Carmeliet G., "Interactions between periosteal cells and blood vessels during bone autograft healing: implications for tissue engineering strategies," in *TERMIS World Congress*, 2012.

[138] van Gastel N., Depypere M., Van Looveren R., Schrooten J., Maes F., Luyten F., and Carmeliet G., "Interactions between periosteal cells and blood vessels during bone autograft healing: implications for tissue engineering strategies," in *Cell-VIB Symposium: angiogenesis, metabolic regulation and cancer biology*, 2012.

[139] van Gastel N., Depypere M., Roberts S., Stockmans I., Torrekens S., Schrooten J., Maes F., Luyten F. P., and Carmeliet G., "Revitalization of bone allografts by murine periosteal cells expressing BMP2 and VEGF," in *Annual meeting of the American Society for Bone and Mineral Research*, 2010.

[140] van Gent F., Vande Velde G., van Kuyck K., Rangarajan J., Depypere M., Dresselaers T., Maes F., Nuttin B., and Himmelreich U., "Multi-modality approach to ameliorate stereotactic brain surgery planning in rodents," in *Proceedings SkyScan User Meeting*, 2012.

[141] Van Slambrouck K. and Nuyts J., "Metal artifact reduction in computed tomography using local models in an image block-iterative scheme," *Medical Physics*, vol. 39, no. 11, pp. 7080–7093, 2012.

[142] Vecchi A., Garlanda C., Lampugnani M., Resnati M., Matteucci C., Stoppacciaro A., Schnurch H., Risau W., Ruco L., and Mantovani A., "Monoclonal antibodies specific for endothelial cells of mouse blood vessels. their application in the identification of adult and embryonic endothelium," *European Journal of Cell Biology*, vol. 63, pp. 247–254, 1994.

[143] Verdelis K., Lukashova L., Atti E., Mayer-Kuckuk P., Peterson M., Tetradis S., Boskey A., and van der Meulen M., "MicroCT morphometry analysis of mouse cancellous bone: Intra-and inter-system reproducibility," *Bone*, vol. 49, no. 3, pp. 580–587, 2011.

[144] Vinegar H. J. and Wellington S. L., "Tomographic imaging of three-phase flow experiments," *Review of Scientific Instruments*, vol. 58, no. 1, pp. 96–107, 1987.

[145] von Kossa J., "Ueber die im organismus künstlich erzeugbaren verkalkungen," *Beiträge Zur Pathologischen Anatomie und Zur Allgemeinen Pathologie*, vol. 29, pp. 163–202, 1901.

[146] Waarsing J. H., Day J. S., van der Linden J. C., Ederveen A. G., Spanjers C., De Clerck N., Sasov A., Verhaar J. A. N., and Weinans H., "Detecting and tracking local changes in the tibiae of individual rats: a novel method to analyse longitudinal in vivo micro-CT data," *Bone*, vol. 34, no. 1, pp. 163–169, 2004.

[147] Waarsing J. H., Day J. S., and Weinans H., "An improved segmentation method for in vivo microCT imaging," *Journal of Bone and Mineral Research*, vol. 19, no. 10, pp. 1640–1650, 2004.

[148] Walter D. J., Tkaczyk E. J., and Wu X., "Accuracy and precision of dual energy CT imaging for the quantification of tissue fat content," in *Proceedings of SPIE Medical Imaging: Physics of Medical Imaging*, vol. 6142, pp. 61 421G1–61 421G12, 2006.

[149] Wang J., Li T., and Xing L., "Iterative image reconstruction for CBCT using edge-preserving prior," *Medical Physics*, vol. 36, no. 1, pp. 252–260, 2009.

[150] Webster D., Wirth A., van Lenthe G. H., and Müller R., "Experimental and finite element analysis of the mouse caudal vertebrae loading model: prediction of cortical and trabecular bone adaptation," *Biomechanics and Modeling in Mechanobiology*, vol. 11, no. 1-2, pp. 221–230, 2012.

[151] Whiting B. R., "Signal statistics in X-ray computed tomography," in *Proceedings of SPIE Medical Imaging: Physics of Medical Imaging*, vol. 4682, pp. 53–61, 2002.

[152] Willey J. S., Lloyd S. A., Robbins M. E., Bourland J. D., Smith-Sielicki H., Bowman L. C., Norrdin R. W., and Bateman T. A., "Early increase in osteoclast number in mice after whole-body irradiation with 2 Gy X-rays," *Radiation Research*, vol. 170, no. 3, pp. 388–392, 2008.

[153] Williams H. J. and Davies A. M., "The effect of X-rays on bone: a pictorial review," *European Radiology*, vol. 16, no. 3, pp. 619–633, 2006.

[154] Witt S. T., Riedel C. H., Goessl M., Chmelik M. S., and Ritman E. L., "Point spread function deconvolution in 3D micro-CT angiography for multiscale vascular tree separation," in *Proceedings of SPIE Medical Imaging: Physics of Medical Imaging*, vol. 5030, pp. 720–727, 2003.

[155] Xiang A., Kanematsu M., Kumar S., Yamashita D., Kaise T., Kikkawa H., Asano S., and Kinoshita M., "Changes in micro-CT 3D bone parameters reflect effects of a potent cathepsin K inhibitor (sb-553484) on bone resorption and cortical bone formation in ovariectomized mice," *Bone*, vol. 40, no. 5, pp. 1231–1237, 2007.

[156] Yu H. and Wang G., "Compressed sensing based interior tomography," *Physics in Medicine & Biology*, vol. 54, no. 9, pp. 2791–2805, 2009.

[157] Zeng G. and Gullberg G., "Unmatched projector/backprojector pairs in an iterative reconstruction algorithm," *IEEE Transactions on Medical Imaging*, vol. 19, no. 5, pp. 548–555, 2000.

[158] Zhang G., Cheng J., Zhang L., Chen Z., and Xing Y., "A practical reconstruction method for dual energy computed tomography." *Journal of X-Ray Science & Technology*, vol. 16, no. 2, pp. 67–88, 2008.

List of publications

International Journal

1. K. Laperre*, **M. Depypere***, N. van Gastel, S. Torrekens, K. Moermans, R. Bogaerts, F. Maes and G. Carmeliet, "Development of microCT protocols for in vivo follow-up of mouse bone architecture without major radiation side effects," *Bone*, vol. 49, pp. 613–622, 2011, * equal contribution.

2. Y. Huang, J. Van Dessel, X. Liang, **M. Depypere**, W. Zhong, G. Ma, I. Lambrichts, F. Maes and R. Jacobs, "Effects of immediate and delayed loadings on peri-implant trabecular structures: a cone-beam CT evaluation," *Clinical Implant Dentistry and Related Research*, 2013 (Accepted).

3. J. Van Dessel, Y. Huang, **M. Depypere**, I. Rubira-Bullen, F. Maes and R. Jacobs, "A comparative evaluation of cone-beam computed tomography (CBCT) and micro-CT on trabecular bone structures in the human mandible," *Dentomaxillofacial Radiology*, 2013 (Minor revision).

To be submitted:

M. Depypere, J. Nuyts, K. Van Slambrouck, K. Laperre, N. van Gastel, J. Hermans, G. Carmeliet, F. Maes and P. Suetens, "Simultaneous reconstruction and segmentation of murine bone from low quality microCT images."

M. Depypere, J. Nuyts, K. Van Slambrouck, N. van Gastel, K. Laperre, G. Carmeliet, F. Maes and P. Suetens, "Iterative dual energy microCT reconstruction for a K-edge material by applying adaptive material constraints."

K. Laperre, P. Fraisl, S. Torrekens, R. Van Looveren, G. Bultynck, **M. Depypere**, F. Maes, S. Vinckier, F. Meersman, I. Rombouts, J. Delcour, P. Carmeliet and G. Carmeliet, "The oxygen-sensor PHD2 regulates energy metabolism, protein synthesis and collagen processing in growth plate chondrocytes."

N. van Gastel, **M. Depypere**, P.J. Stiers, I. Stockmans, R. Van Looveren, F. Luyten, F. Maes and G. Carmeliet, "The unique survival properties of periosteal cells preserve the healing of bone grafts in a compromised host microenvironment."

O. Nackaerts, **M. Depypere**, G. Zhang, B. Vandenberghe, F. Maes, SedentexCT and R. Jacobs, "Segmentation of trabecular jaw bone on CBCT datasets."

International Conference: Published in Proceedings

1. **M. Depypere**, J. Nuyts, K. Laperre, G. Carmeliet, F. Maes and P. Suetens, "The minimal entropy prior for simultaneous reconstruction and segmentation of in vivo microCT trabecular bone images," in *Proceedings IEEE International Symposium on Biomedical Imaging*, pp. 586–589, June 2009.

2. **M. Depypere**, J. Nuyts, N. van Gastel, G. Carmeliet, F. Maes and P. Suetens, "An iterative dual energy CT reconstruction method for a K-edge contrast material," in *SPIE Medical Imaging 2011 Conference : Physics of Medical Imaging*, vol. 7961, pp. 79610M1–79610M7, February 2011.

3. **M. Depypere**, J. Nuyts, N. van Gastel, K. Laperre, G. Carmeliet, F. Maes and P. Suetens, "Iterative dual energy reconstruction for noisy microCT images," in *Proceedings SkyScan User Meeting*, pp. 72–75, April 2011.

4. O. Nackaerts, **M. Depypere**, G. Zhang, F. Maes, SedentexCT and R. Jacobs, "Segmentation of trabecular jaw bone on CBCT and microCT datasets," in *Proceedings SkyScan User Meeting*, pp. 254–256, April 2011.

5. F. van Gent, G. Vande Velde, K. van Kuyck, J. Rangarajan, **M. Depypere**, T. Dresselaers, F. Maes, B. Nuttin and U. Himmelreich, "Multi-modality approach to ameliorate stereotactic brain surgery planning in rodents," in *Proceedings SkyScan User Meeting*, April 2012.

International Conference: Abstract or Not Published

1. **M. Depypere**, K. Laperre, G. Carmeliet, F. Maes and P. Suetens, "Expectation-maximisation segmentation of trabecular bone from in vivo microCT," SkyScan User Meeting, June 2008.

2. **M. Depypere**, J. Nuyts, K. Laperre, G. Carmeliet, F. Maes and P. Suetens, "Iterative reconstruction for segmentation of trabecular bone from in vivo microCT," SkyScan User Meeting, April 2009.

3. K. Laperre, **M. Depypere**, N. van Gastel, S. Torrekens, F. Maes and G. Carmeliet, "Effect of in vivo microCT radiation on trabecular bone morphology in mice," Annual meeting of the American Society for Bone and Mineral Research, September 2009.

4. J. Rangarajan, **M. Depypere**, C. Casteels, J. Nuyts, U. Himmelreich, G. Carmeliet, F. Maes and P. Suetens, "Quantitative multi-modal and multi-temporal image analysis in small animal models," Biomedica 2010 - the life science summit, March 2010.

5. **M. Depypere**, N. van Gastel, J. Nuyts, K. Laperre, G. Carmeliet, F. Maes and P. Suetens, "Dual energy microCT imaging of bone and vasculature inside bone," SkyScan User Meeting, July 2010.

6. N. van Gastel, **M. Depypere**, S. Roberts, I. Stockmans, S. Torrekens, J. Schrooten, F. Maes, F. Luyten and G. Carmeliet, "Revitalization of bone allografts by murine periosteal cells expressing BMP2 and VEGF," Annual meeting of the American Society for Bone and Mineral Research, October 2010.

7. K. Laperre, P. Fraisl, **M. Depypere**, S. Vinckier, N. Smets, R. Bouillon, F. Maes, P. Carmeliet and G. Carmeliet, "The oxygen-sensor PHD2 in chondrocytes modifies bone mass by regulating cartilage collagen processing," Annual meeting of the American Society for Bone and Mineral Research, October 2010.

8. J. Rangarajan, G. Vande Velde, K. van Kuyck, **M. Depypere**, F. van Gent, T. Dresselaers, U. Himmelreich and F. Maes, "Assessment of variability within small animal stereotactic neurosurgery and inclusion of vasculature information for planning neuro-anatomical surgery in the rodent brain," ISMRM Annual Meeting & Exhibition, May 2012.

9. Y. Huang, J. Van Dessel, W. Zhong, **M. Depypere**, N. Kou, G. Ma, X. Liang, I. Lambrichts, F. Maes and R. Jacobs, "Radiographic analysis on peri-implant bone subjected to various implant protocols," European Congress of Dentomaxillofacial Radiology, June 2012.

10. O. Nackaerts, **M. Depypere**, G. Zhang, F. Maes and R. Jacobs, "Segmentation of trabecular jaw bone on CBCT datasets," European Congress of Dentomaxillofacial Radiology, June 2012.

11. N. van Gastel, **M. Depypere**, R. Van Looveren, J. Schrooten, F. Maes, F. Luyten and G. Carmeliet, "Interactions between periosteal cells and blood vessels during bone autograft healing: implications for tissue engineering strategies," Cell-VIB Symposium: Angiogenesis, Metabolic Regulation and Cancer Biology, July 2012.

12. N. van Gastel, **M. Depypere**, I. Stockmans, J. Schrooten, F. Maes, F. Luyten and G. Carmeliet, "Interactions between periosteal cells and blood vessels during bone autograft healing: implications for tissue engineering strategies," TERMIS World Congress, September 2012.

13. X. Liang, Y. Huang, J. van Dessel, W. Zhong, **M. Depypere**, J. Gu, B. Vandenberghe, F. Maes, I. Lambrichts, Z. Zhang, G. Ma, R. Jacobs and X. Ma, "CBCT instead of microCT for studying the trabecular bone: a feasible option?," 9th Asian Congress of Oral and Maxillofacial Radiology, September 2012.

14. Y. Huang, J. Van Dessel, X. Liang, **M. Depypere**, G. Ma, W. Zhong, I. Lambrichts, F. Maes and R. Jacobs, "Effects of immediate and delayed implant loadings on trabecular structures: a cone-beam CT evaluation," European Association for Osseointegration, October 2012.

15. N. van Gastel, **M. Depypere**, K. Moermans, I. Stockmans, J. Schrooten, F. Maes, F. Luyten and G. Carmeliet, "Interactions between periosteal cells and muscle-derived blood vessels are essential for bone autograft healing," Annual meeting of the American Society for Bone and Mineral Research, October 2012.

16. J. Van Dessel, Y. Huang, I. Rubira-Bullen, **M. Depypere**, L.F.P. Nicolielo, F. Maes, M.A.H. Duarte and R. Jacobs "A comparative evaluation of cone-beam computed tomography (CBCT) and micro-CT on trabecular bone structures in human mandible," 26th Congresso Odontológico de Bauru, May 2013.

17. J. Van Dessel, Y. Huang, I. Rubira-Bullen, **M. Depypere**, F. Maes and R. Jacobs "A comparative evaluation of cone-beam computed tomography (CBCT) and micro-CT on trabecular bone structures in human mandible," International Congress of Dento-maxillo-facial Radiology, June 2013.

18. A. Van Ende, E. Van de Casteele, **M. Depypere**, F. Maes, B. Van Meerbeek and M. Wevers, "Three dimensional evaluation of polymerization

shrinkage and strain in dental composite restorations using X-ray microtomography," 1st International Conference on Tomography of Materials and Structures, July 2013.

19. A. Van Ende, E. Van de Casteele, **M. Depypere**, M. Wevers, J. De Munck, F. Maes and B. Van Meerbeek, "Non-destructive Analysis of the Displacement and Strain in Composite Restorations," 46th Meeting of the Continental European Division of the International Association for Dental Research, September 2013 (Submitted).

National Conference: Abstract or Not Published

1. **M. Depypere**, K. Laperre, N. van Gastel, S. Torrekens, J. Nuyts, G. Carmeliet, F. Maes and P. Suetens, "Longitudinal in vivo microCT imaging of bone micro-architecture in mice," Knowledge for Growth - sixth edition of FlandersBio's Annual Life Sciences Convention, May 2010 (best poster award).